nature cancer

Article

https://doi.org/10.1038/s43018-026-01257-5

Basophils inhibit early lung metastasis by suppressing regulatory T cells

Received: 4 November 2024

Accepted: 17 September 2026

Published online: 03 November 2026

Check for updates

Bruno Torchia[1,2,17], Nadine Fournier[2,3,17], Simge Yücel[1,2], Morgane Fournier[2,3], Soroush Setareh[4,5], Hadi Esmaily[6,7], Yahya Mohammadzadeh[1,2], Joao Lourenco[2,3], Ali Ghasemi[1,2], Elodie Marcandalli[1,2], Luqing Li[1,2], Mehrnaz Mesdaghi[8,9], Shideh Namazi Bayegi[9], Camilo Faust[10], Anton M. Schule[10], Tommaso Scolaro[11,12], Marta Manco[11,12], Celine Wyser Rmili[1,2], Niki Ubags[13], Stacey D. Finley[14], Christophe von Garnier[13], Massimiliano Mazzone[11,12], Francisco J. Quintana[10,15,16], Michele De Palma[1,2] & Nahal Mansouri[1,2,13] ✉

Basophils are rare cells best known for their role in allergy but their contribution to cancer remains poorly understood. Here, we found that basophils suppress early lung metastatic seeding in mice by enhancing antitumor CD8$^+$ T cell immunity through inhibition of regulatory T (T_{reg}) cells. Basophils restrain T_{reg} cells through two complementary mechanisms: mast cell protease 8-mediated cleavage of interleukin-2 receptor α and histamine-mediated activation of the histamine H1 receptor (HRH1). HRH1 blockade with loratadine abolished T_{reg} cell suppression and accelerated metastatic seeding in mice. In a prospective double-blind crossover trial of loratadine versus placebo enrolling 40 healthy volunteers (IRCT20170608034390N14), circulating T_{reg} cell frequency (primary outcome) increased following loratadine. Higher blood basophil counts predicted improved survival across human cancers and integrative multiomic analyses identified conserved quiescent (B0) and tumor-associated (B1) basophil states, with B0 predicting favorable outcomes. These findings identify basophils as regulators of early metastatic progression and highlight the basophil–T_{reg} cell axis as a potential therapeutic target.

Basophils are rare blood granulocytes best known for their roles in allergic reactions and host defense against parasites and, together with mast cells, are the major cellular source of histamine[1,2]. Despite their established role in allergy, their contribution to tumor progression remains poorly understood.

Previous retrospective studies showed that basophil numbers in peripheral blood are associated with prognosis in persons with cancer. Higher circulating basophil counts have been associated with improved outcomes across multiple cancers[3,4]. Moreover, basophils have been recently shown to exert protective roles in preclinical models of melanoma[5]. Similarly, epidemiological studies suggest that allergic individuals have a reduced risk of several cancers[6–8]. Conversely, recent mechanistic investigations showed that basophil-derived IL-4 prompts protumoral macrophage programming in a mouse lung cancer model[9] and histamine promotes tumor growth by way of histamine H1 receptor (HRH1)-expressing macrophages[10,11]. However, these studies[9–11] focused on the role of basophils and histamine signaling after tumor establishment, leaving the critical early stages of tumor metastasis unexplored.

Regulatory T (T_{reg}) cells have well-established functions in suppressing antitumor immunity, limiting the efficacy of immune

A full list of affiliations appears at the end of the paper. ✉e-mail: nahal.mansouri@chuv.ch

checkpoint blockade, facilitating immune evasion and promoting metastasis[12]. Strategies to either deplete T_{reg} cells or inhibit their function have been shown to enhance antitumor immunity. The tumor-promoting role of T_{reg} cells trades off for a reduced risk of allergy and autoimmune disease[13–15]. T_{reg} cell maintenance and suppressive function depend on IL-2Rα (CD25)–STAT5 signaling and disruption of this pathway impairs T_{reg} cell survival and function[16,17]. Although monocytes, macrophages and dendritic cells regulate T_{reg} cell biology[18], whether basophils do so remains unknown. Here, we identify a basophil–T_{reg} cell axis that limits early metastatic seeding through histamine signaling and disruption of IL-2Rα/CD25 signaling.

Results

Basophils inhibit metastasis to the lung

To identify immune alterations associated with early metastatic seeding, we performed single-cell RNA sequencing (scRNA-seq) of lungs from mice bearing subcutaneous (s.c.) 4T1 mammary tumors 26 days after tumor implantation, when micrometastatic foci (<100 µm) were present (Fig. 1a and Extended Data Fig. 1a). Immune composition was altered in tumor-bearing lungs; neutrophil and monocyte/macrophage populations were significantly expanded, whereas T_{reg} cells were decreased (Fig. 1b,c and Extended Data Fig. 1b,c). Basophils were also increased, although they remained a rare population.

To investigate the role of basophils in lung metastasis, we selectively depleted them using a CD200R3 antibody (anti-CD200R3, Ba103)[19–21]. We injected cancer cells intravenously (i.v.) to obtain two experimental lung metastasis models (Fig. 1d): 4T1 mammary cancer cells modified to express a CD9–mCherry (mCh) fusion protein (4T1-CD9-mCh cells)[22] and *Kras*$^{G12D/+}$;*Tp53*$^{-/-}$ lung cancer cells[23] modified to express green fluorescent protein (GFP) (KP-GFP cells). Anti-CD200R3, initiated 1 or 2 days before cancer cell injection, efficiently and selectively depleted lung basophils (identified as CD45$^+$ CD117$^-$FcεR1$^+$CD49b$^+$; gating strategies used to identify cell populations by flow cytometry in this and subsequent experiments shown in Supplementary Figs. 1–9) as early as 1 day after the first dose and up to the end of the experiment (day 14) (Fig. 1e and Extended Data Fig. 1d,e). Basophil depletion increased cancer cell seeding in the lung in both tumor models (Fig. 1f). After 2 weeks, hematoxylin and eosin (H&E) staining of the lungs of mice that received 4T1-CD9-mCh cells revealed the presence of initial micrometastatic nodules in basophil-depleted mice (Extended Data Fig. 1f). In an independent experiment with longer follow-up (24 days after i.v. injection of unmodified 4T1 cancer cells; Fig. 1g), basophil depletion led to enhanced tumor burden and higher numbers of metastatic nodules, quantified by both microcomputed tomography (micro-CT, day 21) and H&E staining (day 24) (Fig. 1h–k). We obtained similar results in an s.c. 4T1-CD9-mCh mammary tumor model (Extended Data Fig. 1g,h). Notably, whereas early basophil depletion increased cancer cell seeding in the lung, delayed depletion, initiated on day 7 after tumor injection, had no impact on metastatic colonization (Extended Data Fig. 1i,j).

We next examined the kinetics and effects of basophil transfer in tumor-bearing mice. In transgenic *Kras*$^{G12D/+}$;*Tp53*$^{-/-}$ mice[23] (transgenic KP) that received a single basophil dose, donor-derived (CD45.1) basophils persisted in bone marrow, spleen, tumor and adjacent lung for 2 days but were undetectable by day 5 (Extended Data Fig. 1k,l). In another experiment, the adoptive transfer of basophils reduced 4T1-CD9-mCh cancer cell seeding to the lung (Extended Data Fig. 1m,n). Taken together, both cell depletion and transfer studies indicate that basophils inhibit early metastatic seeding of cancer cells to the lung.

Basophils suppress T_{reg} cells in mice

In the i.v. 4T1-CD9-mCh model, anti-CD200R3 moderately increased T_{reg} cells (identified as CD45$^+$CD4$^+$FOXP3$^+$ cells) in the spleen and, to a lesser extent, in the lung on day 14 (Fig. 2a); this response was rapid, as T_{reg} cells increased in the spleen as early as 2 days after basophil elimination. Basophil depletion also moderately increased splenic T_{reg} cells in tumor-free mice (Fig. 2b,c). Conversely, basophil transfer decreased T_{reg} cells (Extended Data Fig. 2a). In an s.c. 4T1-CD9-mCh model, anti-CD200R3 increased T_{reg} cells in tumor, spleen and, to a lesser extent, lung (Extended Data Fig. 2b,c). Together, these findings indicate that basophils restrain T_{reg} cell expansion in both tumor-bearing and tumor-free mice.

Using time-lapse microscopy of whole blood from *Foxp3*-IRES-DTR-eGFP (*Foxp3*^{DTR}) reporter mice, which enable direct visualization of eGFP$^+$ T_{reg} cells without additional staining, we observed frequent basophil–T_{reg} cell clusters (Fig. 2d). Immunostaining of spleen, lung, tumor and tumor draining lymph nodes (dLNs) from mice bearing i.v. 4T1-CD9-mCh tumors likewise revealed frequent basophil–T_{reg} cell clusters. Together, these findings suggest that basophils regulate T_{reg} cells through direct cell contact and/or paracrine signaling.

T_{reg} cells modulate antitumor immunity, partly by inhibiting CD8$^+$ T cells[24]. To explore mechanisms by which basophils regulate T_{reg} cell function, we performed scRNA-seq of lungs of mice that received i.v. 4T1-CD9-mCh cells in combination with basophil depletion. We analyzed the lung cells on both day 1 (early) and day 7 (late) after cancer cell injection (Fig. 2e and Extended Data Fig. 2d). Of note, anti-CD200R3 did not affect lung dendritic cells, which may also express CD200R3 (ref. 25). At both time points, overrepresentation analysis (ORA) of Hallmark pathways revealed an increase in MYC target genes in T_{reg} cells of basophil-depleted mice (Fig. 2f). On day 7, mTORC1, IL-2–STAT5 and PI3K–AKT–mTOR pathways were also enriched. Concurrently, there was an increase in the expression of *Foxp3* and *Stat5a* mRNA in T_{reg} cells (Fig. 2g), as well as in the proportion of T_{reg} cells that expressed the activation genes *Foxp3*, *Stat5a*, *Il2rb*, *Mapk1* and *Tnfrsf18*[26] (Extended Data Fig. 2e). Together, these data indicate that basophils may limit T_{reg} cell activation in mice.

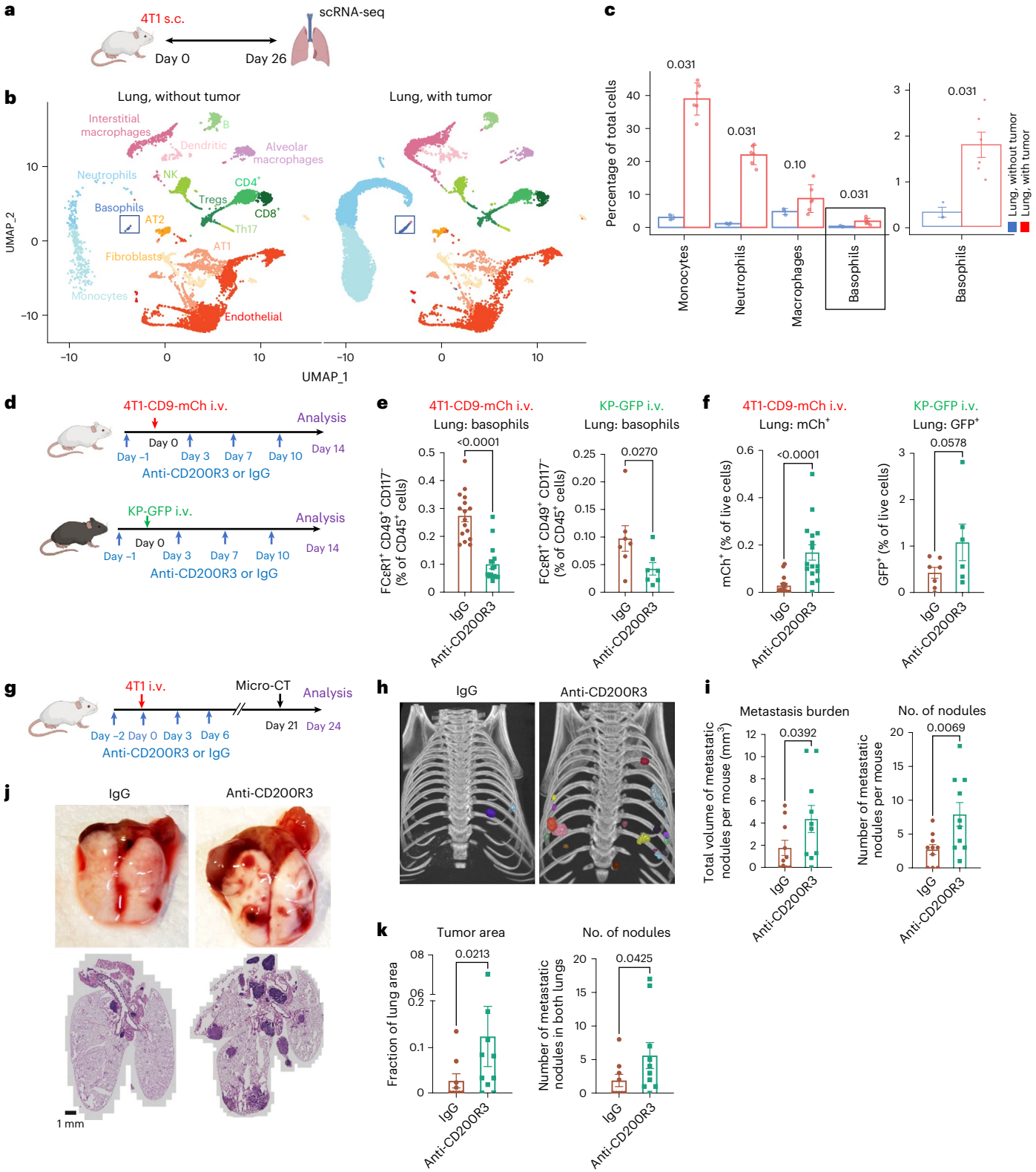
To study basophil-mediated T_{reg} cell functions, we conducted cell cocultures with CD4$^+$CD25^{hi} T_{reg} cell-enriched cells freshly isolated from the mouse spleen (T_{reg} cells hereon) and FCεR1$^+$CD117/Kit$^-$ basophils isolated from the mouse bone marrow. Notably, T_{reg} cells cocultured with basophils exhibited higher apoptosis (Fig. 2h). Because T_{reg} cells naturally suppress CD8$^+$ T cells[24], we next examined the immunosuppressive capacity of basophil-conditioned T_{reg} cells in coculture with CD8$^+$ T cells. While T_{reg} cells efficiently inhibited CD8$^+$ T cell proliferation

Fig. 1 | Basophils inhibit metastasis to the lung. a, Experimental design for scRNA-seq analysis of lungs from s.c. 4T1 tumor-bearing mice. **b**, UMAP showing major lung cell populations in mice without or with tumors. Rectangles indicate basophils. AT1&2, alveolar type 1 and type 2 epithelial cells; NK, natural killer cells. **c**, Proportion of the indicated cell populations among total lung cells in mice without (blue) or with (red) tumors. In **b**,**c**, $n = 3$ mice without tumors and $n = 6$ mice with tumors. **d**, Experimental design for basophil depletion with anti-CD200R3 antibody or irrelevant IgG in two lung metastasis models using 4T1-CD9-mCh (top) or KP-GFP (bottom) cells. **e**, Percentage of lung basophils (CD45$^+$CD117$^-$FcεRI$^+$CD49b$^+$) following i.v. injection of 4T1-CD9-mCh (left; $n = 16$) or KP-GFP (right; $n = 7$) cells. **f**, Percentage of lung tumor cells following basophil depletion. Left, 4T1-CD9-mCh cells (CD45$^-$mCh$^+$ live cells; $n = 16$). Right, KP-GFP cells (CD45$^-$GFP$^+$ live cells; $n = 7$ IgG and $n = 6$ anti-CD200R3). **g**, Experimental design for basophil depletion in mice injected with 4T1 cells. **h**, Representative micro-CT images of lung metastatic nodules. **i**, Quantification of metastatic burden and number of metastatic nodules ($n = 10$). **j**, Representative lungs showing macroscopic appearance (top) and H&E staining (bottom). **k**, Quantification of tumor area and metastatic nodules from H&E-stained lung sections ($n = 9$ IgG and $n = 10$ anti-CD200R3). Data are presented as the mean ± s.e.m. in bar plots. Statistical analysis was conducted using a Wilcoxon test with Benjamini–Hochberg correction (**c**), unpaired two-sided (4T1-CD9-mCh) or one-sided (KP-GFP) Student's *t*-test (**e**,**f**), unpaired one-sided Student's *t*-test (**i**) or unpaired one-sided Mann–Whitney test (**k**).

https://doi.org/10.1038/s43018-026-01257-5

in the absence of basophils, the presence of basophils negated this effect (Extended Data Fig. 2f). To eliminate potential direct effects of basophils on CD8$^+$ T cells, we cultured T_{reg} cells with or without basophils for 4 h and then sorted the T_{reg} cells before adding CD8$^+$ T cells. Basophil-exposed T_{reg} cells had lower suppressive capacity than basophil-naive T_{reg} cells after 72 h of coculture (Fig. 2i), a response that was abrogated by pretreating T_{reg} cells with Z-VAD-FMK, an irreversible pan-caspase inhibitor[27] (Fig. 2j).

Basophil-treated T_{reg} cells also restored OVA-specific CD8$^+$ T cell killing of MC38-OVA cells (Fig. 2k). Basophils had no direct effect on tumor cells, as neither coculture with KP-GFP cells nor prolonged exposure of 4T1-CD9-mCh cells to basophil-conditioned medium (baso-med) altered tumor cell viability or lung-seeding capacity (Extended Data Fig. 2g–i). scRNA-seq of basophil–T_{reg} cell–CD8 cocultures showed enrichment of mTORC1, IFNγ response and effector T cell programs in CD8$^+$ T cells (Extended Data Fig. 2j). Moreover, we



observed upregulation of the 'effector T cell' gene set[28] in $CD8^+$ T cells cocultured with basophils and T_{reg} cells, as compared to $CD8^+$ T cells cocultured with T_{reg} cells alone (Extended Data Fig. 2k). Consistent with these findings, $CD8^+$ T cells from basophil-depleted lungs (Fig. 2e) showed enrichment of an exhausted versus memory T cell signature (Fig. 2l). $CD8^+$ T cell numbers also decreased in lungs of tumor-free mice and mice with s.c. 4T1-CD9-mCh tumors, as well as in the blood of mice that received i.v. 4T1-CD9-mCh cells (Fig. 2m). Together, these results indicate that basophils suppress T_{reg} cells to enhance $CD8^+$ T cell proliferation and cytotoxicity.

Basophil-secreted histamine inhibits T_{reg} cells

To elucidate the mechanism underlying basophil-induced T_{reg} cell inhibition, we analyzed the top deregulated genes in lung basophils from mice with s.c. 4T1 tumors (Extended Data Fig. 3a and Fig. 1a). *Hdc*, encoding the histamine-synthesizing enzyme, was among the most upregulated genes. Therefore, we investigated whether basophil-derived histamine[29] contributes to T_{reg} cell inhibition.

We examined histamine receptor mRNA expression in human T_{reg} cells using the Human Protein Atlas (HPA). Of the four histamine receptors (HRH1–HRH4), *HRH1* was the predominant receptor expressed by T_{reg} cells (Fig. 3a and Extended Data Fig. 3b). *HRH1* mRNA was also enriched in T_{reg} cells compared to other immune cell populations. We confirmed *HRH1* expression in both mouse and human T_{reg} cells by qPCR (Fig. 3b) and detected HRH1 protein in human T_{reg} cells using a capillary-based immunoassay (Fig. 3c).

We then asked whether basophils modulate HRH1 signaling in T_{reg} cells. We cocultured basophils with T_{reg} cells, in either the presence or the absence of loratadine, a type 1 antihistamine that specifically blocks HRH1 (ref. 30). scRNA-seq analysis revealed several deregulated genes in T_{reg} cells, a response that was partially reversed by loratadine (Fig. 3d and Extended Data Fig. 3c). To assess T_{reg} cell phenotype, we used a T_{reg} cell-associated signature comparing T_{reg} cells to effector $CD4^+$ cells[31]. Basophil exposure downregulated this signature, whereas loratadine reversed the effect (Fig. 3e and Extended Data Fig. 3d). Of the leading-edge genes identified in both analyses, 31 were shared. Consistent with this, basophil-exposed T_{reg} cells expressed lower FOXP3 protein, which was restored by loratadine in a dose-dependent manner (Fig. 3f). Basophils also induced a histamine-response signature[32], again reversed by loratadine (Extended Data Fig. 3e). We next applied the network-based drug-repurposing tool SAveRUNNER, which identified type 1 antihistamines (HRH1 blockers) as the most significantly enriched drug class among genes downregulated by basophils (Extended Data Fig. 3f,g). Lastly, integration of our scRNA-seq data with an independent T_{reg} cell dataset[33] showed that basophils shifted T_{reg} cells toward an effector/nonlymphoid tissue phenotype, whereas loratadine restored the central/lymphoid tissue state (Extended Data Fig. 3h).

We next investigated downstream consequences of HRH1 activation. Pathway enrichment analysis of scRNA-seq data from basophil-exposed T_{reg} cells revealed increased calcium signaling, which was attenuated by loratadine (Extended Data Fig. 3i). Mitochondrial superoxide production was also increased in basophil-exposed T_{reg} cells and reduced by either loratadine or the nitric oxide donor DETA NONOate (Fig. 3g). Basophil-exposed T_{reg} cells also exhibited increased apoptosis signatures[34] (Spearman's $\rho = 0.64$; Extended Data Fig. 3j) and activation of the proapoptotic caspase pathway, both of which were attenuated by loratadine (Extended Data Fig. 3k).

To investigate the involvement of HRH1 signaling in T_{reg} cell apoptosis, we cultured T_{reg} cells with baso-med and assessed caspase activation using a polycaspase assay (Extended Data Fig. 3l). Baso-med increased early apoptosis at 24 h and late apoptosis at 36 h. Loratadine did not affect basal T_{reg} cell apoptosis but attenuated baso-med-induced apoptosis at both time points. Consistent with these findings, histamine also modestly increased T_{reg} cell apoptosis, an effect reversed by loratadine (Extended Data Fig. 3m).

To further understand basophil-mediated HRH1 signaling and downstream mechanisms involved in T_{reg} cell inhibition, we intersected transcriptomic analysis of T_{reg} cells from three independent experiments: scRNA-seq analysis of basophil-exposed T_{reg} cells treated with loratadine ex vivo, bulk RNA-seq analysis of splenic T_{reg} cells isolated from loratadine-treated mice and scRNA-seq analysis of lung of basophil-depleted mice (Fig. 3h). Pathway ORA of common upregulated genes in T_{reg} cells after basophil and/or histamine signaling inactivation revealed significant enrichment in IL-2R–STAT5 and PI3K–AKT–mTOR signaling, both of which are associated with enhanced T_{reg} cell stability, function and survival[17,35]. Taken together, these results indicate that basophils inhibit T_{reg} cells through HRH1 signaling.

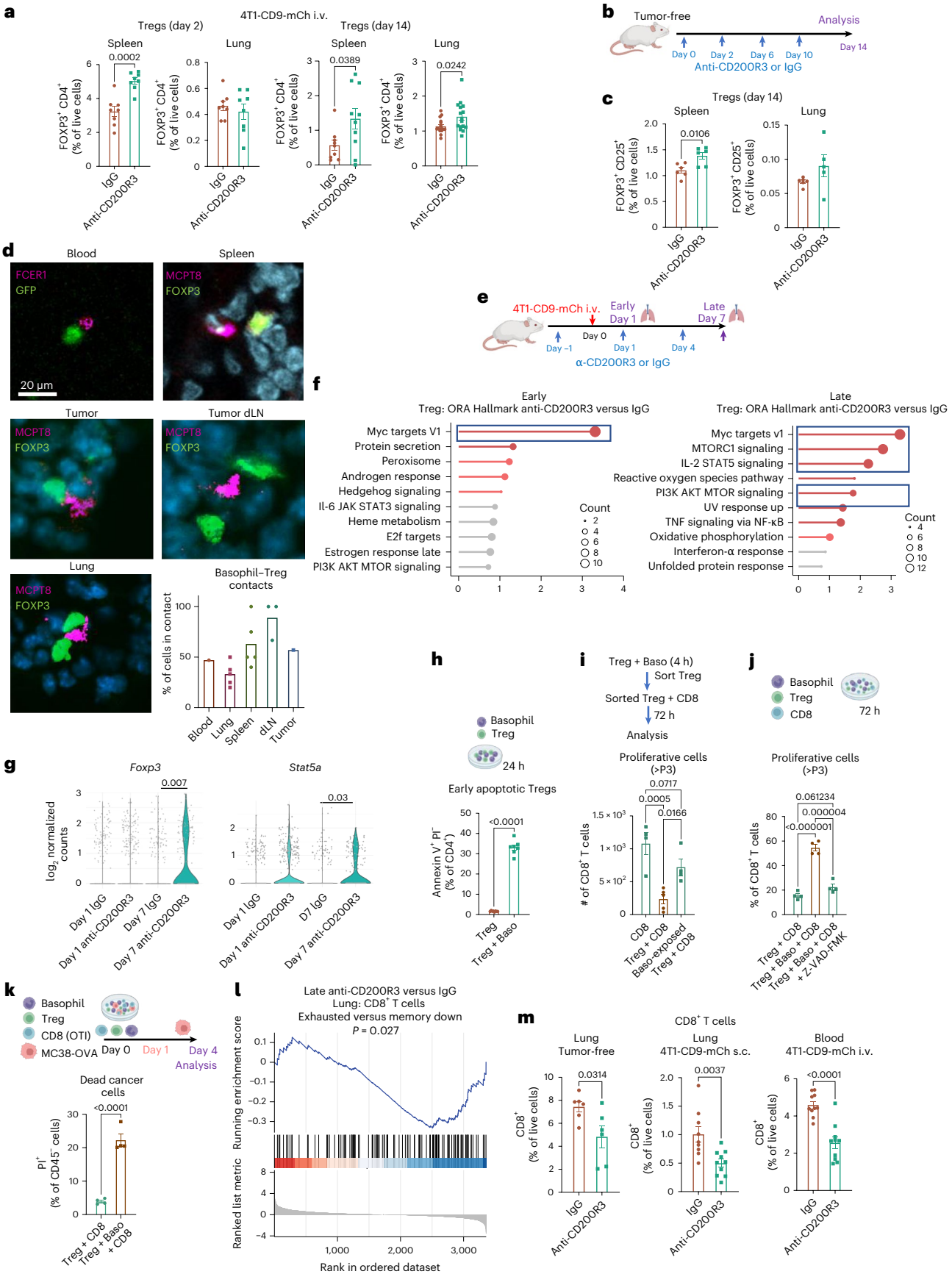
Loratadine did not alter basophil activation, including histamine secretion, activation marker expression or expression of *Hdc* and *Mcpt8* (Extended Data Fig. 3n–p). As activated T_{reg} cells have been reported to stimulate basophils through IL-3 (ref. 36), we examined the reciprocal interaction but observed no changes in activation marker expression (*Cd200r3*, *Cd63* and *Fcer1*) or histamine release (Extended Data Fig. 3q,r). Consistent with this, kinetic analysis showed comparable histamine release from basophils cultured alone or with T_{reg} cells (Extended Data Fig. 3r). Together, these findings indicate that basophil-derived histamine acts primarily on T_{reg} cells.

Inhibition of histamine signaling impairs $CD8^+$ T cells and enhances lung metastatic seeding in mice

To study the effects of HRH1-mediated T_{reg} cell inhibition on $CD8^+$ T cell phenotypes and functions, we analyzed scRNA-seq data of $CD8^+$ T cells cocultured with basophils and T_{reg} cells, with or without loratadine (Fig. 3d). Loratadine downregulated multiple basophil-induced genes and pathways associated with effector and tumoricidal activity in $CD8^+$

Fig. 2 | Basophils suppress T_{reg} cells in mice. a, Percentage of splenic and lung T_{reg} cells after i.v. injection of 4T1-CD9-mCh cells at the indicated time points. Experimental design was as in Fig. 1d. Day 2, $n = 8$; day 14, $n = 9$ IgG and $n = 10$ (anti-CD200R3) for spleen, $n = 16$ for lung. **b**, Experimental design in tumor-free mice. **c**, Percentage of splenic (left) and lung (right) T_{reg} cells ($n = 6$ for spleen, $n = 6$ IgG and $n = 5$ anti-CD200R3 for lung). **d**, Representative immunofluorescence images and quantification of $Fc\varepsilon RI^+$ basophils and $eGFP^+$ T_{reg} cells in blood and $MCPT8^+$ basophils and $FOXP3^+$ T_{reg} cells in spleen, lung, tumor and dLN ($n = 1$ for blood and tumor, $n = 5$ for lung and spleen, $n = 3$ for dLN). **e**, Experimental design for lung scRNA-seq of basophil-depleted mice injected with 4T1-CD9-mCh cells. **f**, Hallmark ORA of the 200 most upregulated genes in T_{reg} cells on day 1 (left) and day 7 (right) ($n = 3$ mice per group). Circle size indicates gene number; *x* axis, $-\log_{10}$(*P* value): red, $P < 0.05$; light red, $P < 0.1$. **g**, Violin plots of *Foxp3* and *Stat5a* expression in T_{reg} cells ($n = 358$ day 1 IgG, $n = 471$ day 1 anti-CD200R3, $n = 264$ day 7 IgG and $n = 207$ day 7 anti-CD200R3 T_{reg} cells from three mice per group). **h**, Experimental design (top) and percentage of annexin V^+PI^- apoptotic T_{reg} cells (bottom) ($n = 8$ T_{reg} cells and $n = 7$ T_{reg} cells + basophils). **i**, Experimental design (top) and absolute number of CTV-labeled $CD8^+$ T cells undergoing >3 divisions after 72 h of coculture with T_{reg} cells (bottom) ($n = 4$ CD8 and basophil-exposed T_{reg} cells + CD8, $n = 5$ T_{reg} cells + CD8). **j**, Experimental design (top) and percentage of CTV-labeled $CD8^+$ T cells undergoing >3 divisions ($n = 4$). **k**, Experimental design (top) and percentage of PI^+ cancer cells in the OT-I killing assay (bottom) ($n = 4$). **l**, GSEA of an exhausted versus memory $CD8^+$ T cell signature (GSE9650)[28] ($n = 3$). **m**, Percentage of $CD8^+$ T cells following basophil depletion. Left, tumor-free mice, day 14 ($n = 6$); middle, s.c. 4T1-CD9-mCh, day 10 ($n = 9$ IgG and $n = 10$ anti-CD200R3); right, i.v. 4T1-CD9-mCh, day 7 ($n = 10$). Data are presented as the mean ± s.e.m. in bar plots. Statistical analysis was conducted using an unpaired two-sided Student's *t*-test (**a**,**c**,**g**,**h**,**k**,**m**), one-sided Fisher's exact test (**f**), one-way ANOVA followed by Fisher's LSD test (**i**,**j**) or GSEA with significance determined by 100,000 random permutations (l). For **h**–**k**, *n* represents the number of independent cell cultures. Panels **h**, **j** and **k** created in BioRender; De Palma Lab EPFL https://biorender.com/8yxozuz (2026).

https://doi.org/10.1038/s43018-026-01257-5



https://doi.org/10.1038/s43018-026-01257-5

T cells, such as granzyme A (*Gzma*) and *Gzmb* (Extended Data Fig. 4a). Furthermore, loratadine restored the immunosuppressive capacity of basophil-exposed T_{reg} cells, as shown by reduced $CD8^+$ T cell proliferation, without directly affecting $CD8^+$ T cell proliferation in the absence of T_{reg} cells (Fig. 4a and Extended Data Fig. 4b). Moreover, the addition of loratadine to a coculture of MC38-OVA cancer cells with basophils and T_{reg} cells decreased antigen-specific cancer cell killing by OT-I $CD8^+$ T cells (Fig. 4b). These findings indicate that basophils suppress T_{reg} cells, at least in part, through HRH1 signaling, leading to $CD8^+$ T cell activation, proliferation and tumoricidal activity, whereas loratadine abrogates this effect.

We then examined the effect of loratadine on T_{reg} cell-mediated $CD8^+$ T cell suppression in mice. In both tumor-free mice and mice that received i.v. injections of either 4T1-CD9-mCh or KP-GFP cancer

Fig. 3 | Basophil-secreted histamine inhibits T_{reg} cells. a, *HRH1* expression across immune cell populations from the HPA. Expression is shown as normalized TPM. **b**, qPCR analysis of *Hrh1* (mouse; left) and *HRH1* (human; right) expression in the indicated immune cells, normalized to housekeeping genes (mouse: *Gapdh* and *Hprt*; human: *GAPDH*) ($n = 3$ T_{reg} cells and basophils and $n = 4$ $CD8^+$ T cells for mouse, $n = 3$ HEK-293 and $n = 4$ other groups for human). **c**, Left, automated western blot analysis of HRH1 in the indicated human cells with β-actin as a loading control. Right, quantification ($n = 3$ T_{reg} cells and $n = 2$ $CD8^+$ T cells and HEK-293). **d**, Top, experimental design for scRNA-seq of basophil–T_{reg} cell cocultures. Bottom, heat map of differentially expressed T_{reg} cell genes following basophil coculture ($|\log_2$ fold change$| > 1.5$, $P < 0.05$). Genes induced or repressed by basophils and reversed by loratadine are shown above and below, respectively. Venn diagrams show overlapping genes ($n = 2$). **e**, GSEA of T_{reg} cell versus effector $CD4^+$ T cell signature (GSE14350)[31] in indicated comparison ($n = 2$). **f**, Percentage of $FOXP3^+$ cells in the indicated cocultures ($n = 8$). **g**, MitoSOX mean fluorescence intensity in T_{reg} cells after 18 h of coculture (left) and representative fluorescence images (right) ($n = 4$). MitoSOX, green; nuclei, blue. **h**, Integrated analysis of three T_{reg} cell transcriptomic datasets. Left, basophil–T_{reg} cell cocultures ± loratadine ($n = 2$ independent cell cultures), splenic T_{reg} cells from loratadine-treated tumor-free mice ($n = 4$ vehicle and $n = 2$ loratadine) and lung T_{reg} cells from basophil-depleted tumor-bearing mice ($n = 3$). Middle, Venn diagram of 296 shared upregulated genes ($\log_2$ fold change > 0) (middle). Right, Hallmark ORA of shared genes. Red, $P < 0.05$; orange, $P < 0.1$. Data are presented as the mean ± s.e.m. in bar plots. Statistical analysis was conducted using a differential expression analysis with adjusted $P < 0.05$ and $|\log_2$ fold change$| > 1.5$ (**d**), GSEA with 100,000 permutations (**e**), one-way ANOVA with Fisher's LSD test (**f**,**g**), Fisher's exact test ($P = 3 \times 10^{-11}$) and one-sided Fisher's exact test for ORA (**h**). For **b**,**c**,**f**,**g**, *n* represents the number of independent cell cultures (mouse) or independent donors (human). Panels **d** and **h** created in BioRender; De Palma Lab EPFL https://biorender.com/8yxozuz (2026).

cells, daily doses of loratadine moderately increased T_{reg} cells in the peripheral blood and spleen (Fig. 4c,d and Extended Data Fig. 4c,d). A similar trend was observed with diphenhydramine, another HRH1 antagonist. In the KP-GFP model, loratadine enhanced cancer cell dissemination in the lung, as shown by immunostaining (Fig. 4e) and flow cytometry (Fig. 4f) analyses. This effect was associated with a decrease in $GZMB^+CD8^+$ T cells in both blood and lungs of loratadine-treated mice (Fig. 4g and Extended Data Fig. 4e). These findings suggest that HRH1 blockade increases cancer cell homing to the lung by promoting immune-suppressive effects.

To study T_{reg} cells and $CD8^+$ T cells following HRH1 blockade, we analyzed bulk RNA-seq of T_{reg} cells and $CD8^+$ T cells isolated from the spleens of loratadine-treated or vehicle-treated mice. T_{reg} cells from loratadine-treated mice upregulated IL-2–STAT5 signaling and downregulated protein kinase C activation, a downstream effector of histamine signaling (Fig. 4h,i and Extended Data Fig. 4f). $CD8^+$ T cells exhibited reduced expression of proliferation (*Mki67*) and cytotoxic (*Gzma* and *Gzmb*) genes among the top 20 differentially expressed genes (Fig. 4j and Extended Data Fig. 4g). Gene set enrichment analysis (GSEA) confirmed downregulation of cell cycle, cell proliferation (G2M, mTOR and E2F) and IFNγ/IFNα response pathways. Together, these findings indicate that HRH1 blockade suppresses $CD8^+$ T cell activation and promotes metastatic seeding in the lung.

Loratadine improves recovery from experimental autoimmune encephalitis (EAE)

We then asked whether loratadine could be beneficial in a mouse model of autoimmunity in which T_{reg} cells are dysfunctional. To this end, we used the EAE model of multiple sclerosis[15]. Loratadine-treated mice exhibited moderately lower EAE scores and accelerated recovery compared to vehicle-treated mice (Fig. 4k,l). These findings suggest that loratadine could be beneficial in autoimmune diseases.

Basophils inhibit T_{reg} cells through mast cell protease 8 (MCPT8)-mediated IL-2Rα (CD25) cleavage

Because basophils and T_{reg} cells associated in vivo (Fig. 2d), we asked whether T_{reg} cell suppression requires direct cell contact. Transwell separation moderately reduced T_{reg} cell killing (Extended Data Fig. 5a), indicating that both diffusible histamine and contact-dependent mechanisms contribute to T_{reg} cell inhibition.

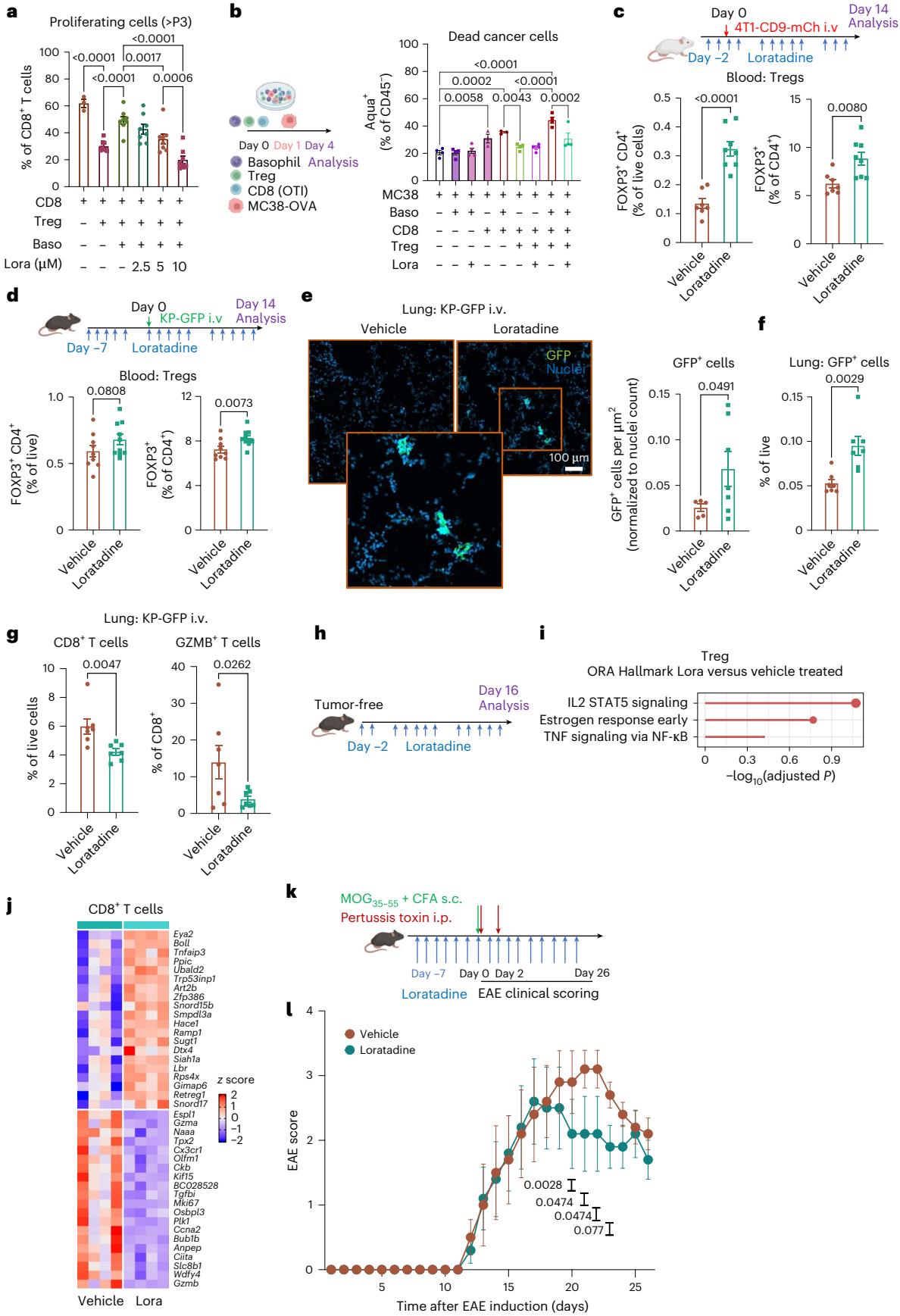
Flow cytometry showed near-complete loss of IL-2Rα/CD25 on T_{reg} cells within 4 h of coculture with basophils, confirmed using two antibodies against the extracellular domain of CD25 (Fig. 5a and Extended Data Fig. 5b). This is consistent with the increased IL-2–STAT5 signaling observed in T_{reg} cells from basophil-depleted mice (Fig. 2f). Transwell separation completely prevented CD25 loss, indicating a contact-dependent mechanism (Extended Data Fig. 5c). In contrast, mast cells did not reduce CD25 expression (Extended Data Fig. 5d). CD25 loss was largely independent of HRH1 signaling, as loratadine had only a modest effect (Extended Data Fig. 5e) and remained sustained after basophil removal (Extended Data Fig. 5f).

To further elucidate the mechanism underlying basophil-mediated CD25 loss, we cultured T_{reg} cells alone or with basophils and analyzed *Il2ra* RNA and CD25 protein after 24 h. *Il2ra* mRNA and total CD25 protein abundance were unchanged (Extended Data Fig. 5g,h). However, western blot analysis revealed an approximately 10-kDa reduction in CD25 molecular weight following basophil exposure (Fig. 5b), suggesting extracellular proteolytic cleavage and reconciling the flow cytometry and western blot findings.

Basophils express several proteases[2]. To identify the enzyme responsible, we cocultured T_{reg} cells and basophils in the presence of protease inhibitors. The serine protease inhibitor AEBSF completely rescued CD25 expression and molecular weight, as assessed by flow cytometry (Fig. 5c) and western blot (Fig. 5d). Bulk RNA-seq of ex vivo cultured basophils identified *Mcpt8* and *Prss34* among the top 20

Fig. 4 | Inhibition of histamine signaling impairs $CD8^+$ T cells and enhances lung metastatic seeding in mice. a, Percentage of CTV-labeled $CD8^+$ T cells undergoing >3 rounds of proliferation after 72 h of coculture with the indicated cells and loratadine concentrations ($n = 3$ $CD8^+$ T cells alone and $n = 8$ other conditions). **b**, Left, experimental design for the OT-I killing assay. Right, percentage of dead cancer cells ($CD45^-$ $Aqua^+$) ($n = 3$ MC38 + CD8 and MC38 + basophils + CD8, $n = 4$ other groups). **c**, Top, experimental design for loratadine treatment before i.v. injection of 4T1-CD9-mCh cells. Bottom, percentage of $FOXP3^+$ T_{reg} cells among live and $CD4^+$ T cells in blood ($n = 7$ vehicle and $n = 8$ loratadine). **d**, Top, experimental design for loratadine treatment before i.v. injection of KP-GFP cells. Bottom, percentage of $FOXP3^+$ T_{reg} cells among live and $CD4^+$ T cells in blood ($n = 9$ vehicle and $n = 10$ loratadine). **e**, Left, representative lung immunofluorescence images from experiment in **d**. GFP^+ tumor cells, green; nuclei, blue (DAPI). Inset shows magnified view of the boxed region in the loratadine-treated lung. Right, quantification of GFP^+ area normalized to DAPI ($n = 5$ vehicle and $n = 7$ loratadine). **f**, Percentage of lung GFP^+ cancer cells (live $CD45^-$ GFP^+) measured by flow cytometry ($n = 7$). **g**, Percentage of $CD8^+$ T cells among live lung cells and $GZMB^+$ cells within $CD8^+$ T cells following i.v. injection of KP-GFP cells ($n = 7$). **h**, Experimental design for loratadine treatment in tumor-free mice. Splenic T_{reg} cells and $CD8^+$ T cells were sorted on day 16 for bulk RNA-seq. **i**, Hallmark ORA of the 200 most upregulated genes in splenic T_{reg} cells. Circle size indicates gene number; *x* axis, $-\log_{10}$(adjusted *P*). The 200 upregulated genes were derived from comparison of vehicle-treated ($n = 4$) and loratadine-treated ($n = 2$) mice. **j**, Heat map of the 20 most differentially expressed genes in splenic $CD8^+$ T cells ($n = 4$). **k**, Experimental design for EAE. **l**, EAE clinical scores in vehicle-treated and loratadine-treated mice ($n = 5$). Data are presented as the mean ± s.e.m. in bar plots. Statistical analysis was conducted using a one-way ANOVA followed by Fisher's LSD test (**a**,**b**), unpaired two-sided Student's *t*-test (**c**), unpaired one-sided Student's *t*-test (**d**–**g**), one-sided Fisher's exact test (**i**) or multiple paired two-sided Student's *t*-tests (**l**). For **a**,**b**, *n* represents the number of independent cell cultures. Panel **b** created in BioRender; De Palma Lab EPFL https://biorender.com/8yxozuz (2026).

https://doi.org/10.1038/s43018-026-01257-5



https://doi.org/10.1038/s43018-026-01257-5

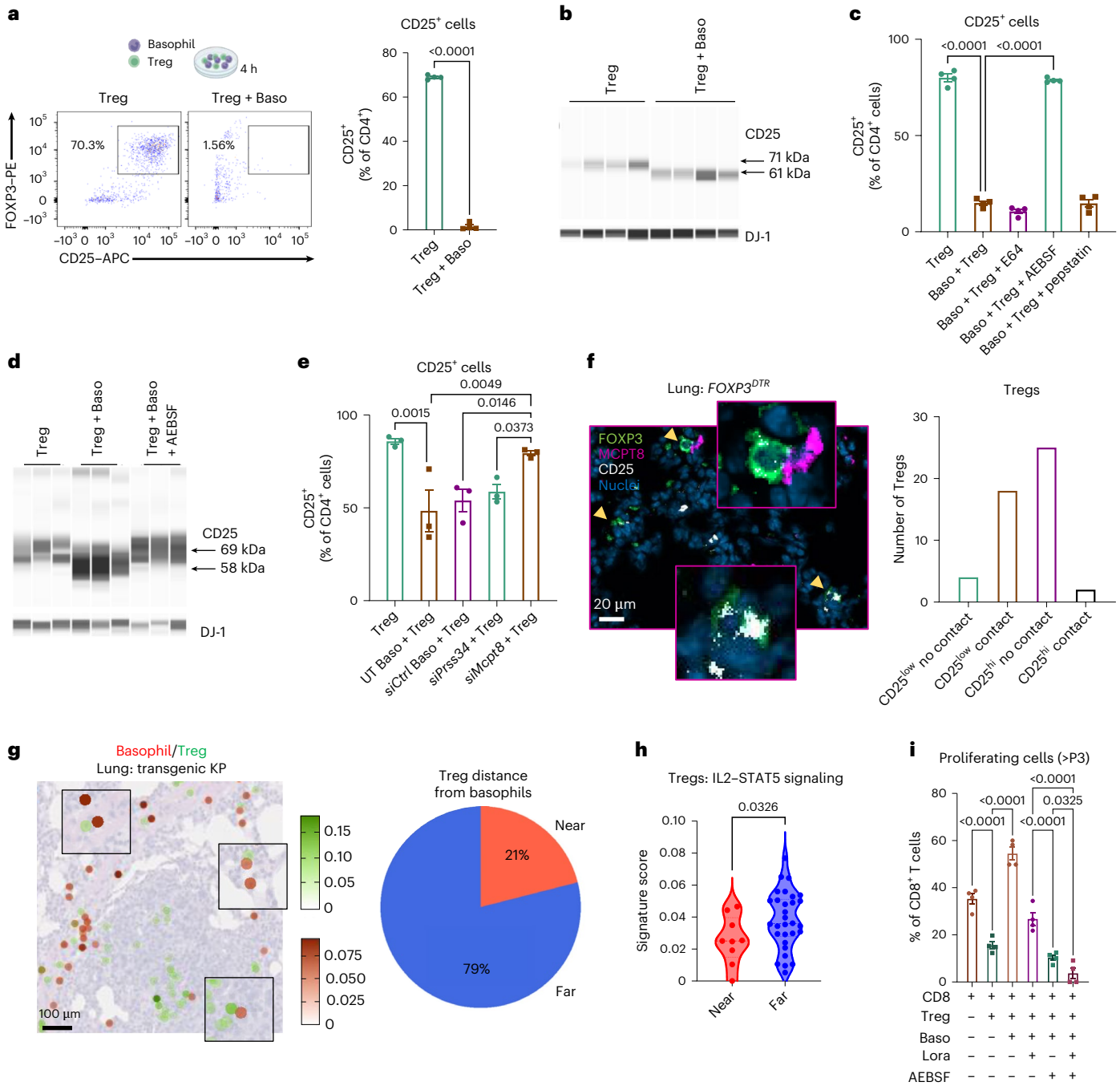


Fig. 5 | Basophils inhibit T_{reg} cells through MCPT8-mediated IL-2Rα (CD25) cleavage. a, Top, experimental design for the 4-h coculture assay. Bottom, representative data showing CD25 (IL-2Rα) expression in T_{reg} cells after coculture with basophils, using clone PC61 ($n = 4$). **b**, Automated western blot analysis of CD25 (IL-2Rα) in T_{reg} cells sorted after 24 h of coculture. Bands at 71 kDa (T_{reg} cells) and 61 kDa (basophil-exposed T_{reg} cells) are shown. DJ-1 served as the loading control ($n = 4$). **c**, Percentage of $CD25^+$ cells among $CD4^+$ cells following 24 h T_{reg} cell–basophil coculture with the indicated protease inhibitors: pepstatin A (aspartyl protease inhibitor), AEBSF (serine protease inhibitor) and E64 (cysteine protease inhibitor) ($n = 4$). **d**, Automated western blot analysis of CD25 (IL-2Rα) in T_{reg} cells sorted from the indicated cocultures after 24 h. Bands at 69 kDa (T_{reg} cell and T_{reg} cell + basophils + AEBSF) and 58 kDa (T_{reg} cell + basophils) are shown. DJ-1 served as the loading control ($n = 3$). **e**, Percentage of $CD25^+$ cells among $CD4^+$ cells following 4 h of coculture with basophils transfected with the indicated siRNAs ($n = 3$). UT, untransfected. **f**, Left, representative immunofluorescence images of lungs from *FOXP3*^{DTR} mice stained for MCPT8 (magenta), GFP (green), CD25 (white) and DAPI (blue). Insets show magnified views of selected regions indicated by yellow arrowheads. Right, quantification of $CD25^{hi}$ and $CD25^{low}$ T_{reg} cells, alone or in contact with basophils. Cells were analyzed across >10 fields of view from one mouse lung. **g**, Left, representative spatial transcriptomic map of KP mouse showing basophil and T_{reg} cell signature scores. Black boxes indicate representative regions of basophil–T_{reg} cell spatial proximity. Right, pie chart showing the proportion of T_{reg} cells located ≤50 µm (near) or >50 µm (far) from basophils. **h**, Violin plot of Hallmark IL-2–STAT5 signaling pathway signature scores in T_{reg} cells ($n = 9$ near and $n = 30$ far cells). In **g**,**h**, cells were analyzed across >10 fields of view from one KP mouse lung. **i**, Percentage of proliferating $CD8^+$ T cells undergoing >3 rounds of proliferation after 72 h of coculture with loratadine, AEBSF or both. The T_{reg} cell + CD8 and T_{reg} cell + basophils + CD8 control data are also shown in Fig. 2j ($n = 4$). Data are presented as the mean ± s.e.m. in bar plots. Statistical analysis was conducted using an unpaired two-sided Student's *t*-test (**a**,**h**) or one-way ANOVA followed by Fisher's LSD test (**c**,**e**,**i**). For **a**–**e**,**i**, *n* represents the number of independent cell cultures. Panel **a** created in BioRender; De Palma Lab EPFL https://biorender.com/8yxozuz (2026).

https://doi.org/10.1038/s43018-026-01257-5

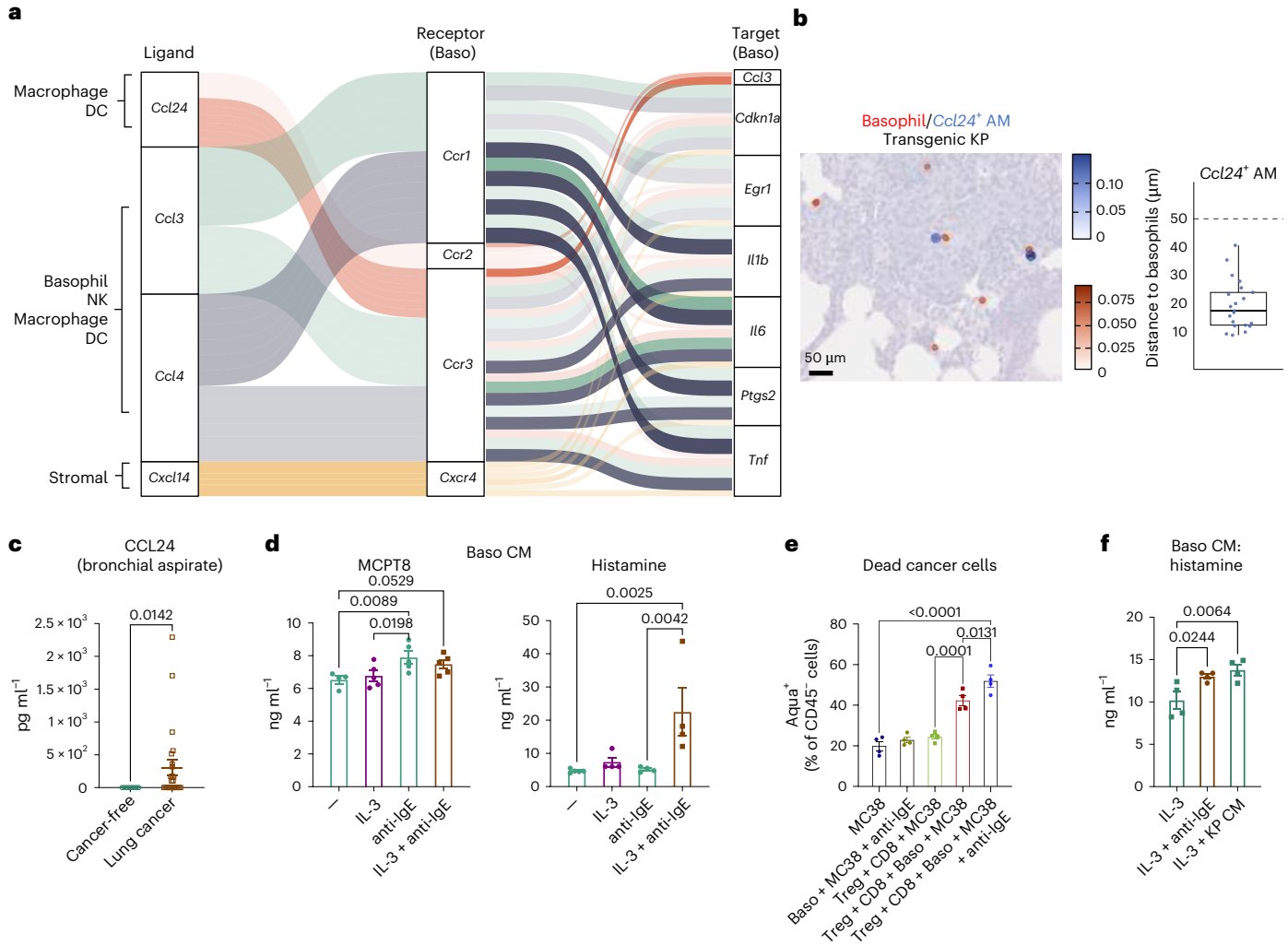


Fig. 6 | CCL24 and IgE–FcεRI engagement drive basophil recruitment and activation in cancer. a, Sankey plot of predicted ligand–receptor interactions involved in basophil recruitment identified by NicheNet analysis. Ligands expressed by nonbasophil populations (left) are connected to their predicted basophil receptors (middle) and downstream target genes (right). Connection width reflects predicted interaction strength. Analysis was derived from the data shown in Fig. 1a ($n = 3$ tumor-free and $n = 6$ tumor-bearing mice). **b**, Left, representative spatial transcriptomic image showing *Ccl24*$^+$ AMs (blue) and basophils (red) within and around the tumor. Right, quantification of the distance between each *Ccl24*$^+$ AM and its nearest basophil. Each point represents one *Ccl24*$^+$ AM ($n = 21$ cells). Cells were analyzed across >10 fields of view from one KP mouse lung. **c**, CCL24 concentrations in bronchial aspirates from individuals with or without lung cancer measured by ELISA ($n = 8$ cancer-free participants and $n = 24$ participants with lung cancer). **d**, MCPT8 and histamine concentrations in culture supernatants of basophils treated with medium, IL-3 or anti-IgE for 24 h, measured by ELISA ($n = 4$ untreated and $n = 5$ other conditions for MCPT8, $n = 5$ untreated and $n = 4$ other conditions for histamine). **e**, OT-I killing assay of MC38-OVA cells cultured under the indicated conditions and analyzed after 4 days. Anti-IgE was added 24 h before analysis. The graph shows the percentage of dead tumor cells (Aqua$^+$ among CD45$^-$ cells) ($n = 4$). **f**, Histamine concentrations in culture supernatants of IL-3-primed basophils stimulated with anti-IgE or KP-conditioned medium for 16 h, measured by ELISA ($n = 4$). Data are presented as the mean ± s.e.m. in bar plots. In **b**, the box plot shows the median, interquartile range (IQR) and whiskers extending to the most extreme values within 1.5× the IQR. Statistical analysis was conducted using an unpaired two-sided Mann–Whitney test (**c**) or one-way ANOVA followed by Fisher's LSD test (**d**–**f**). For **d**–**f**, *n* represents the number of independent cell cultures.

expressed protein-coding genes (Extended Data Fig. 5i). Partial small interfering RNA (siRNA)-mediated knockdown of *Mcpt8* but not *Prss34* partially restored CD25 expression in T_{reg} cells (gene knockdown confirmed by qPCR and western blot; Fig. 5e and Extended Data Fig. 5j,k). Consistent with these findings, the IL-2–STAT5 pathway was the most downregulated pathway in basophil-exposed T_{reg} cells (Fig. 3d and Extended Data Fig. 5l).

To determine whether MCPT8-mediated CD25 cleavage occurs in vivo, we performed immunostaining of lungs from tumor-free *FOXP3*^{DTR} mice and spatial transcriptomic analysis of lungs from transgenic KP mice. Frequent basophil–T_{reg} cell clusters were observed and T_{reg} cells in direct contact with basophils exhibited reduced CD25 expression and IL-2–STAT5 signaling compared to more distant T_{reg} cells (Fig. 5f–h).

Consistent with these findings, scRNA-seq comparison with *Il2ra*-mutant T_{reg} cells[17] showed that basophil-exposed T_{reg} cells acquired a similar effector-like transcriptional state (Extended Data Fig. 5m). Likewise, spleen and lung T_{reg} cells from basophil-depleted tumor-free mice expressed higher levels of CD25 (Extended Data Fig. 5n,o).

Lastly, to determine whether HRH1 signaling and CD25 cleavage act independently, we treated basophil-exposed T_{reg} cells with loratadine and/or AEBSF before measuring CD8$^+$ T cell proliferation. Each inhibitor partially restored T_{reg} cell-mediated suppression of CD8$^+$ T cell proliferation, whereas the combination produced a greater

effect, indicating additive mechanisms of T_{reg} cell suppression (Fig. 5i). Together, these findings identify MCPT8-mediated CD25 cleavage as a contact-dependent mechanism by which basophils impair IL-2–STAT5 signaling in T_{reg} cells, acting in parallel with HRH1 signaling to suppress T_{reg} cell function.

Computational modeling predicts consequences of basophil-mediated anticancer cell effects

To better understand how basophils influence tumor cell killing, we developed computational models simulating coculture systems of cancer cells with immune cell subsets. Parameters were derived from our experimental data (Methods and Extended Data Fig. 5p). We tested two potential mechanisms: (1) basophils directly killing T_{reg} cells and (2) basophils inhibiting T_{reg} cell-mediated suppression of $CD8^+$ T cells, without inducing T_{reg} cell death. The results of the model predict that relief of T_{reg} cell-mediated suppression of $CD8^+$ T cells contributes more strongly to cancer cell death than direct T_{reg} cell killing. When both mechanisms are included, the effect is additive but the dominant contribution arises from T_{reg} cell suppression relief (Extended Data Fig. 5q). These predictions suggest that, in addition to inducing T_{reg} cell death, basophils may enhance antitumor immunity by relieving T_{reg} cell-mediated suppression of $CD8^+$ T cells.

Histamine levels are locally and systemically elevated in cancer

To determine whether histamine is regulated during tumor progression, we examined basophil activation and histamine synthesis in multiple tumor models. In the i.v. 4T1 model, tumor-bearing mice exhibited increased circulating basophils together with elevated HDC protein, measured by quantitative mass spectrometry (LC–MS/MS). In the s.c. 4T1 model, *Hdc* expression was higher in lung basophils (Extended Data Fig. 6a–c). Similarly, orthotopic KP tumors showed increased basophil infiltration and elevated histamine levels in serum and bone marrow (Extended Data Fig. 6d–f). Spatial transcriptomics further revealed higher *Hdc* expression in basophils located near tumor nodules than in more distant basophils (Extended Data Fig. 6g).

Together, these findings indicate that histamine production is increased both locally within the tumor microenvironment and systemically during tumor progression.

CCL24 and IgE–FcεRI engagement drive basophil recruitment and activation in cancer

To identify signals recruiting basophils to tumors, we performed NicheNet analysis of tumor-bearing and tumor-free lungs (Fig. 1a). *Ccl24* emerged as the strongest candidate, with increased expression in dendritic cells and macrophages from tumor-bearing lungs (Fig. 6a). Spatial transcriptomics showed that *Ccl24*$^+$ alveolar macrophages (AMs) localized adjacent to basophils at the tumor border (Fig. 6b) and CCL24 was increased in bronchial aspirates from participants with lung cancer (Fig. 6c).

We next investigated mechanisms of basophil activation. Bone-marrow-derived basophils expressed surface-bound IgE (Extended Data Fig. 6h). Consistent with established basophil biology[37], IL-3 priming alone did not induce histamine release but licensed basophils to respond to IgE-mediated activation. Accordingly, anti-IgE stimulation increased histamine and MCPT8 release (Fig. 6d and Extended Data Fig. 6i), enhanced basophil-mediated CD25 loss on T_{reg} cells (Extended Data Fig. 6j) and increased antigen-specific killing by OT-I $CD8^+$ T cells (Fig. 6e). Likewise, KP-conditioned medium activated basophils, increasing CD11b, CD69, CD49b and histamine release (Fig. 6f and Extended Data Fig. 6k). In vivo, lung basophils from tumor-bearing mice were enriched for an IgE-associated activation signature[38], whereas an IL-33 signature was largely absent (Extended Data Fig. 6l–o). Consistent with this and in agreement with previous reports[39,40], circulating IgE levels were elevated in tumor-bearing mice (Extended Data Fig. 6p). Together, these findings suggest that AM-derived CCL24 contributes to basophil recruitment, while IgE–FcεRI signaling may contribute to basophil activation in cancer.

Basophil-mediated T_{reg} cell suppression is conserved in humans

To validate our mouse findings, we stained basophils (2D7) and T_{reg} cells (FOXP3) in healthy lung, healthy spleen and non-small cell lung cancer (NSCLC) tissue, identifying basophil–T_{reg} cell clusters across all tissues (Fig. 7a). Analysis of a published scRNA-seq dataset of early lung adenocarcinoma[41] further revealed an inverse correlation between basophil and T_{reg} cell abundance (Fig. 7b).

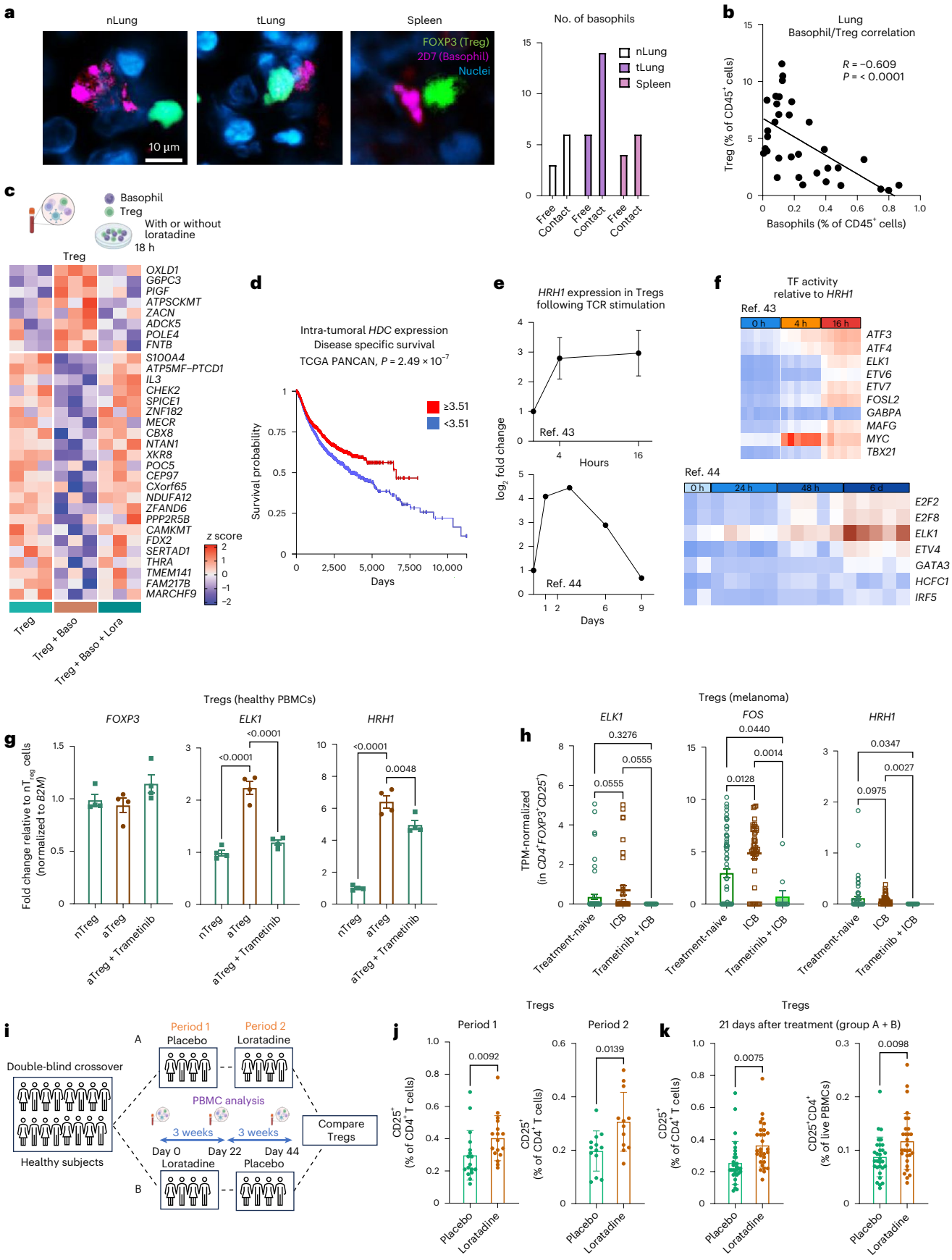
Human basophils moderately reduced T_{reg} cell viability in coculture, an effect reversed by loratadine (Extended Data Fig. 7a). Bulk RNA-seq of human basophil–T_{reg} cell cocultures identified conserved HRH1-dependent transcriptional changes, including suppression of a T_{reg} cell activation signature[42], which was reversed by loratadine (Fig. 7c and Extended Data Fig. 7b–e). Oxidative stress-induced senescence emerged as a conserved pathway across mouse and human T_{reg} cells (Extended Data Fig. 7f), supporting conservation of HRH1-mediated T_{reg} cell inhibition across species.

Consistent with our mouse studies, loratadine did not alter expression of *HDC* or protease genes in human basophils, although *IL4* expression increased (Extended Data Fig. 7g). Likewise, T_{reg} cells did not induce basophil activation (Extended Data Fig. 7h).

Lastly, high intratumoral *HDC* expression was associated with improved disease-specific survival across The Cancer Genome Atlas (TCGA) pan-cancer cohort (Fig. 7d). Together, these findings support conservation of the basophil–HRH1–T_{reg} cell axis in humans.

Fig. 7 | HRH1-mediated Basophil–T_{reg} cell crosstalk is conserved in humans. **a**, Left, representative immunofluorescence images of human T_{reg} cells (FOXP3; green) and basophils (2D7; magenta). Right, quantification of basophils free or in contact with T_{reg} cells. Cells were analyzed across >10 fields of view from one healthy/normal lung (nLung), tumor lung (tLung) or spleen. DAPI, blue. **b**, Correlation between basophil and T_{reg} cell numbers in lungs (data from a previous study[41]) ($n = 33$). **c**, Top, experimental design for bulk RNA-seq of human T_{reg} cells following basophil coculture. Bottom, heat map of basophil-regulated genes reversed by loratadine. Genes were selected using $|\log_2 \text{fold change}| > 1.5$ and $P < 0.05$ ($n = 3$). **d**, Kaplan–Meier analysis of intratumoral *HDC* expression. Participants were stratified by median *HDC* expression ($n = 5{,}282$ HDC low and $n = 5{,}154$ HDC high). **e**,**f**, The $\log_2$ fold changes in *HRH1* mRNA (**e**) and SCENIC-inferred regulon activity of transcription factors predicted to regulate HRH1 (**f**) following anti-CD3/CD28-mediated TCR stimulation of human T_{reg} cells, analyzed from previous studies[43,44] (top, $n = 5$; bottom, $n = 1$). **g**, mRNA expression of the indicated genes in human T_{reg} cells isolated from healthy PBMCs at baseline (nT_{reg}) or after 16 h anti-CD3/CD28-mediated TCR stimulation (aT_{reg}), with or without trametinib ($n = 4$). **h**, TPM-normalized expression of the indicated genes in T_{reg} cells from melanoma scRNA-seq[45]. Each dot represents one T_{reg} cell ($n = 65$ treatment-naive, $n = 42$ immune checkpoint blockade (ICB) and $n = 11$ ICB + trametinib). **i**, Clinical trial design. PBMCs were collected at baseline and after each treatment period. After dropouts, 30 placebo and 29 loratadine measurements were available. **j**, Percentage of $CD4^+CD25^+$ T_{reg} cells among $CD4^+$ T cells at the end of period 1 (left) and period 2 (right) ($n = 17$ in period 1, $n = 13$ placebo and $n = 12$ loratadine in period 2). **k**, Percentage of $CD4^+CD25^+$ T_{reg} cells within $CD4^+$ T cells (left) and live PBMCs (right). Data were pooled across both treatment periods ($n = 30$ placebo and $n = 29$ loratadine). Data are presented as the mean ± s.e.m. (**e**,**g**,**h**) or mean ± s.d. (**j**,**k**). Statistical analysis was conducted using a Pearson correlation (**b**), one-way ANOVA with Fisher's LSD test (**g**), Kruskal–Wallis test with Dunn's multiple-comparison test (**h**), two-sided Mann–Whitney test (**j**) or paired two-sided Wilcoxon signed-rank test (**k**; $n = 25$ pairs). In **c**,**e**–**g**, n represents the number of independent donors. Panels created in BioRender: **c**, De Palma Lab EPFL https://biorender.com/8yxozuz (2026); **c**,**i**, https://biorender.com/m9grmnj (2026).

https://doi.org/10.1038/s43018-026-01257-5



T cell receptor (TCR)-driven MAPK–ELK1 signaling regulates HRH1 expression in T_{reg} cells

We next explored regulators of HRH1 expression in T_{reg} cells. TCR stimulation with anti-CD3/CD28 beads upregulated *HRH1* in both mouse and human T_{reg} cells (Extended Data Fig. 7i). Analysis of two independent transcriptomic datasets of human TCR-stimulated T_{reg} cells[43,44] confirmed increased HRH1 expression within 24 h that persisted for up to 6 days following activation (Fig. 7e). To identify upstream regulators, we performed SCENIC analysis, which identified ELK1 as a candidate transcription factor. *ELK1* expression paralleled *HRH1* induction following TCR stimulation, correlated with *HRH1* across samples, and HRH1 was predicted to belong to the ELK1 regulon (Fig. 7f). To validate this pathway, we stimulated human T_{reg} cells in the presence or absence of the MEK inhibitor trametinib. Whereas *FOXP3* expression remained unchanged, TCR stimulation induced both *ELK1* and *HRH1*, and trametinib markedly reduced their expression (Fig. 7g), supporting regulation through MAPK signaling. Lastly, analysis of scRNA-seq data from individuals with melanoma treated with immunotherapy with or without trametinib[45] showed reduced expression of MEK/ERK target genes, including *FOS* and *ELK1*, together with reduced *HRH1* expression in T_{reg} cells from the trametinib-treated participant (Fig. 7h). Together, these findings support a model in which TCR-driven MAPK signaling regulates *HRH1* expression in T_{reg} cells through ELK1.

Loratadine enhances T_{reg} cells in healthy human subjects

The aforementioned findings prompted us to explore the effects of loratadine on immune parameters in humans. We conducted a prospective, double-blind, crossover clinical trial enrolling 40 healthy adult volunteers, with age and sex balanced between treatment sequence groups at randomization. Participants were randomly assigned to receive placebo followed by loratadine or the reverse sequence, each for 21 days, with peripheral blood collected at baseline and after each treatment period for immune profiling. Because of participant dropout, 30 placebo and 29 loratadine samples were available for analysis. No adverse events were reported during the study. Flow cytometry of peripheral blood mononuclear cells (PBMCs) revealed a significant increase in the proportion of T_{reg} cells ($CD4^+CD25^+$) following loratadine treatment compared to placebo (Fig. 7i–k). These findings indicate that type 1 antihistamines exert immunosuppressive effects by increasing T_{reg} cell abundance.

Multiomic integration identifies B0 and B1 basophil states conserved across models and species

Given that basophils influence tumor dynamics from the earliest stages of metastasis, we hypothesized that they adopt distinct functional states shaped by the tumor microenvironment. To test this, we integrated transcriptomic and proteomic datasets to define conserved basophil states across species.

LC–MS/MS of peripheral blood basophils from tumor-bearing and tumor-free mice (21 days after i.v. 4T1 injection) identified 937 differentially abundant proteins. We intersected these data with differentially expressed genes from lung basophils in two independent scRNA-seq datasets: a published 4T1 metastatic niche dataset[46] and our dataset of lung-infiltrating immune cells from mice with or without s.c. 4T1 tumors. This analysis identified a conserved set of genes consistently dysregulated in tumor-associated basophils (Fig. 8a).

To identify conserved basophil states across species, we integrated these mouse datasets with single-cell transcriptomic data from human colorectal cancer[47]. This analysis defined two robust signatures: a tumor-associated B1 signature ($n = 10$ genes) and a steady-state (tumor-free) B0 signature ($n = 12$ genes). The B1 signature showed minimal expression in basophils from healthy mouse lung (Extended Data Fig. 8a,b). Lastly, analysis of the metastatic lung niche across breast cancer progression[46] revealed progressive enrichment of the B1 signature, accompanied by a decline in the B0 signature (Fig. 8b).

We next assessed basophil abundance across human cancers using data from a previous study[48]. Basophil and mast cell populations were identified using a conserved human basophil/mast cell signature (*FCER1A*, *HDC*, *MS4A2*, *GATA2* and *CPA3*) derived from multiple scRNA-seq datasets[47,49–51]. Among tumor types, colorectal cancer showed the highest proportion of basophils, followed by breast and lung cancer (Extended Data Fig. 8c). We then analyzed independent datasets[50–52] from these three tumor types, in which both B0 and B1 signatures were conserved (Fig. 8c–f). Consistent with our mouse findings, basophils in healthy tissues preferentially expressed the B0 state, whereas intratumoral basophils were enriched for the B1 state.

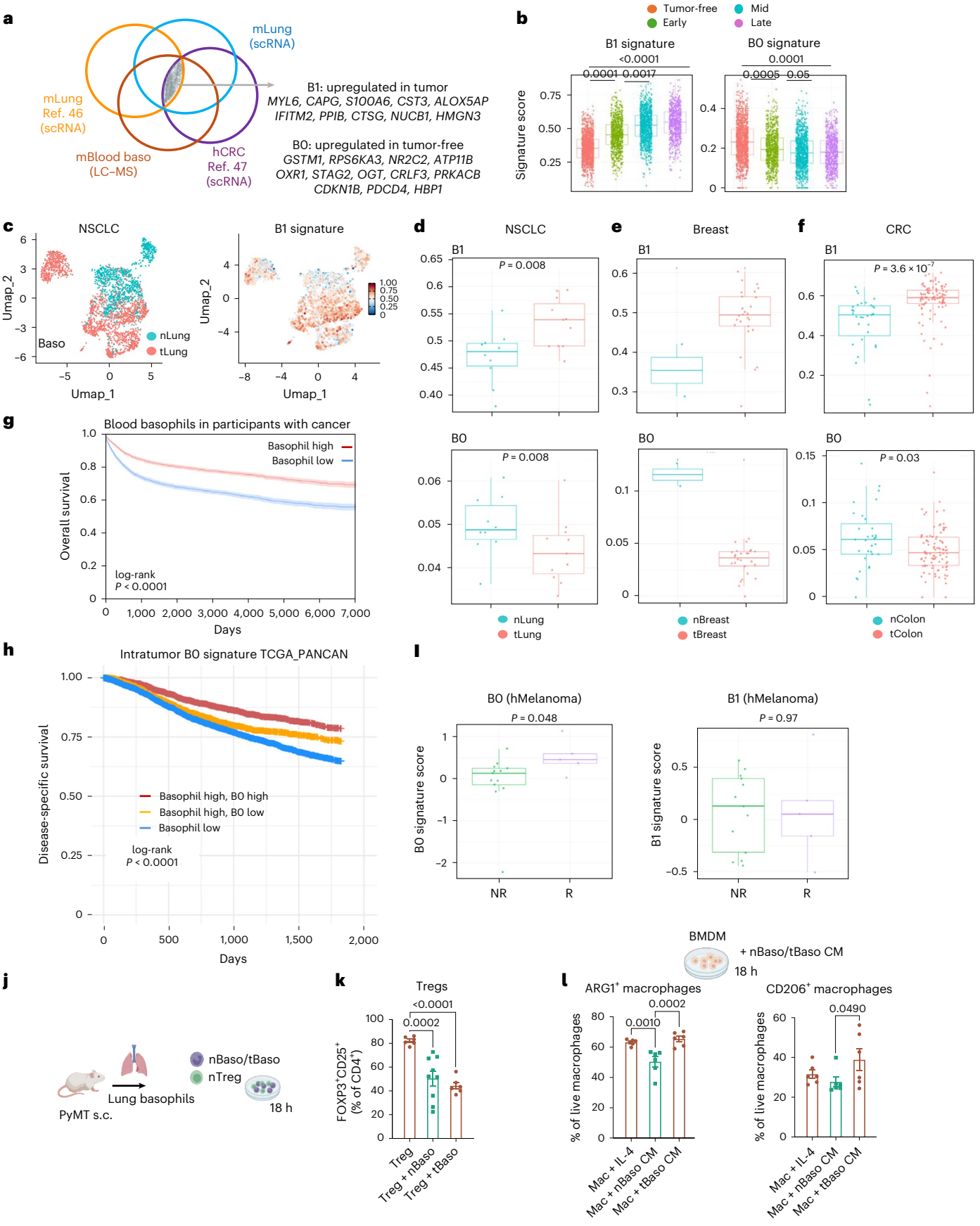
Together, these data identify two conserved basophil states across mice and humans: a steady-state B0 program enriched in tumor-free tissues and a tumor-associated B1 program that is induced within tumors and progressively enriched during tumor progression.

Basophil abundance and the B0 program predict improved survival and immunotherapy benefit in persons with cancer

To assess the association between circulating basophils and survival, we performed a retrospective analysis on 11,164 participants with cancer treated at Lausanne University Hospital (CHUV) between 2000 and 2020 using an approach similar to that described previously[53]. Participants with higher absolute blood basophil counts ($\geq 0.03 \times 10^9$ cells l^{-1}) had improved survival (Fig. 8g), a finding that was consistent across multiple tumor types, including breast and lung cancer (Extended Data Fig. 8d).

Fig. 8 | Tumors educate basophils into a conserved tumor-associated state. **a**, Venn diagram of proteins dysregulated in blood basophils from tumor-bearing mice (LC–MS; $n = 6$ tumor-free and $n = 4$ tumor-bearing mice), DEGs from two mouse lung basophil scRNA-seq datasets (our dataset: $n = 6$ tumor-free mice ($n = 3$ paclitaxel and $n = 3$ vehicle) and $n = 8$ tumor-bearing mice ($n = 2$ paclitaxel and $n = 6$ vehicle); McGinnis et al.[46]: $n = 4$ tumor-free and $n = 6$ tumor-bearing mice) and DEGs from human colorectal cancer basophils (Che et al.[47]: $n = 4$ healthy and $n = 6$ tumor samples). Conserved genes define tumor-associated B1 ($n = 10$ genes) and steady-state B0 ($n = 12$ genes) programs. **b**, B0 and B1 signature enrichment from healthy lung to metastatic disease[46]. Early, mid and late denote metastatic progression following s.c. 4T1 inoculation ($n = 4$ tumor-free mice and $n = 2$ mice at each metastatic stage); each point represents a cell. **c**, B1 signature expression in human NSCLC[50] basophil/mast cells. UMAPs show adjacent healthy lung (nLung) and tumor (tLung) cells (left) and B1 signature expression (right). Data were pooled from $n = 10$ nLung and $n = 11$ tLung samples. **d**–**f**, Participant-level B1 and B0 signature enrichment in basophil/mast cells from NSCLC[50] (**d**), breast cancer[52] (**e**) and colorectal cancer[51] (**f**) versus nontumor/healthy tissues ($n = 10$ nLung and $n = 11$ tLung (**d**), $n = 2$ nBreast and $n = 26$ tBreast (**e**), $n = 31$ nColon and $n = 97$ tColon (**f**)). **g**, Kaplan–Meier survival of participants with cancer stratified by median blood basophil count (0.03×10^9 cells l^{-1}) ($n = 5{,}071$ low and $n = 6{,}093$ high). **h**, Disease-specific survival in the pan-cancer cohort ($n = 2{,}670$ basophil high/B0 high, $n = 1{,}992$ basophil high/B0 low and $n = 4{,}668$ basophil low). **i**, B0 (left) and B1 (right) signature enrichment in melanoma responders (R) and nonresponders (NR) to anti-PD1 therapy[54] ($n = 5$ R and $n = 13$ NR). **j**, Basophils from healthy (nBaso) or orthotopic PyMT tumor-bearing (tBaso) lungs were cocultured with healthy splenic T_{reg} cells at a 1:2 ratio. **k**, $CD25^+FOXP3^+$ T_{reg} cells among $CD4^+$ T cells following coculture with nBaso or tBaso. Basophils were obtained from $n = 2$ healthy and $n = 2$ tumor-bearing mice ($n = 6$ T_{reg} alone and tBaso + T_{reg}) and $n = 9$ independent coculture wells (nBaso + T_{reg}). **l**, Top, bone-marrow-derived macrophages were exposed to conditioned medium collected from nBaso or tBaso cultured independently for 24 h. Bottom, $ARG1^+$ and $CD206^+$ macrophages among live cells ($n = 6$ independent cell cultures). Data are presented as the mean ± s.e.m. in bar plots and as box plots showing the median, interquartile range and whiskers extending to 1.5× the IQR. Statistical analysis was conducted using a two-sided pairwise *t*-test with pooled s.d. (**b**), Wilcoxon rank-sum tests with continuity correction (one-sided for **e**, two-sided for **d**,**f**), log-rank tests (**g**,**h**), unpaired two-sided Student's *t*-test (**i**) or one-way ANOVA with Fisher's LSD test (**k**,**l**). Panels created in BioRender: **j**, De Palma Lab EPFL https://biorender.com/8yxozuz (2026); **l**, De Palma Lab EPFL https://biorender.com/fxshf3b.

https://doi.org/10.1038/s43018-026-01257-5



Higher basophil counts also tended to associate with the absence of lung metastases (Extended Data Fig. 8e). Consistent with these findings, high intratumoral expression of two independent basophil signatures in TCGA and KM-Plotter cohorts predicted improved survival across multiple solid tumors (Extended Data Fig. 8f,g).

We next asked whether distinct basophil states further influence outcome. Participants whose tumors were enriched for the B0 signature exhibited the most favorable survival across breast, lung and pan-cancer datasets (Fig. 8h and Extended Data Fig. 9a–c). In a small lung cancer scRNA-seq dataset, responders to neoadjuvant immunotherapy[49] showed a trend toward higher intratumoral basophil abundance, primarily driven by the B0 subcluster (Extended Data Fig. 9d). Consistent with this, B0 enrichment also predicted response to anti-PD1 therapy in melanoma[54] (Fig. 8i).

These findings indicate that higher circulating and intratumoral basophil levels are associated with favorable prognosis and immunotherapy responsiveness and this effect is primarily driven by the B0 steady-state program.

Tumor-associated basophils acquire type 2 cytokine programs that drive M2 macrophage polarization while retaining T_{reg} cell-inhibitory capacity

We next asked whether reprogramming into the B1 state alters the ability of basophils to suppress T_{reg} cells. Splenic T_{reg} cells were cocultured with basophils isolated from the lungs of tumor-bearing (tBaso, B1; orthotopic PyMT mammary model) or tumor-free mice (nBaso, B0) (Fig. 8j,k). Both populations comparably reduced $CD25^+FOXP3^+$ T_{reg} cells. Likewise, spatial transcriptomics showed that T_{reg} cells near basophils exhibited reduced IL-2–STAT5 signaling across healthy, peritumoral and tumor regions despite increased intratumoral T_{reg} cell density (Extended Data Fig. 10a,b).

To identify mechanisms underlying the reduced protective phenotype associated with B1 enrichment, we analyzed genes and proteins upregulated in tumor-associated basophils. IL-4/IL-13 signaling was enriched in blood basophils from mammary tumor-bearing mice, with increased IL-4 and IL-13 expression confirmed in basophils from 4T1-bearing lungs and KP lung tumors by flow cytometry and scRNA-seq (Extended Data Fig. 10c–e). Consistent with previous reports[9], KP-conditioned medium induced IL-4 production, which was further enhanced by IL-3 priming (Extended Data Fig. 10f).

Given that IL-4 and IL-13 promote M2-like macrophage polarization[55], we treated bone-marrow-derived macrophages with conditioned medium from B0 or B1 basophils. Conditioned medium from B1 basophils induced a pronounced M2-like phenotype, characterized by increased CD206 and Arg1 expression, compared to medium from B0 basophils (Fig. 8l).

Together, these data show that tumor-derived cues rewire basophils across compartments into a type 2 cytokine-dominant B1 state that maintains their T_{reg} cell-inhibitory function while driving M2-like macrophage polarization, an immunoregulatory shift that likely contributes to the diminished tumor-antagonizing activity of B1 basophils.

Discussion

This study illustrates an unexpected role for basophils in suppressing early lung metastasis through regulation of T_{reg} cells, extending their established functions beyond allergy and defense against parasites[56].

We show that basophils suppress T_{reg} cells through two complementary mechanisms that enhance $CD8^+$ T cell immunity and limit early metastatic seeding. Histamine suppresses T_{reg} cells through HRH1-dependent mitochondrial stress, whereas MCPT8-mediated cleavage of IL-2Rα/CD25 disrupts IL-2–STAT5 signaling required for T_{reg} cell maintenance and function[16,17]. Consistent with these mechanisms, basophils and T_{reg} cells colocalized across mouse and human tissues. Our data further support a model in which TCR-driven MAPK signaling contributes to *HRH1* expression in T_{reg} cells, with ELK1 emerging as a candidate transcriptional regulator. Although supported by transcriptional analyses and pharmacological inhibition of the MAPK pathway, future chromatin-based studies, including ChIP-seq or CUT&RUN, will be required to determine whether ELK1 directly regulates the *HRH1* locus.

Loratadine counteracted basophil-mediated T_{reg} cell inhibition in both mouse and human coculture assays, as well as in tumor-free and tumor-bearing mice, leading to reduced effector T cell activation and enhanced lung metastatic seeding. These findings are consistent with histamine-dependent regulation of T_{reg} cell function in allergic settings[57,58] and suggest that the basophil–histamine–HRH1 axis may represent a broader mechanism of immune regulation. Whether this pathway similarly regulates T_{reg} cells in allergic or autoimmune diseases remains unknown. From a clinical perspective, retrospective studies have suggested potential benefits of antihistamines in persons with established cancers[59,60], whereas population-based studies examining associations between antihistamine use and cancer risk have yielded conflicting results[61–63].

Previous studies have reported both protumor and antitumor roles for basophils and histamine signaling[9–11,64–66]. Our findings reconcile these observations by demonstrating stage-specific functions during tumor progression. Basophils suppress early metastatic seeding, whereas tumor progression is accompanied by reprogramming into a distinct B1 state conserved across mice and humans. B1 basophils exhibit features of type 2 activation and promote M2-like macrophage polarization, providing a potential mechanism for the reduced tumor-antagonizing activity of basophils in established tumors. Despite elevated histamine levels in the tumor setting, T_{reg} cell suppression was not enhanced, possibly because of HRH1 desensitization at saturating histamine concentrations[67]. Consistent with this model, enrichment of the quiescent B0 state was associated with improved survival and enhanced response to immunotherapy.

Our findings identify macrophage-derived CCL24 and IgE–FcεRI engagement as candidate upstream pathways of basophil activation in the tumor microenvironment. Elevated IgE levels have been reported in subsets of persons with cancer[68,69] and our findings of increased circulating IgE together with enrichment of IgE-associated signatures in lung basophils support IgE-dependent basophil activation in cancer[70]. Although FcεRI signaling is classically triggered by allergen-mediated crosslinking, our data raise the possibility of nonallergic activation in tumors. Future studies should determine how IgE responses arise during tumor development and whether IgE specificity influences basophil activation.

Our experimental findings were corroborated in human studies. Higher peripheral blood basophil counts were associated with improved survival in a large retrospective cancer cohort, while two independent intratumoral basophil signatures predicted favorable prognosis across multiple cancer types. In a prospective study of healthy volunteers, loratadine increased circulating T_{reg} cells, consistent with a potential immunosuppressive effect and previous observations with the type 1 antihistamine levocetirizine in allergic rhinitis[71].

Our study had limitations. Despite including more than 10,000 participants, the retrospective cohort remains susceptible to unmeasured confounders, including comorbidities, concomitant medications and allergy status; therefore, findings should be interpreted as associative rather than causal. The prospective study was limited by its small sample size and short treatment duration and larger studies are needed to define the impact of antihistamines on cancer and immune regulation.

The basophil-mediated inhibition of T_{reg} cells and prometastatic effects of HRH1 blockade may have clinical implications. Future studies should determine whether chronic type 1 antihistamine use influences cancer development or progression and whether targeting the basophil–T_{reg} cell axis offers therapeutic opportunities in settings where this interaction is dysregulated. Our findings identify the basophil–T_{reg} cell

axis as a mechanism of immune regulation, with potential relevance to cancer and immune-mediated disease.

Methods

Ethical approvals

All animal experiments complied with relevant ethical regulations and were approved by the Cantonal Veterinary Office of Vaud (protocol nos. VD2978.2, VD3435.1, VD3785, VD3953 and VD4176) or by the Institutional Animal Care and Use Committee of Brigham and Women's Hospital.

Human buffy coats from healthy donors were obtained from the Lausanne Blood Transfusion Center under project P_297. No ethical approval was required for the use of these samples and written informed consent was obtained by the provider.

Bronchial aspirates were obtained from participants undergoing diagnostic bronchoscopy at CHUV, collected and biobanked under registry CHUV_2022_023_RM and analyzed with approval from the Cantonal Ethics Committee of Vaud (VD2022-01536). All included participants provided written institutional consent for research.

The retrospective study of participants with cancer at CHUV was approved by the Commission Cantonale d'Éthique de la Recherche sur l'Être Humain (CER-VD2020-02322). All included participants provided written institutional consent for research.

The prospective clinical trial in healthy volunteers was approved by the Shaheed Beheshti Medical University Ethics Committee (IR.SBMU.RETECH.REC.1402.304) and conducted in accordance with the Declaration of Helsinki and applicable regulations governing research involving human participants. All participants provided written informed consent and received financial compensation for participation. The trial was prospectively registered in the Iranian Registry of Clinical Trials (IRCT20170608034390N14).

Mice

We used female BALB/cJ (Jackson Laboratory, stock 000651) and FVB/NJ (Jackson Laboratory, stock 001800) mice for mammary tumor models, male C57BL/6J mice (Jackson Laboratory, stock 000664) for lung tumor models, female C57BL/6J mice for the EAE model and female OT-I mice (Jackson Laboratory, stock 003831) as T cell donors. C57BL/6J mice of either sex were used for bone marrow and spleen cell isolation. Female CD45.1 (B6.SJL-*Ptprc*^{a} *Pepc*^{b}/BoyJ#002014), *Foxp3*^{DTR} (B6.129(Cg)-*Foxp3*$^{tm3(HBEGF/GFP)Ayr}$/J; #016958) and *Kras*$^{LSL\text{-}G12D/+}$;*Trp53*$^{fl/fl}$ mice were used as indicated. BALB/cJ, C57BL/6J, FVB/NJ and OT-I mice were purchased from The Jackson Laboratory, whereas the other strains were bred in-house.

All mice were maintained under specific-pathogen-free conditions at the Swiss Federal Institute of Technology in Lausanne (EPFL), at Agora animal facilities in Lausanne or at the Brigham and Women's Hospital animal facility in Boston. Mice were housed in groups of up to five mice per cage at 18–24 °C and 40–60% humidity and maintained on a 12-h light–dark cycle (6:00 a.m. to 6:00 p.m.). Food and water were available ad libitum.

Male and female mice were used as indicated for each disease model. Sex was selected according to established experimental models and was not evaluated as an independent biological variable.

Cell lines

Mouse 4T1 cells (mammary adenocarcinoma; American Type Culture Collection, CRL-2539), 4T1 mammary cancer cells modified to express a CD9–mCh fusion protein (4T1-CD9-mCh cells)[22], PyMT (mammary adenocarcinoma, female origin)[22] cells, *Kras*^{G12D};*Tp53*^{null} lung adenocarcinoma cells[23] (KP, male origin), KP cells modified to stably express GFP using a previously described CMV.GFP.WPRE lentiviral vector (KP-GFP cells)[72] and MC38-OVA cells[73] (female origin) were cultured in DMEM (Sigma) supplemented with 10% FBS (Gibco) and penicillin–streptomycin (Gibco). All cell lines tested negative for *Mycoplasma* contamination. None of the cell lines used in this study are listed in the International Cell Line Authentication Committee database of commonly misidentified cell lines.

Primary mouse cell cultures of basophils, T_{reg} cells and $CD8^+$ cells

Bone-marrow-derived basophils were generated from C57BL/6 femurs and tibias by culture in RPMI supplemented with 10% FBS, L-glutamine, penicillin–streptomycin and recombinant mouse IL-3 (basophil medium, 2 ng ml^{-1}; R&D Systems, 403-ML) for 7 days, with medium replenished every 3 days. Basophils were purified by flow cytometric sorting as CD117$^-$FcεRI$^+$ cells. Baso-med was generated by culturing basophils at 1×10^6 cells per ml for 24 h in basophil medium; supernatants were collected for subsequent experiments. T_{reg} cells were freshly sorted from C57BL/6 splenocytes (CD4$^+$CD25^{hi}) or *Foxp3*^{DTR} splenocytes (CD4$^+$GFP$^+$) and CD8$^+$ T cells were isolated from C57BL/6 splenocytes. For suppression assay, CD8$^+$ T cells were labeled with CellTrace violet (CTV; Thermo Fisher Scientific). T_{reg} cells, CTV-labeled CD8$^+$ T cells and basophils were cocultured at a 1:2:2 ratio in DMEM containing 10% FBS, nonessential amino acids, sodium pyruvate, β-mercaptoethanol and antibiotics, in the presence of CD3/CD28 Dynabeads (2:1 T cell-to-bead ratio; Thermo Fisher Scientific, 11461D). Where indicated, T_{reg} cells were pretreated with Z-VAD-FMK (20 μM; R&D Systems, 2163) for 30 min before addition to coculture. After 72 h, CD8$^+$ T cell proliferation was assessed by flow cytometric analysis of CTV dilution. IL-3 (2 ng ml^{-1}) was included to maintain basophil viability. Where indicated, cultures were treated with loratadine (2.5–10 μM), histamine (40 μM) (Sigma-Aldrich, L9664 and H7125), AEBSF (1 mM), E64 (10 nM) or pepstatin A (1 μM) (all from Lucerna Chem). For scRNA-seq, cocultures were treated with 5 μM loratadine for 40 h.

Mouse tumor models and interventions

Experimental lung metastases were established by i.v. injection of 2×10^5 KP-GFP cells into 8-week-old male C57BL/6 mice or 2×10^4–5×10^4 4T1 or 4T1-CD9-mCh cells into 8-week-old female BALB/c mice. Tumor development was monitored by micro-CT as described previously[23,74]. Orthotopic KP lung tumors were generated by i.v. injection of multicellular KP spheroids (~50 cells per spheroid) prepared as previously described[23] and lung tumor growth was monitored by micro-CT as described[23,74]. The maximum authorized size of individual lung tumors (3 mm in diameter) was not exceeded.

The s.c. mammary tumors were induced by implantation of 7.5×10^3 or 5×10^5 4T1 or 4T1-CD9-mCh cells into the right flank of 6–8-week-old female BALB/c mice. Orthotopic mammary tumors were established by implantation of 2×10^5 PyMT cells into the mammary fat pad of 8-week-old female FVB/N mice. Tumor volume was calculated as (length × width^2)/3. The maximum authorized tumor volume (1,000 mm^3) was not exceeded.

Where indicated, mice received i.v. anti-CD200R3 antibody (clone Ba103, 20 μg per mouse; Hycult Biotech) or isotype control. Loratadine or diphenhydramine (20 mg kg^{-1} per day, Sigma) was administered orally in carboxymethyl cellulose. Where indicated, paclitaxel (10 mg kg^{-1}; Labatec) or vehicle was administered intraperitoneally every 3 days from day 17 after s.c. 4T1 tumor cell implantation, as previously described[22]. Drug administration schedules and mouse killing time points are indicated in the figures.

Macrophage polarization assay

Bone-marrow-derived macrophages (BMDMs) were generated as described previously[75] by culturing bone marrow cells in RPMI supplemented with 10% FBS, penicillin–streptomycin and murine macrophage colony-stimulating factor (50 ng ml^{-1}; BioLegend). On day 7, BMDMs were stimulated for 18 h with IL-4 (20 ng ml^{-1}; Sigma, I1020) or conditioned medium from basophils sorted from the lungs of healthy or PyMT tumor-bearing FVB/N mice. Macrophage polarization was assessed by flow cytometry using CD206 and arginase 1 staining.

Adoptive transfer of basophils

For tumor seeding experiments, 5×10^4 IL-3-cultured (7 days) basophils isolated from female BALB/c mice were injected i.v. every 3 days for a total of four injections, starting on the day of 4T1 inoculation. Mice were killed 14 days later and lungs were collected for analysis.

For tracking experiments, 2×10^6 CD45.1 bone-marrow-derived basophils were injected i.v. into transgenic KP mice with established tumors (10 weeks after lentiviral Cre injection). Bone marrow, spleen, tumor, dLNs and adjacent lung tissue were collected 1, 2 or 5 days later for flow cytometric analysis.

Tissue processing and flow cytometry

Deeply anesthetized mice were perfused with PBS before killing. Lungs were dissociated using the mouse lung dissociation kit and gentleMACS tissue dissociator (Miltenyi Biotec); tumors were digested in IMDM containing collagenase IV (0.2 mg ml^{-1}), dispase (2 mg ml^{-1}) and DNase I (0.002 mg ml^{-1}) for 20 min at 37 °C; spleens were mechanically dissociated through 70-µm strainers and blood was collected into EDTA tubes. Red blood cells were lysed (Sigma) and single-cell suspensions processed for flow cytometry. Cells were Fc-blocked with anti-CD16/CD32 (4 µg ml^{-1}, 15 min, 4 °C) and surface-stained for 30 min at 4 °C. FOXP3 and GZMB or IL-4 and IL-13 intracellular staining was performed using the FOXP3/transcription factor or intracellular fixation and permeabilization buffer sets (Thermo Fisher, 00-5523-00 and 88-8824-00, respectively). For cytokine detection, cells were stimulated for 4 h with cell activation cocktail and brefeldin A (10 µg ml^{-1}; BioLegend, 423303). Samples were acquired on an Attune NxT using single-stained compensation and fluorescence − 1 controls. Antibodies and gating strategies are provided in Supplementary Tables 2 and 3 **and** Supplementary Figs. 1–9.

Human coculture assays

PBMCs from human buffy coats were isolated by density gradient centrifugation (Lymphoprep; StemCell Technologies, 07801) and T_{reg} cells and basophils were purified by magnetic isolation (StemCell Technologies, 18063 and 17969, respectively). Cell purity was confirmed by flow cytometry (Supplementary Figs. 1–9).

T_{reg} cells were cultured in RPMI supplemented with 10% FBS, penicillin–streptomycin, nonessential amino acids and β-mercaptoethanol and activated with CD3/CD28 Dynabeads. For viability assays, T_{reg} cells were cocultured with basophils at a 1:2 ratio in the presence of IL-3 (2 ng ml^{-1}; R&D Systems, 203-IL) with or without loratadine (10 µM), for 3 days before flow cytometric analysis. For bulk RNA-seq, live T_{reg} cells and basophils were sorted by fluorescence-activated cell sorting (FACS) after 18 h of coculture and snap-frozen for downstream analysis. For qPCR, T_{reg} cells were analyzed immediately after isolation or after 16 h of anti-CD3/CD28 stimulation in the presence or absence of trametinib (10 nM).

SiRNA transfection

Basophils were transfected with *Mcpt8* or *Prss34* siRNA (Thermo Fisher Scientific, s69722 and s142171, respectively) using Lipofectamine RNAiMAX (Thermo Fisher Scientific, 13778150) according to the manufacturer's instructions. After 72 h, basophils were cocultured with T_{reg} cells for 4 h. Knockdown efficiency was confirmed by qPCR and western blotting in parallel with the coculture experiments.

Western blot analysis

Basophil proteins were extracted in RIPA buffer containing protease and phosphatase inhibitors 72 h after siRNA transfection. Equal amounts of protein were separated by SDS–PAGE, transferred to PVDF membranes and detected by chemiluminescence. For capillary western blotting, T_{reg} cells cultured alone or with basophils were sorted after 24 h, lysed in RPPA buffer and analyzed using the Jess system (ProteinSimple, Bio-Techne; 12–230-kDa separation module). DJ-1, β-actin, IL-2Rα (CD25) and HRH1 were detected by chemiluminescence and analyzed using Compass (version 6.1) with the dropped-line method. Antibodies are listed in Supplementary Table 2.

Giemsa staining

Bone-marrow-derived mouse basophils or human basophils were cytospun onto glass slides, fixed in methanol for 10 min, stained with Giemsa for 20 min, washed and imaged immediately by brightfield microscopy without mounting.

ELISA and LEGENDplex assays

Human CCL24 in bronchial aspirates from participants undergoing diagnostic bronchoscopy at CHUV was quantified by ELISA (R&D Systems, DCC240B); participants with active lung infection, asthma or severe allergies were excluded. Mouse IgE, histamine and MCPT8 in serum, lung homogenates or culture supernatants were measured using commercial assays (Invitrogen, 88-50460-88; Beckman Coulter, IM2015; MyBioSource, MBS1605303). Lung homogenates were mechanically prepared and histamine normalized to tissue weight; intracellular histamine was extracted in methanol. IL-4 and IL-13 in culture supernatants were measured using the LEGENDplex mouse Th cytokine panel (BioLegend, 740741) and analyzed using LEGENDplex software. All assays were performed according to the manufacturers' instructions.

Immunofluorescence and confocal microscopy

Mouse spleen and lung cryosections (8 µm) were methanol-fixed, whereas frozen human healthy spleen, lung and lung tumor sections (Abnova) were acetone-fixed. Sections were blocked and stained with antibodies listed in Supplementary Table 2 and DAPI. For peripheral basophil imaging, blood from *Foxp3*^{DTR} mice was stained with anti-FcεRI and DAPI and imaged by time-lapse confocal microscopy. Images were acquired using a Zeiss LSM700 or Axioscan 7 and analyzed using QuPath.

Apoptosis and mitochondrial reactive oxygen species (ROS) assays

Apoptosis was assessed using annexin V/PI flow cytometry (Thermo Fisher Scientific, A13199) or the Vybrant FLICA caspase apoptosis assay kit (Invitrogen, V35117). Mitochondrial ROS in T_{reg} cells cocultured with basophils for 18 h ± loratadine or DETA NONOate (1 mg ml^{-1}) were measured using MitoSOX green (Thermo Fisher Scientific, M36005) and quantified by flow cytometry as the mean fluorescence intensity.

OT-I cancer cell killing assay

MC38-OVA cells were cocultured with OT-I $CD8^+$ T cells, T_{reg} cells and/or basophils. Where indicated, loratadine (5 µM) or anti-IgE (1:100) was added as shown in the experimental schematics. Cancer cell death was assessed by flow cytometry as $Aqua^+$ or propidium iodide $(PI)^+$ cells among $CD45^-$ tumor cells.

Dynamic cancer cell growth assay

KP-GFP^+ cells were cultured alone or with freshly isolated basophils at a 1:5 cancer cell-to-basophil ratio in 96-well plates. Cell growth was monitored for 5 days using the IncuCyte live-cell imaging system (Sartorius), with images acquired every 2 h. GFP^+ cell numbers were quantified using IncuCyte analysis software.

LC–MS proteomic analysis

Samples were reduced, alkylated and sequentially digested with Lys-C and trypsin. Peptides were desalted, labeled with TMTpro reagents (Thermo Fisher Scientific), pooled after quality control, fractionated by high-pH reversed-phase chromatography and analyzed by nanoLC–MS/MS using a Vanquish Neo UHPLC coupled to an Orbitrap Ascend Tribrid MS instrument (Thermo Fisher Scientific).

Raw data were processed in Proteome Discoverer (version 3.0) using SEQUEST and MSFragger against the UniProt *Mus musculus* reference proteome (release 2025_03) supplemented with common contaminant proteins. Database searches were performed with trypsin specificity, allowing up to two missed cleavages. Carbamidomethylation and TMTpro modifications (lysine residues and peptide N termini) were specified as fixed modifications, whereas methionine oxidation was included as a variable modification. A 1% false discovery rate (FDR) was applied at both the peptide and the protein levels.

Protein quantification and statistical analyses were performed in R (version 4.4.2) using in-house scripts. TMT reporter intensities were normalized for sample loading, followed by trimmed mean of *M* values (TMM) normalization using edgeR (version 4.4.2). Differential protein expression was assessed using limma (version 3.62.2), and P values were adjusted using the Benjamini–Hochberg method. Proteins with an adjusted $P < 0.05$ were considered significantly differentially expressed.

EAE model

EAE was induced as previously described[76]. Briefly, 8-week-old female C57BL/6 mice were immunized s.c. with myelin oligodendrocyte glycoprotein $(MOG)_{35–55}$ peptide emulsified in complete Freund's adjuvant (CFA) containing *Mycobacterium tuberculosis* H37Ra, followed by intraperitoneal pertussis toxin administration on the day of immunization and 2 days later. Loratadine (20 mg kg^{-1} per day) or vehicle (carboxymethyl cellulose) was administered by oral gavage from 7 days before immunization until day 25. Clinical disease was assessed daily using a 0–5 neurological scoring scale. Mice were randomly assigned to treatment groups and clinical scoring was performed blinded to treatment group.

Reverse transcription PCR analysis

Total RNA was extracted using the RNeasy Micro Kit (Qiagen, 74004) according to the manufacturer's instructions. cDNA was synthesized using the high-capacity cDNA reverse transcription kit and qPCR was performed using TaqMan gene expression assays (Thermo Fisher, 4368814 and 4331182). Assay identifiers for all target and reference genes are provided in Supplementary Table 4. Gene expression was normalized to *GAPDH* or *B2M* (human samples) or *Gapdh* and *Hprt* (mouse samples) and analyzed using the $2^{-\Delta\Delta Ct}$ method.

RNA-seq and bioinformatics analysis

Mouse RNA-seq. Total RNA was extracted as above. Libraries from CD8 T cells and basophils were prepared using the NEBNext Ultra RNA library prep kit and T_{reg} cell libraries were prepared using the NEBNext single-cell/low-input cDNA synthesis and amplification module and Ultra II DNA library prep kit (New England Biolabs). Libraries were sequenced on an Illumina NovaSeq 6000 (2×150-bp reads). Reads were mapped and quantified against mm10 using STAR and Salmon (nf-core/rnaseq version 3.10.0). Counts were normalized using TMM (edgeR version 4.2.1) and voom (limma version 3.60.4) and differential expression was determined using limma. Genes with average transcripts per million (TPM) < 2 or counts < 5 per sample and uncharacterized, predicted and pseudogenes were excluded.

Human RNA-seq. Human basophils ($FC\varepsilon R1^+c\text{-}Kit^-$) and $CD4^+$ T_{reg} cells were FACS-sorted from PBMCs before or after 18 h of coculture (>99% purity). RNA was extracted using QIAzol and the RNeasy micro kit (Qiagen) and samples with DV200 > 30% were processed using the SMART-Seq stranded kit with unique molecular identifier integration and rRNA depletion (Takara Bio) and sequenced on an Aviti instrument (paired-end 75-bp reads). Reads were processed against GRCh38 using STAR, Salmon and featureCounts (nf-core/rnaseq) and normalized using TMM/voom. Genes with average TPM < 2 or counts < 5 per sample were excluded, together with pseudogenes and uncharacterized genes. For T_{reg} cells, only protein-coding genes were retained after exclusion of mitochondrial and ribosomal genes.

scRNA-seq. Lung or cultured immune cell suspensions were processed using the Chromium single-cell 3′ library and gel bead kit version 3.1 (10x Genomics) and sequenced on an Illumina NovaSeq 6000 (~20,000 reads per cell). Cell Ranger version 7.0.0 was used for processing against mm10. Downstream analyses were performed using Seurat version 5.3.0. Cells with ≥200 and <7,500 detected features and <10% mitochondrial transcripts were retained and doublets were removed using DoubletFinder version 2.0.3. Data were normalized using SCTransform, clustered using the Louvain algorithm, visualized by uniform manifold approximation and projection (UMAP) and annotated using canonical markers. Differential expression was performed using pseudobulk analysis in muscat/edgeR or Seurat FindAllMarkers, retaining genes expressed in ≥10% of cells per population per sample with average log CPM > 5.

Pathway enrichment and bioinformatic analyses. Gene set enrichment and overrepresentation analyses were performed using clusterProfiler version 4.6.2. Hallmark gene sets were obtained from msigdbr version 10.0.1. Gene expression across immune cell populations was interrogated using HPA version 23.0 and Ensembl version 109. TCGA expression and clinical data were analyzed using UCSCXenaTools version 1.4.7. Single-sample signature scores were calculated using hacksig version 0.1.2 and compared using two-sided Student's *t*-tests with Benjamini–Hochberg correction. DrugBank 6.0 was interrogated using SAveRUNNER.

IgE/IL-33 activation signature. These activation signatures were derived from published transcriptomic data[38] using genes significantly upregulated following IgE or IL-33 stimulation.

NicheNet analysis. Cell–cell communication was analyzed using NicheNet version 2.2.0. Ligands expressed in ≥5% of basophils were considered and receptors with regulatory weights < 0.2 excluded. Differentially expressed genes in receiver cells were identified by pseudobulk analysis (adjusted $P < 0.05$, $\log_2$ fold change > 0.25). The top 20 predicted ligands were used to infer ligand–receptor–target networks, visualized using ggalluvial (version 0.12.5).

Basophil B0 and B1 signature analysis

Data sources and preprocessing. Preprocessed scRNA-seq datasets were obtained from the Gene Expression Omnibus (GEO), European Genome–Phenome Archive (EGA), Figshare and CELLxGENE. Human datasets included lung cancer (GSE131907)[50], colorectal cancer (GSE178318)[51], breast cancer (EGAS00001004809)[52], pan-cancer[48] and healthy lung, colon and breast tissues from Tabula Sapiens (2022). Mouse datasets included a published 4T1 breast cancer dataset (GSE263963)[46] and our mouse lung scRNA-seq dataset. Datasets were reanalyzed using Seurat. Features detected in ≥3 cells and cells with ≥100 detected genes were retained; cells with ≥20% mitochondrial transcripts, nCount_RNA < 50 or identified as doublets using scDblFinder version 1.16.0 were excluded. Data were normalized, scaled, subjected to principal component analysis and Louvain clustering, visualized by UMAP and annotated using canonical markers. For datasets lacking raw counts, normalized expression matrices from the original study were used.

B0 and B1 signature generation and validation. Steady-state (B0) and tumor-associated (B1) basophil signatures were derived by intersecting dysregulated genes or proteins across four independent datasets: (1) our mouse lung scRNA-seq, which included both tumor-free and tumor-bearing mice, either untreated or treated with paclitaxel; (2) our blood basophil proteomic dataset; (3) a published mouse lung

scRNA-seq dataset[46]; and (4) a human colorectal cancer scRNA-seq dataset[47]. Mouse basophils were identified by *Mcpt8, Hdc* and *Cpa3*, pseudobulked by biological replicate and analyzed using DESeq2 (version 1.42.1). Human basophils were identified by *FCER1A, HDC, MS4A2, GATA2* and *CPA3* and differential expression was determined using Seurat FindMarkers. Genes with adjusted $P < 0.05$ were retained and assigned to B1 or B0 according to their direction of change in tumor-associated versus tumor-free basophils. Proteomic differential abundance analysis was performed as described above, retaining proteins with FDR < 0.05 and assigning them to B1 or B0 according to their direction of change. The resulting B0 and B1 signatures were independently validated using UCell (AddModuleScore_UCell) in mouse and human basophil scRNA-seq datasets[50–52] and Tabula Sapiens.

Human transcriptomic and survival analyses

Melanoma T_{reg} cell analysis. scRNA-seq data and clinical annotations from individuals with melanoma were obtained from a previous study[45]. T_{reg} cells were defined as $CD4^+FOXP3^+CD25^+$ cells and assigned to treatment groups according to the original clinical annotations. Transcriptional regulatory networks were inferred using SCENIC (version 1.3.1) on GSE94396 and a previous dataset[43]. Regulon activity was quantified using AUCell (version 1.24.0) and specificity assessed using regulon specificity scores.

Association of intratumoral basophils with survival. For KM-Plotter analyses, basophil abundance was estimated from the combined expression of *IL3RA, CCR3* and *FCER1A*. Participants were stratified into tertiles and survival was compared between highest (T3) and lowest (T1) tertiles using the log-rank test. Kaplan–Meier curves were reformatted using the survival and ggsurvfit R packages.

For TCGA and METABRIC analyses, primary tumor expression and survival data were obtained through cBioPortal. Gene expression was z-score normalized using hacksig. Kaplan–Meier analyses used survival (version 3.8-3) and survminer (version 0.5.1), with follow-up censored at 5 years and significance assessed by log-rank test. Tumors were stratified by expression of basophil genes (see above) and basophil-high tumors were further classified by B0 and B1 signatures.

Lung basophil–T_{reg} cell correlation. Lung tumor and adjacent normal scRNA-seq/CITE-seq data were obtained from a previous study[77]. Basophils were identified as $CD123^+CD117^-FCER1A^+CCR3^+$ cells, with *TPSAB1/TPSB2* as ancillary markers, and T_{reg} cells were identified by *CD4, IL2RA* and *FOXP3*. Samples containing <1,000 or >10,000 cells, generated using older library protocols or lacking CD45 enrichment were excluded. Pearson correlation was used to assess the association between basophil and T_{reg} cell abundance.

Visium HD spatial transcriptomics

Processing and analysis. KP lungs were isolated 127 days after intratracheal lentiviral Cre delivery, embedded in OCT and processed using the 10x Genomics Visium HD CytAssist FFPE workflow. Libraries were sequenced on NovaSeq 6000 and Aviti platforms and processed using Space Ranger (version 3.1.0) against mm10-2020-A. Visium HD data were imported using bin2cell (version 0.3.3), spatial striping was corrected using destripe and expression counts were normalized and log-transformed using Scanpy (version 1.11.2).

Nuclei were segmented using StarDist (2D_versatile_he) in bin2cell and expanded to approximate whole-cell boundaries. Transcript counts were aggregated at cell level and cells were annotated in Seurat using mouse lung scRNA-seq-derived signatures quantified with UCell. Spatial visualizations were generated using B2CViz (version 1.0.0).

Spatial proximity analysis. Euclidean distances between T_{reg} cells and the nearest basophil were calculated using get.knnx (FNN version 1.1.4), with T_{reg} cells classified as near or far using a 50-µm threshold. IL-2–STAT5 Hallmark pathway activity was quantified using UCell and groups were compared using pairwise *t*-tests in ggpubr (version 0.6.1).

Association of blood basophil counts with survival

Adult participants with a primary malignant tumor diagnosed at CHUV between 2000 and 2020 and institutional research consent were included; participants with benign tumors and carcinoma in situ were excluded. Absolute blood basophil counts were available for 11,164 participants. After removing duplicate measurements and median-imputing missing values, mean basophil counts from diagnosis to death, last follow-up or data extraction were calculated as previously described[53]. Participants were stratified by the median basophil count ($0.03 \times 10^9 l^{-1}$) and survival was compared by Kaplan–Meier analysis and log-rank test using lifelines (version 0.27.8).

Prospective clinical trial

We conducted a randomized, double-blind, placebo-controlled crossover trial involving 40 healthy adult volunteers. Recruitment was conducted between June 21 and August 21, 2024. The trial is reported in accordance with the CONSORT 2010 guidelines, and the study protocol and completed CONSORT checklist are provided in the Supplementary Information. Both male and female healthy volunteers aged 20–30 years were enrolled. Biological sex was self-reported and recorded as a biological variable. The study was not designed or powered to detect sex-specific differences. Baseline age and sex were balanced between treatment sequence groups at randomization.

Participants were randomized 1:1 (10 blocks of four) to placebo followed by loratadine or vice versa using Sealed Envelope. Drug and placebo were identically packaged and coded by an independent clinical laboratory expert. Participants, investigators and outcome assessors were blinded and allocation was concealed from the data analyst until analysis completion. Participants received loratadine (10 mg daily) or placebo for 21 days per period without washout. The primary endpoint was the change in T_{reg} cell frequency following loratadine compared to placebo. The prespecified secondary endpoint was the number of $CD8^+$ effector T cells; this outcome is not reported here as it was outside the scope of the present study, which focused on basophil–T_{reg} cell interactions.

Peripheral blood was collected at the end of each treatment period. PBMCs were isolated and analyzed by flow cytometry following staining with CD4–FITC and CD25–PE antibodies (BioLegend). T_{reg} cells were identified as $CD4^+CD25^+$ lymphocytes using FMO controls for gating.

Six participants withdrew before day 22. An additional four participants in group A and five in group B missed the day 42 blood draw, resulting in 29 loratadine-treated and 30 placebo-treated samples. Paired crossover analyses included only complete treatment pairs (participant characteristics in Supplementary Table 1)

Data distribution was assessed using Shapiro–Wilk, D'Agostino–Pearson, Anderson–Darling and Kolmogorov–Smirnov tests together with quantile–quantile plots. Because the data were not normally distributed, unpaired comparisons were performed using the Mann–Whitney test and paired crossover analyses using the Wilcoxon signed-rank test. Sample size was estimated from a previous study[78] assuming a 20% treatment effect, $\alpha = 0.05$ and 80% power, requiring 32 participants. To account for an anticipated 20% dropout rate, 40 participants were enrolled.

Mathematical modeling of cell interactions

A mechanistic ordinary differential equation model describing interactions among cancer cells, T_{reg} cells, $CD8^+$ T cells and basophils was implemented in MATLAB using the ode15s solver and mass-action kinetics[79] (Extended Data Fig. 5q). Initial cell numbers and experimental timing matched the in vitro assays. Parameters governing proliferation, death and immune interactions, including basophil-mediated T_{reg} cell apoptosis and inhibition of T_{reg} cell-mediated $CD8^+$ T cell

suppression, were fitted to experimental measurements. Model files and equations are available from GitHub (https://github.com/FinleyLabUSC/Basophil-immune-model/) and Zenodo (https://doi.org/10.5281/zenodo.22773668)[80]. Parameter values are provided in Supplementary Table 5.

Statistical analysis and reproducibility

Experiments involving independent mouse cohorts were conducted one to two times, with sample sizes selected on the basis of prior experience with the respective tumor models and our previous studies[22,23]; no statistical methods were used to predetermine sample size. Reproducibility was assessed across independent experiments and complementary experimental models addressing the same biological questions. Randomization was not performed for the metastatic lung models, in which treatment groups were defined before or at the time of tumor inoculation. For studies involving established disease, mice were randomized to treatment groups before treatment initiation, where applicable. Experimental endpoints were defined according to the approved animal protocols and the permitted maximal tumor burden was not exceeded. Drug administration was performed by investigators aware of group allocation.

Investigators were blinded to group allocation during tumor growth measurements, immunofluorescence acquisition and quantification and flow cytometry acquisition where applicable. Flow cytometry analysis was not blinded because of manual gating and access to experimental codes. No data points were excluded as outliers. In rare instances, individual samples were excluded from specific analyses because of technical failures during sample collection, processing or data acquisition. For mouse primary cell experiments, each value represents an independent primary cell coculture, in which primary cells were independently assembled and treated in separate wells. Each well constitutes an independently established biological culture and was subjected to the experimental conditions independently. Accordingly, individual wells were considered independent biological replicates for the purpose of assessing variability and treatment effects. Experiments involving human primary cells used independent donors, with sample sizes indicated in the figure legends.

Graphs were generated using Prism (GraphPad Software) or R. Data are presented as the mean ± s.e.m. unless otherwise indicated. Individual data points are shown whenever possible. Normality was assessed using the Shapiro–Wilk test. Equality of variances was not formally tested. Comparisons were performed using Student's or Welch's *t*-tests, Mann–Whitney or Wilcoxon tests, analysis of variance, Fisher's exact tests, log-rank tests or permutation-based analyses, as specified in the figure legends. Initial exploratory analyses used two-sided tests. One-sided tests were used for subsequent experiments addressing prespecified directional hypotheses; otherwise, two-sided tests were applied. Multiple comparisons were performed using a one-way analysis of variance (ANOVA) followed by Fisher's least significant difference (LSD) test, multiple paired *t*-tests or Benjamini–Hochberg correction, as indicated. Exact *P* values are shown in the figures, except when $P < 0.0001$.

For the prospective randomized crossover clinical trial, analyses were performed using paired statistical methods. Given evidence of nonnormal distribution, treatment comparisons between placebo and loratadine were conducted using the Wilcoxon signed-rank test. Data are presented as the mean ± s.d., unless otherwise indicated. Schematics included in this study were created with BioRender.com under a publication license.

Reporting summary

Further information on research design is available in the Nature Portfolio Reporting Summary linked to this article.

Data availability

Sequencing and spatial transcriptomics data generated in this study are available from the GEO under accession codes GSE266677 and GSE341382. MS proteomics data are available through PRIDE under dataset identifier PXD082224. Publicly available datasets used in this study are also available from the GEO under accession codes GSE131907, GSE178318, GSE263963 and GSE94396. The study protocol is included in the Supplementary Information. Individual-level clinical data from retrospective studies and biobanked biological samples cannot be made publicly available because access is restricted under the approved study protocols and applicable institutional data protection requirements. Requests for access for academically led research may be considered subject to the relevant institutional and ethical approvals and appropriate data or material transfer agreements. The remaining data are available within the article and its Supplementary Information. Source data are provided with this paper.

Code availability

The mathematical model and custom code developed for the cell-interaction simulations in this study are publicly available from Zenodo (https://doi.org/10.5281/zenodo.22773668)[80].

References

1. Mitre, E. & Nutman, T. B. Basophils, basophilia and helminth infections. *Chem. Immunol. Allergy* **90**, 141–156 (2006).
2. Siracusa, M. C., Kim, B. S., Spergel, J. M. & Artis, D. Basophils and allergic inflammation. *J. Allergy Clin. Immunol.* **132**, 789–801 (2013).
3. Marone, G. et al. Is there a role for basophils in cancer? *Front. Immunol.* **11**, 2103 (2020).
4. Hiltbrunner, S. et al. Comprehensive statistical exploration of prognostic (bio-)markers for responses to immune checkpoint inhibitor in patients with non-small cell lung cancer. *Cancers (Basel)* **14**, 75 (2021).
5. Wei, J. et al. IL3-driven T cell–basophil crosstalk enhances antitumor immunity. *Cancer Immunol. Res.* **12**, 822–839 (2024).
6. Merrill, R. M., Isakson, R. T. & Beck, R. E. The association between allergies and cancer: what is currently known? *Ann. Allergy Asthma Immunol.* **99**, 102–116 (2007).
7. Fereidouni, M., Ferns, G. A. & Bahrami, A. Current status and perspectives regarding the association between allergic disorders and cancer. *IUBMB Life* **72**, 1322–1339 (2020).
8. Karim, A. F., Westenberg, L. E. H., Eurelings, L. E. M., Otten, R. & Gerth van Wijk, R. The association between allergic diseases and cancer: a systematic review of the literature. *Neth. J. Med.* **77**, 42–66 (2019).
9. LaMarche, N. M. et al. An IL-4 signalling axis in bone marrow drives pro-tumorigenic myelopoiesis. *Nature* **625**, 166–174 (2024).
10. Li, H. et al. The allergy mediator histamine confers resistance to immunotherapy in cancer patients via activation of the macrophage histamine receptor H1. *Cancer Cell* **40**, 36–52 (2022).
11. Chryplewicz, A. et al. Cancer cell autophagy, reprogrammed macrophages, and remodeled vasculature in glioblastoma triggers tumor immunity. *Cancer Cell* **40**, 1111–1127 (2022).
12. Imianowski, C. J., Chen, Q., Workman, C. J. & Vignali, D. A. A. Regulatory T cells in the tumour microenvironment. *Nat. Rev. Cancer* **25**, 703–722 (2025).
13. Noval Rivas, M. & Chatila, T. A. Regulatory T cells in allergic diseases. *J. Allergy Clin. Immunol.* **138**, 639–652 (2016).
14. Verreycken, J., Baeten, P. & Broux, B. Regulatory T cell therapy for multiple sclerosis: breaching (blood–brain) barriers. *Hum. Vaccin. Immunother.* **18**, 2153534 (2022).
15. Koutrolos, M., Berer, K., Kawakami, N., Wekerle, H. & Krishnamoorthy, G. Treg cells mediate recovery from EAE by controlling effector T cell proliferation and motility in the CNS. *Acta Neuropathol. Commun.* **2**, 163 (2014).

16. Chinen, T. et al. An essential role for the IL-2 receptor in Treg cell function. *Nat. Immunol.* **17**, 1322–1333 (2016).
17. Permanyer, M. et al. Efficient IL-2R signaling differentially affects the stability, function, and composition of the regulatory T-cell pool. *Cell. Mol. Immunol.* **18**, 398–414 (2021).
18. Wardell, C. M., MacDonald, K. N., Levings, M. K. & Cook, L. Cross talk between human regulatory T cells and antigen-presenting cells: lessons for clinical applications. *Eur. J. Immunol.* **51**, 27–38 (2021).
19. Kojima, T. et al. Mast cells and basophils are selectively activated in vitro and in vivo through CD200R3 in an IgE-independent manner. *J. Immunol.* **179**, 7093–7100 (2007).
20. Obata, K. et al. Basophils are essential initiators of a novel type of chronic allergic inflammation. *Blood* **110**, 913–920 (2007).
21. Nakamura, T. et al. Selective depletion of basophils ameliorates immunoglobulin E-mediated anaphylaxis. *Biochem. Biophys. Rep.* **9**, 29–35 (2017).
22. Keklikoglou, I. et al. Chemotherapy elicits pro-metastatic extracellular vesicles in breast cancer models. *Nat. Cell Biol.* **21**, 190–202 (2019).
23. Martinez-Usatorre, A. et al. Overcoming microenvironmental resistance to PD-1 blockade in genetically engineered lung cancer models. *Sci. Transl. Med.* **13**, eabd1616 (2021).
24. Ohue, Y. & Nishikawa, H. Regulatory T (Treg) cells in cancer: can Treg cells be a new therapeutic target? *Cancer Sci.* **110**, 2080–2089 (2019).
25. Sato, K. et al. Naturally occurring regulatory dendritic cells regulate murine cutaneous chronic graft-versus-host disease. *Blood* **113**, 4780–4789 (2009).
26. Mahmud, S. A., Manlove, L. S. & Farrar, M. A. Interleukin-2 and STAT5 in regulatory T cell development and function. *JAKSTAT* **2**, e23154 (2013).
27. Yan, R. et al. A structure of human Scap bound to Insig-2 suggests how their interaction is regulated by sterols. *Science* **371**, eabb2224 (2021).
28. Wherry, E. J. et al. Molecular signature of $CD8^+$ T cell exhaustion during chronic viral infection. *Immunity* **27**, 670–684 (2007).
29. Borriello, F., Iannone, R. & Marone, G. Histamine release from mast cells and basophils. *Handb. Exp. Pharmacol.* **241**, 121–139 (2017).
30. Simons, F. E. Loratadine, a non-sedating H1-receptor antagonist (antihistamine). *Ann. Allergy* **63**, 266–268 (1989).
31. Yu, A., Zhu, L., Altman, N. H. & Malek, T. R. A low interleukin-2 receptor signaling threshold supports the development and homeostasis of T regulatory cells. *Immunity* **30**, 204–217 (2009).
32. Pos, Z. et al. Histamine suppresses fibulin-5 and insulin-like growth factor-II receptor expression in melanoma. *Cancer Res.* **68**, 1997–2005 (2008).
33. Miragaia, R. J. et al. Single-cell transcriptomics of regulatory T cells reveals trajectories of tissue adaptation. *Immunity* **50**, 493–504 (2019).
34. O'Brien, M. A. & Kirby, R. Apoptosis: a review of pro-apoptotic and anti-apoptotic pathways and dysregulation in disease. *J. Vet. Emergen. Crit. Care* **18**, 572–585 (2008).
35. Chapman, N. M. & Chi, H. mTOR signaling, Tregs and immune modulation. *Immunotherapy* **6**, 1295–1311 (2014).
36. Sharma, M. et al. Regulatory T cells induce activation rather than suppression of human basophils. *Sci. Immunol.* **3**, eaan0829 (2018).
37. Jensen, B. M., Bartko, E. A., Baumann, K. & Skov, P. S. Measuring histamine and cytokine release from basophils and mast cells. In *Basophils and Mast Cells* (eds Gibbs, B. F. & Falcone, F. H.) (Springer, 2020).
38. Chhiba, K. D., Hsu, C.-L., Berdnikovs, S. & Bryce, P. J. Transcriptional heterogeneity of mast cells and basophils upon activation. *J. Immunol.* **198**, 4868–4878 (2017).
39. Zhou, D. et al. Elevated serum total immunoglobulin E is associated with an increased risk of lung cancer: a retrospective study. *Front. Immunol.* **16**, 1637803 (2025).
40. Hällgren, R. et al. Elevated serum immunoglobulin E in bronchial carcinoma: its relation to the histology and prognosis of the cancer. *J. Allergy Clin. Immunol.* **67**, 398–406 (1981).
41. Leader, A. M. et al. Single-cell analysis of human non-small cell lung cancer lesions refines tumor classification and patient stratification. *Cancer Cell* **39**, 1594–1609 (2021).
42. Ohkura, N. & Sakaguchi, S. Transcriptional and epigenetic basis of Treg cell development and function: its genetic anomalies or variations in autoimmune diseases. *Cell Res.* **30**, 465–474 (2020).
43. Moro, A. et al. Growth of human regulatory $CD4^+$ T cells is more tightly controlled than effector T cells due to distinctive molecular programming. *iScience* **28**, 112553 (2025).
44. Schmidt, A. et al. Time-resolved transcriptome and proteome landscape of human regulatory T cell (Treg) differentiation reveals novel regulators of FOXP3. *BMC Biol.* **16**, 47 (2018).
45. Jerby-Arnon, L. et al. A cancer cell program promotes T cell exclusion and resistance to checkpoint blockade. *Cell* **175**, 984–997 (2018).
46. McGinnis, C. S. et al. The temporal progression of lung immune remodeling during breast cancer metastasis. *Cancer Cell* **42**, 1018–1031 (2024).
47. Che, L.-H. et al. A single-cell atlas of liver metastases of colorectal cancer reveals reprogramming of the tumor microenvironment in response to preoperative chemotherapy. *Cell Discov.* **7**, 80 (2021).
48. Guimarães, G. R. et al. Single-cell resolution characterization of myeloid-derived cell states with implication in cancer outcome. *Nat. Commun.* **15**, 5694 (2024).
49. Hu, J. et al. Tumor microenvironment remodeling after neoadjuvant immunotherapy in non-small cell lung cancer revealed by single-cell RNA sequencing. *Genome Med.* **15**, 14 (2023).
50. Kim, N. et al. Single-cell RNA sequencing demonstrates the molecular and cellular reprogramming of metastatic lung adenocarcinoma. *Nat. Commun.* **11**, 2285 (2020).
51. Chu, X. et al. Integrative single-cell analysis of human colorectal cancer reveals patient stratification with distinct immune evasion mechanisms. *Nat Cancer* **5**, 1409–1426 (2024).
52. Bassez, A. et al. A single-cell map of intratumoral changes during anti-PD1 treatment of patients with breast cancer. *Nat. Med.* **27**, 820–832 (2021).
53. Jamshidi, E. et al. Medical and personal characteristics can predict the risk of lung metastasis. *Clin. Oncol. (R. Coll. Radiol.)* **35**, e362–e375 (2023).
54. Hugo, W. et al. Genomic and transcriptomic features of response to anti-PD-1 therapy in metastatic melanoma. *Cell* **165**, 35–44 (2016).
55. Wynn, T. A. & Vannella, K. M. Macrophages in tissue repair, regeneration, and fibrosis. *Immunity* **44**, 450–462 (2016).
56. Voehringer, D. The role of basophils in helminth infection. *Trends Parasitol.* **25**, 551–556 (2009).
57. Forward, N. A., Furlong, S. J., Yang, Y., Lin, T.-J. & Hoskin, D. W. Mast cells down-regulate $CD4^+CD25^+$ T regulatory cell suppressor function via histamine H1 receptor interaction. *J. Immunol.* **183**, 3014–3022 (2009).
58. Conrad, M. L. et al. Regulatory T cells and their role in allergic disease. *Allergy* **80**, 77–93 (2025).
59. Chiang, C.-H. et al. Efficacy of cationic amphiphilic antihistamines on outcomes of patients treated with immune checkpoint inhibitors. *Eur. J. Cancer* **174**, 1–9 (2022).
60. Fritz, I., Wagner, P. & Olsson, H. Improved survival in several cancers with use of H1-antihistamines desloratadine and loratadine. *Transl. Oncol.* **14**, 101029 (2021).

61. Chan, S.-Y., Chang, Y., Polpichai, N., Lee, Y.-T. & Ma, K. S.-K. Treatment with antihistamines and the risk of liver cancer in patients with viral hepatitis: a multi-center cohort study. *Viruses* **16**, 940 (2024).
62. Peng, J.-Y. et al. Association of antihistamine use with increased risk of esophageal squamous cell carcinoma: a nationwide, long-term follow-up study using propensity score matching. *Biomedicines* **11**, 578 (2023).
63. Chen, Y.-N. et al. H1-antihistamine use and head and neck cancer risk in type 2 diabetes mellitus. *Oncol. Res.* **31**, 23–34 (2023).
64. Sektioglu, I. M. et al. Basophils promote tumor rejection via chemotaxis and infiltration of $CD8^+$ T cells. *Cancer Res.* **77**, 291–302 (2017).
65. Yang, X. D. et al. Histamine deficiency promotes inflammation-associated carcinogenesis through reduced myeloid maturation and accumulation of $CD11b^+Ly6G^+$ immature myeloid cells. *Nat. Med.* **17**, 87–95 (2011).
66. Grauers Wiktorin, H. et al. Histamine targets myeloid-derived suppressor cells and improves the anti-tumor efficacy of PD-1/PD-L1 checkpoint blockade. *Cancer Immunol. Immunother.* **68**, 163–174 (2019).
67. Pantazaka, E., Taylor, E. J. A., Bernard, W. G. & Taylor, C. W. Ca^{2+} signals evoked by histamine H1 receptors are attenuated by activation of prostaglandin EP2 and EP4 receptors in human aortic smooth muscle cells. *Br. J. Pharmacol.* **169**, 1624–1634 (2013).
68. Lal, H., Singh, B., Wig, U. & Saini, A. S. Serum immunoglobulin E levels in patients with head and neck cancer. *J. Laryngol. Otol.* **102**, 432–434 (1988).
69. Josephs, D. H., Spicer, J. F., Corrigan, C. J., Gould, H. J. & Karagiannis, S. N. Epidemiological associations of allergy, IgE and cancer. *Clin. Exp. Allergy* **43**, 1110–1123 (2013).
70. Schroeder, J. T., Ehrlich, L. & Bieneman, A. P. Basophils induce protumorigenic cytokines from A549 lung adenocarcinoma via mechanisms requiring IgE, galectin-3, and IL-3 priming. *J. Leukoc. Biol.* **117**, qiae233 (2025).
71. Mahmoud, F., Arifhodzic, N., Haines, D. & Novotney, L. Levocetirizine modulates lymphocyte activation in patients with allergic rhinitis. *J. Pharmacol. Sci.* **108**, 149–156 (2008).
72. Squadrito, M. L., Cianciaruso, C., Hansen, S. K. & De Palma, M. EVIR: chimeric receptors that enhance dendritic cell cross-dressing with tumor antigens. *Nat. Methods* **15**, 183–186 (2018).
73. Ghasemi, A. et al. Cytokine-armed dendritic cell progenitors for antigen-agnostic cancer immunotherapy. *Nat. Cancer* **5**, 240–261 (2024).
74. Duval, F. et al. Trajectories of macrophage ontogeny and reprogramming in cancer. *iScience* **28**, 112498 (2025).
75. Mansouri, N. et al. Mesenchymal stromal cell exosomes prevent and revert experimental pulmonary fibrosis through modulation of monocyte phenotypes. *JCI Insight* **4**, e128060 (2019).
76. Sanmarco, L. M. et al. Lactate limits CNS autoimmunity by stabilizing HIF-1α in dendritic cells. *Nature* **620**, 881–889 (2023).
77. Lavin, Y. et al. Innate immune landscape in early lung adenocarcinoma by paired single-cell analyses. *Cell* **169**, 750–765 (2017).
78. Bock, G. et al. The effect of vitamin D supplementation on peripheral regulatory T cells and β cell function in healthy humans: a randomized controlled trial. *Diabetes Metabolism Res.* **27**, 942–945 (2011).
79. de Pillis, L. G., Radunskaya, A. E. & Wiseman, C. L. A validated mathematical model of cell-mediated immune response to tumor growth. *Cancer Res.* **65**, 7950–7958 (2005).
80. Finley, S. Code for: Basophils inhibit early lung metastasis by suppressing regulatory T cells. *Zenodo* https://doi.org/10.5281/zenodo.22773668 (2026).

Acknowledgements

We thank E. Jamshidi (Johns Hopkins University) for assistance with the prospective clinical trial, A. Guichard (EPFL) for help with some experiments, D. Labes and M. Castelblanco (Flow Cytometry Facility, Agora), along with B. Mangeat (Gene Expression Core Facility, EPFL), for performing scRNA-seq, R. Hamelin (Proteomic Core Facility, EPFL) and S. Lorrain (Protein Analysis Facility, University of Lausanne) for performing capillary western blot analysis and M. Merad (Mount Sinai Medical School) and N. La Marche (Yale School of Medicine) for their advice on the manuscript.

Author contributions

B.T., S.Y., Y.M., A.G., E.M., L.L., C.F., A.M.S., T.S., M. Manco, C.W.R. and N.M. designed and performed the experiments and analyzed the data. N.F., M.F., S.S., J.L. and S.D.F. performed the bioinformatics, computational and statistical analyses. H.E., M. Mesdaghi and S.N.B. designed and conducted the prospective clinical trial. N.U. and C.v.G. coordinated the retrospective clinical cohort. B.T. and C.W.R. managed the mouse colonies. N.M., M.D.P., F.J.Q. and M. Mazzone conceptualized and supervised the study and interpreted the results. N.M. coordinated the study and wrote the manuscript with contributions from all authors. M.D.P. and N.M. secured funding for the study. All authors reviewed and approved the final manuscript.

Funding

This study was supported by grants from the Swiss Institute for Experimental Cancer Research (ISREC) Foundation (to N.M. and M.D.P.), ISREC Bridge fellowship (to N.M.), Swiss Cancer League (KFS-5433-08-2021 to N.M. and C.v.G.) and Swiss National Science Foundation (310030-188868 to M.D.P.). The funders had no role in study design, data collection and analysis, decision to publish or preparation of the manuscript. Open access funding provided by University of Lausanne.

Competing interests

The authors declare no competing interests.

Additional information

Extended data is available for this paper at https://doi.org/10.1038/s43018-026-01257-5.

Supplementary information The online version contains supplementary material available at https://doi.org/10.1038/s43018-026-01257-5.

Correspondence and requests for materials should be addressed to Nahal Mansouri.

Peer review information *Nature Cancer* thanks Ilaria Malanchi, Hiroyoshi Nishikawa, Lina Serna-Hinguita and the other, anonymous, reviewer(s) for their contribution to the peer review of this work.

Reprints and permissions information is available at www.nature.com/reprints.

Publisher's note Springer Nature remains neutral with regard to jurisdictional claims in published maps and institutional affiliations.

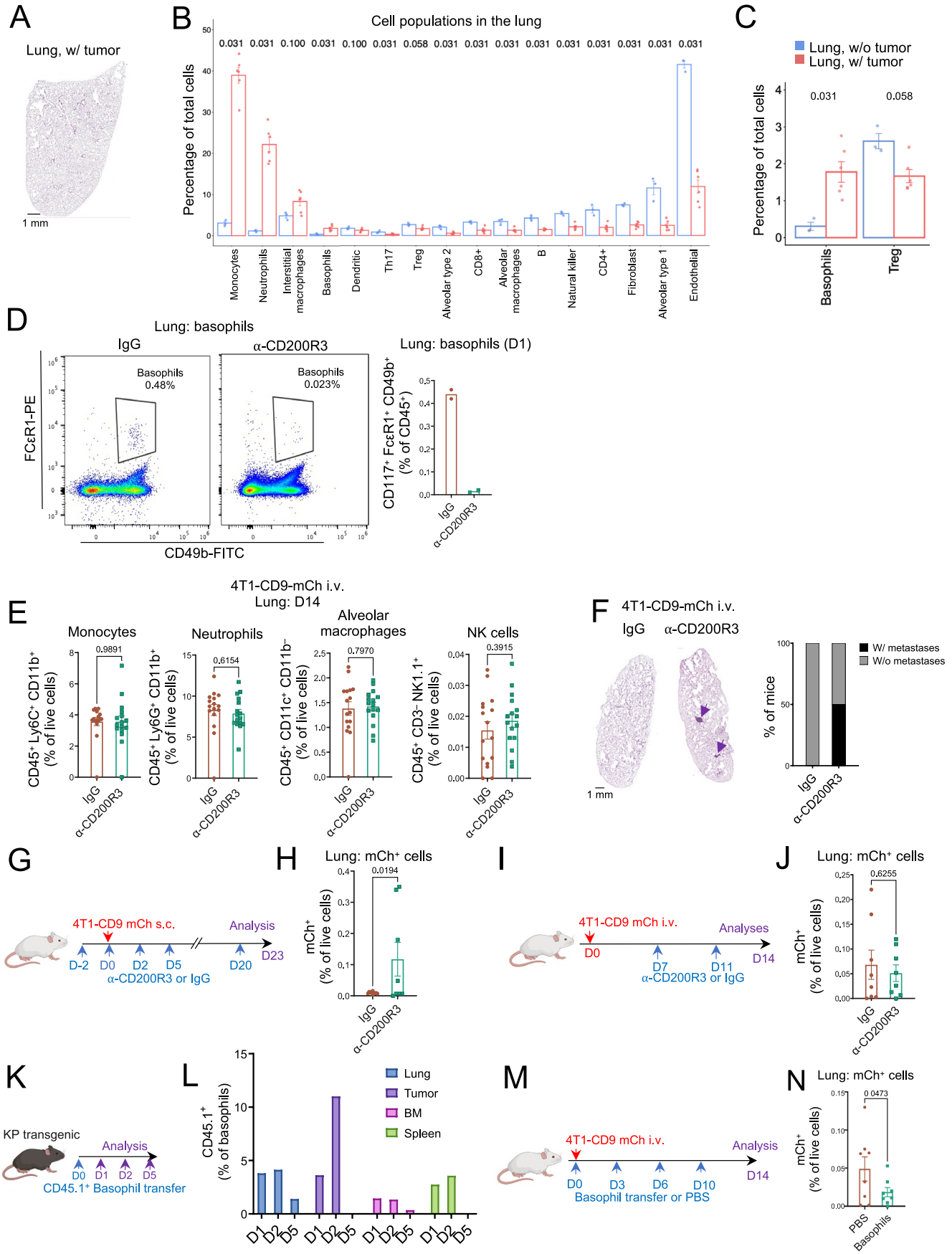
Open Access This article is licensed under a Creative Commons Attribution 4.0 International License, which permits use, sharing, adaptation, distribution and reproduction in any medium or format, as long as you give appropriate credit to the original author(s) and the source, provide a link to the Creative Commons licence, and indicate if changes were made. The images or other third party material in this article are included in the article's Creative Commons licence, unless

indicated otherwise in a credit line to the material. If material is not included in the article's Creative Commons licence and your intended use is not permitted by statutory regulation or exceeds the permitted use, you will need to obtain permission directly from the copyright holder. To view a copy of this licence, visit http://creativecommons.org/licenses/by/4.0/.

© The Author(s) 2026

[1]Swiss Institute for Experimental Cancer Research (ISREC), School of Life Sciences, Swiss Federal Institute of Technology in Lausanne (EPFL), Lausanne, Switzerland. [2]Agora Cancer Research Center, Lausanne, Switzerland. [3]Biomedical Data Science Facility (BDSF), Swiss Institute of Bioinformatics (SIB), Lausanne, Switzerland. [4]Department of Biotechnology, College of Sciences, University of Tehran, Tehran, Iran. [5]Department of Biotechnology, Institute of Bioprocess Science and Engineering, University of Nature Resources and Life Sciences, Vienna, Austria. [6]Department of Clinical Pharmacy, School of Pharmacy, Shahid Beheshti University of Medical Sciences, Tehran, Iran. [7]Clinical research development center, Imam Hossein Educational hospital, Shahid Beheshti University of Medical Sciences, Tehran, Iran. [8]Department of Allergy and Clinical Immunology, Mofid Children's Hospital, Shahid Beheshti University of Medical Sciences, Tehran, Iran. [9]Department of Allergy and Immunodeficiency, Massoud Medical Laboratory, Tehran, Iran. [10]Ann Romney Center for Neurologic Diseases, Brigham and Women's Hospital, Harvard Medical School, Boston, MA, USA. [11]Laboratory of Tumor Inflammation and Angiogenesis, Center for Cancer Biology, VIB, Leuven, Belgium. [12]Laboratory of Tumor Inflammation and Angiogenesis, Center for Cancer Biology, Department of Oncology, KU Leuven, Leuven, Belgium. [13]Division of Pulmonary Medicine, Department of Medicine, Lausanne University Hospital (CHUV), University of Lausanne (UNIL), Lausanne, Switzerland. [14]Alfred E. Mann Department of Biomedical Engineering, University of Southern California, Los Angeles, CA, USA. [15]Broad Institute of MIT and Harvard, Cambridge, MA, USA. [16]The Gene Lay Institute of Immunology and Inflammation, Brigham and Women's Hospital, Harvard Medical School, Boston, MA, USA. [17]These authors contributed equally: Bruno Torchia, Nadine Fournier.
✉e-mail: nahal.mansouri@chuv.ch

https://doi.org/10.1038/s43018-026-01257-5

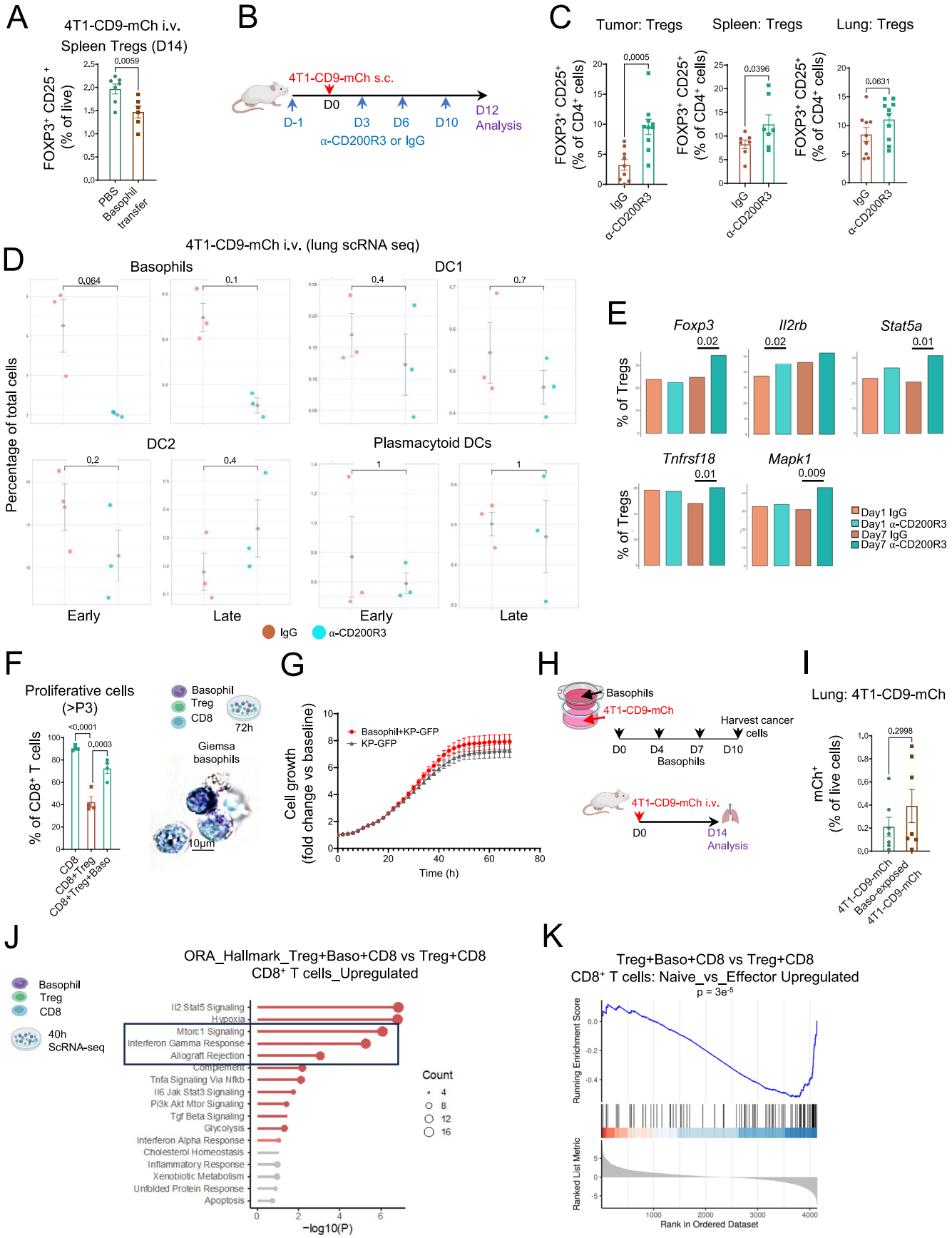


Extended Data Fig. 1 | See next page for caption.

https://doi.org/10.1038/s43018-026-01257-5

Extended Data Fig. 1 | Basophils inhibit metastasis to the lung. **A**. Representative H&E staining of the lung from a mouse bearing a subcutaneous 4T1 mammary tumor. **B**. Percentage of the indicated lung immune cell populations in tumor-free and 4T1 tumor-bearing mice. **C**. Percentage of lung basophils and Tregs in tumor-free and 4T1 tumor-bearing mice. B–C, $n = 3$ (w/o tumor) and 6 (w/ tumor). **D**. Representative flow cytometry plots (left) and quantification (right) of lung basophils ($CD45^+CD117^-Fc\varepsilon RI^+CD49b^+$) one day after anti-CD200R3 or IgG treatment in tumor-free mice. $n = 2$. **E**. Percentage of the indicated lung immune cell populations 14 days after anti-CD200R3 or IgG treatment. $n = 16$. **F**. Representative H&E images of lungs from mice injected intravenously with 4T1-CD9-mCh cells and treated with IgG or anti-CD200R3 (left). Right, quantification of lungs with or without micrometastases. $n = 16$. **G**. Experimental design for early basophil depletion in mice bearing subcutaneous 4T1-CD9-mCh tumors. **H**. Percentage of 4T1-CD9-mCh cells in the lungs following early basophil depletion. $n = 10$ (IgG) and 8 (anti-CD200R3). **I**. Experimental design for late basophil depletion in mice injected with 4T1-CD9-mCh cells i.v. **J**. Percentage of 4T1-CD9-mCh cells in the lungs. $n = 8$. **K**. Experimental design for tracking transferred basophils in transgenic KP mice. **L**. Percentage of donor-derived $CD45.1^+$ basophils among total basophils in the indicated organs over time. BM, bone marrow. $n = 1$ mouse per time point. **M**. Experimental design for basophil transfer in mice injected with 4T1-CD9-mCh cells. **N**. Percentage of 4T1-CD9-mCh cells in the lungs following basophil transfer. $n = 8$. Data are presented as mean ± s.e.m. in bar plots. Statistical analysis: **B** and **C**, two-sided Wilcoxon tests with Benjamini–Hochberg correction; **E**, unpaired two-sided Student's *t*-test; **H** and **N**, unpaired one-sided Student's *t*-tests; **J**, unpaired two-sided Student's *t*-test. In **B** and **C** some data are also shown in Fig. 1c.

https://doi.org/10.1038/s43018-026-01257-5

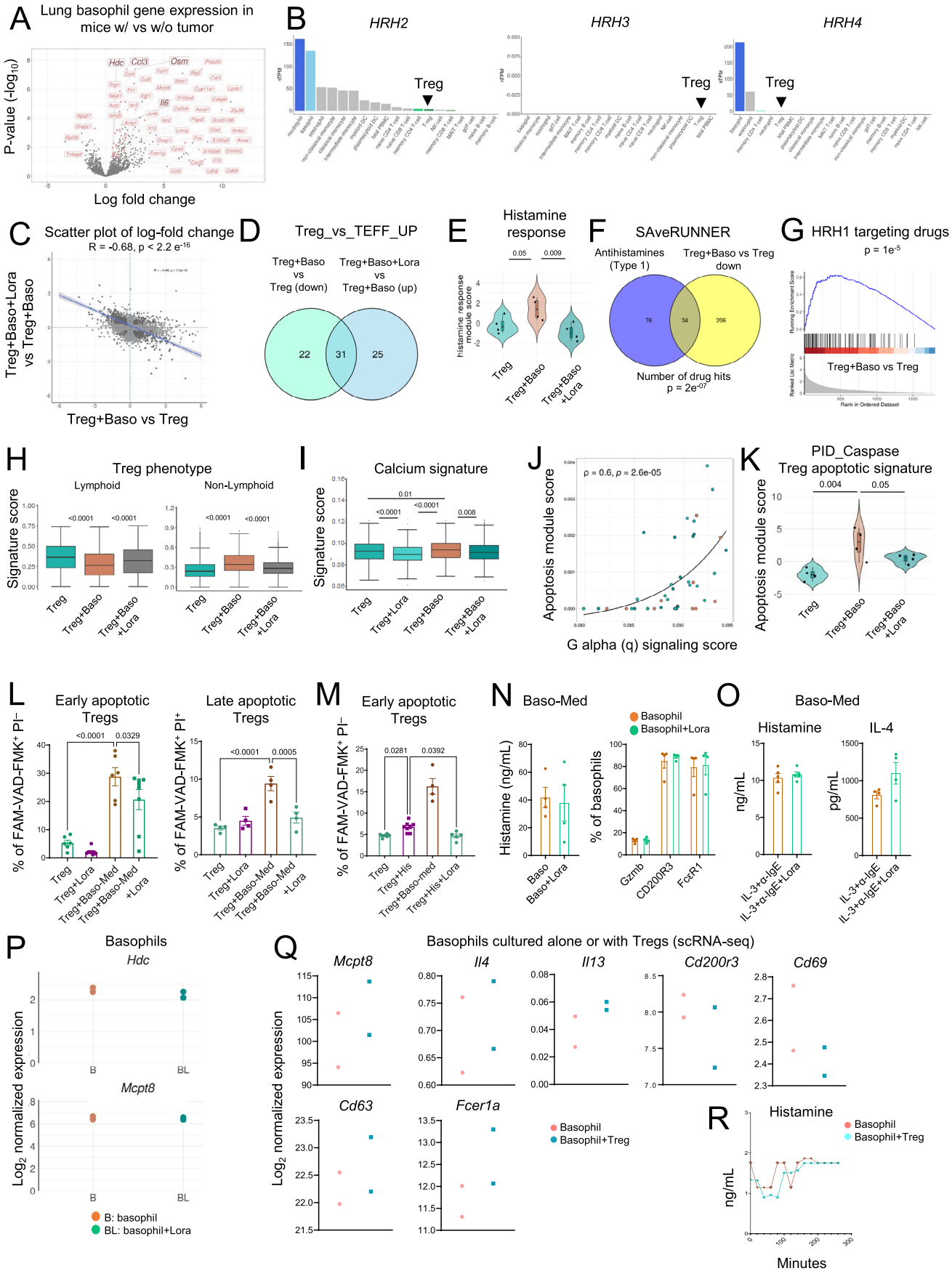


Extended Data Fig. 2 | See next page for caption.

https://doi.org/10.1038/s43018-026-01257-5

Extended Data Fig. 2 | Basophils suppress Tregs in mice. A. Percentage of splenic Tregs following intravenous injection of 4T1-CD9-mCh cells and basophil transfer. $n = 7$ (PBS) and 6 (basophil transfer). **B**. Experimental design for basophil depletion in the subcutaneous 4T1-CD9-mCh model. **C**. Percentage of Tregs in the indicated organs following basophil depletion. $n = 7$ for spleen; $n = 9$ (IgG) and 10 (anti-CD200R3) for tumor and lung. **D**. Percentage of the indicated lung immune cell populations at early and late time points related to Fig. 2e. $n = 3$. **E**. Proportion of Tregs expressing *Foxp3, Il2rb, Stat5a, Mapk1* and *Tnfrsf18* at the indicated time points. $n = 3$ mice per group. **F**. Experimental design (top) and percentage of CellTrace Violet$^+$ CD8$^+$ T cells undergoing >3 rounds of proliferation (bottom). Representative Giemsa staining of ex vivo cultured basophils (right). $n = 4$ independent cell cultures. **G**. Dynamic killing assay of KP-GFP$^+$ cancer cells cultured alone or with basophils. Cancer cell growth is shown as fold change from baseline over time. $n = 5$ (KP-GFP) and 3 (KP-GFP+basophils) independent cell cultures. **H**. Experimental design for transwell co-culture of basophils and 4T1-CD9-mCh cells before i.v. cancer cell injection. **I**. Percentage of 4T1-CD9-mCh cells in the lungs of mice. $n = 7$. **J**. Hallmark pathways enriched in CD8$^+$ T cells from the indicated co-cultures, identified by ORA of the 200 most upregulated genes. Circle size indicates gene number; x axis, $-\log_{10}(P)$. Red, $P < 0.05$; light red, $P < 0.1$; grey, not significant. ~1,000 cells were analysed per condition from $n = 2$ independent cell cultures. **K**. GSEA of naïve versus effector CD8$^+$ T-cell signatures (GSE9650) in CD8$^+$ T cells from Treg+basophil versus Treg-only co-cultures. ~1,000 cells were analysed per condition from $n = 2$ independent cell cultures. Data are presented as mean ± s.e.m in bar plots. Statistical analysis: **A** and **C**, unpaired one-sided Student's *t*-tests; **D** and **E**, two-sided Wilcoxon tests with Benjamini–Hochberg correction; **F**, one-way ANOVA; **I**, unpaired two-sided Student's *t*-test; **J**, one-sided Fisher's exact test; **K**, GSEA with 100,000 random permutations ($P = 3 \times 10^{-5}$). Panels **f** and **h** created in BioRender; De Palma Lab EPFL https://biorender.com/8yxozuz (2026).

https://doi.org/10.1038/s43018-026-01257-5

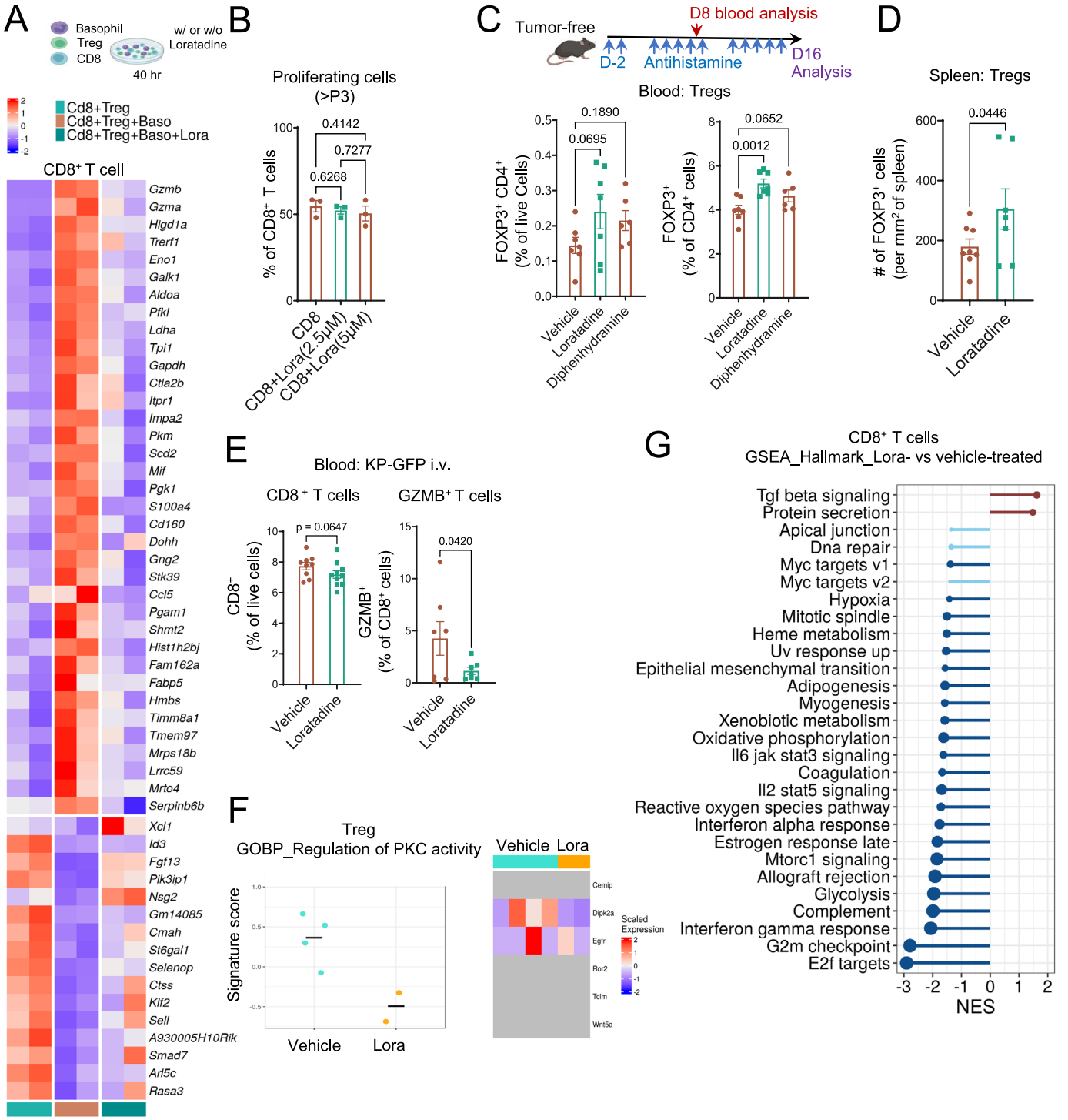


Extended Data Fig. 3 | See next page for caption.

https://doi.org/10.1038/s43018-026-01257-5

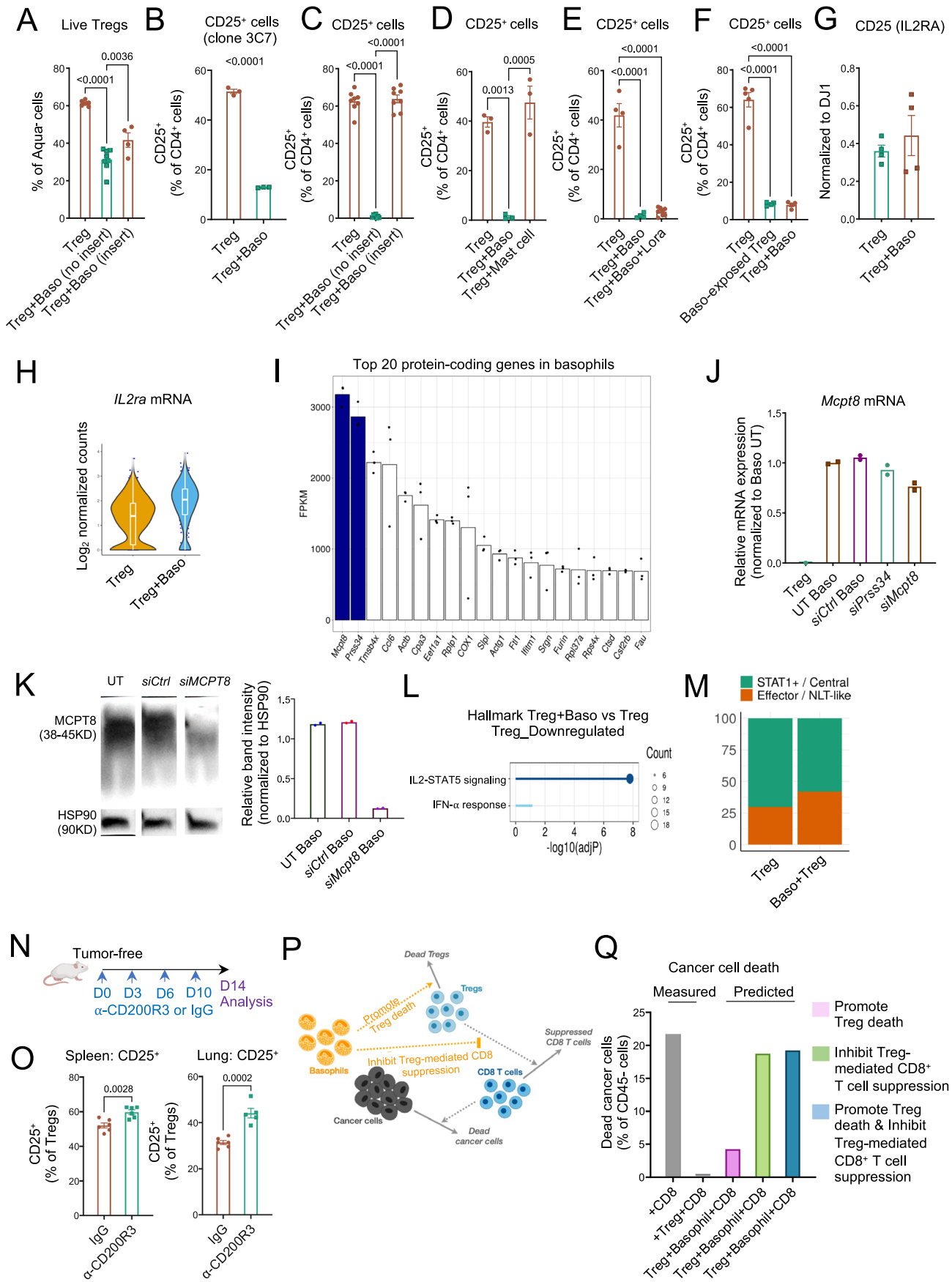
Extended Data Fig. 3 | Basophil-secreted histamine inhibits Tregs. A. Volcano plot of differentially expressed genes in tumor-free and tumor-bearing basophils. Red, adjusted P < 0.005 and fold change >1.5 or <−1.5. *n* = 3 (tumor-free) and 6 (tumor-bearing). **B**. *HRH2, HRH3* and *HRH4* expression across immune-cell populations from the Human Protein Atlas. **C**. Correlation of log fold changes induced by basophils and loratadine. *n* = *2*. **D**. Venn diagram of leading-edge genes shared between the two GSEA comparisons. *n* = 2. **E**. Positive histamine-response pathway scores in Tregs cultured with basophils ± loratadine. *n* = 4. **F**. Overlap between HRH1-targeting drugs and drugs predicted by SAveRUNNER to reverse basophil-repressed Treg genes. **G**. GSEA showing enrichment of type 1 antihistamines among DrugBank drugs ranked by normalized enrichment rank. *n* = 2. **H**. Treg phenotype signature scores from ref. 33. ~1,000 Tregs per condition from *n* = 2. **I**. Calcium-signalling pathway expression (KEGG). ~1,000 Tregs were profiled per condition from *n* = 2. **J**. Correlation between Gαq-signalling activity and apoptosis score. *n* = 18 (Treg) and 12 (Treg+Baso and Treg+Baso+Lora). **K**. Caspase pathway scores in Tregs. *n* = 4. **L**. Early apoptotic Tregs after 24 h cultured with basophil-conditioned medium (Baso-Med) ± loratadine (left). *n* = 6 per condition without loratadine and 8 per condition with loratadine. Late apoptotic Tregs after 36 h (right). *n* = 4 per condition. **M**. Early apoptotic Tregs cultured with histamine (His), basophil-conditioned medium (Baso-Med) or histamine plus loratadine. *n* = 7, 8, 4 and 5 respectively. **N**. Histamine secretion and granzyme B, CD200R3 and FcεRI expression in basophils following vehicle or loratadine treatment. *n* = 4 independent cell cultures. **O**. Histamine and IL-4 concentrations in baso-med. *n* = 5 (histamine) and 4 (IL-4). **P**. Log_2-normalized *Hdc* and *Mcpt8* expression. ~4,500 basophils per condition from *n* = 2. **Q**. Log_2-normalized expression of the indicated genes. ~4,500 basophils per condition from *n* = 2. **R**. Histamine secretion over time by basophils cultured alone or with Tregs, sampled every 20 min from one co-culture per group. In **L**–**O**, data are presented as mean ± s.e.m. In **H** and **I**, box plots show median, IQR and whiskers extending to 1.5 × IQR. Statistical analysis: **A**, moderated *t*-statistics with Benjamini–Hochberg correction; **C**, Pearson correlation; **E** and **K**, two-sided Student's *t*-tests with Benjamini–Hochberg correction; **F**, Fisher's exact test; **G**, GSEA with 100,000 permutations; **H** and **I**, Wilcoxon tests with Benjamini–Hochberg correction; **J**, Spearman correlation with three-parameter power regression; **L** and **M**, one-way ANOVA with Fisher's LSD test; **N** and **O**, unpaired two-sided Student's *t*-tests. In panels **D**, **E** and **G**–**Q**, each *n* represents one independent cell culture.

https://doi.org/10.1038/s43018-026-01257-5



Extended Data Fig. 4 | Inhibition of histamine signaling impairs CD8⁺ T cells and enhances lung metastatic seeding in mice. A. Top, schematic of the scRNA-seq co-culture assay. Bottom, heatmap of differentially expressed genes in CD8⁺ T cells, showing genes induced by basophils and reversed by loratadine (upper) and genes repressed by basophils and restored by loratadine (lower). $n = 2$. Cut-offs: log fold change > 1.5 or < −1.5 and $P < 0.05$. **B**. CD8⁺ T cells undergoing >3 rounds of proliferation after 72 h. $n = 3$. **C**. Top, schematic of the experimental design. Bottom, FOXP3⁺ Tregs among live cells and CD4⁺ T cells in blood on day 8. $n = 7$ (vehicle and loratadine) and 6 (diphenhydramine). **D**. Splenic Tregs in mice injected i.v. with 4T1 cells and treated with vehicle or loratadine, quantified by immunohistochemistry as FOXP3⁺ cells/mm². $n = 8$ (vehicle) and 7 (loratadine). **E**. Blood CD8⁺ T cells and GZMB⁺ CD8⁺ T cells in mice injected i.v. with KP-GFP cells. $n = 9$ and 10 (CD8⁺ T cells); $n = 7$ (GZMB⁺ CD8⁺ T cells). **F**. Enrichment of the Gene Ontology Biological Process term "regulation of PKC activity" in Tregs from vehicle- and loratadine-treated mice. Left, graph; right, heatmap. $n = 4$ (vehicle) and 2 (loratadine). **G**. Hallmark GSEA of splenic CD8⁺ T cells from loratadine- versus vehicle-treated mice. Circle size indicates significance; x axis, normalized enrichment score (NES). $n = 4$ mice. Data are presented as mean ± s.e.m. in bar plots unless otherwise indicated. Statistical analysis: **B** and **C**, one-way ANOVA; **D** and **E**, unpaired one-sided Student's *t*-tests; **G**, GSEA with 100,000 permutations and Benjamini–Hochberg correction. In panels **A** and **B**, *n* represents independent cell cultures. Panel **a** created in BioRender; De Palma Lab EPFL https://biorender.com/8yxozuz (2026).

https://doi.org/10.1038/s43018-026-01257-5

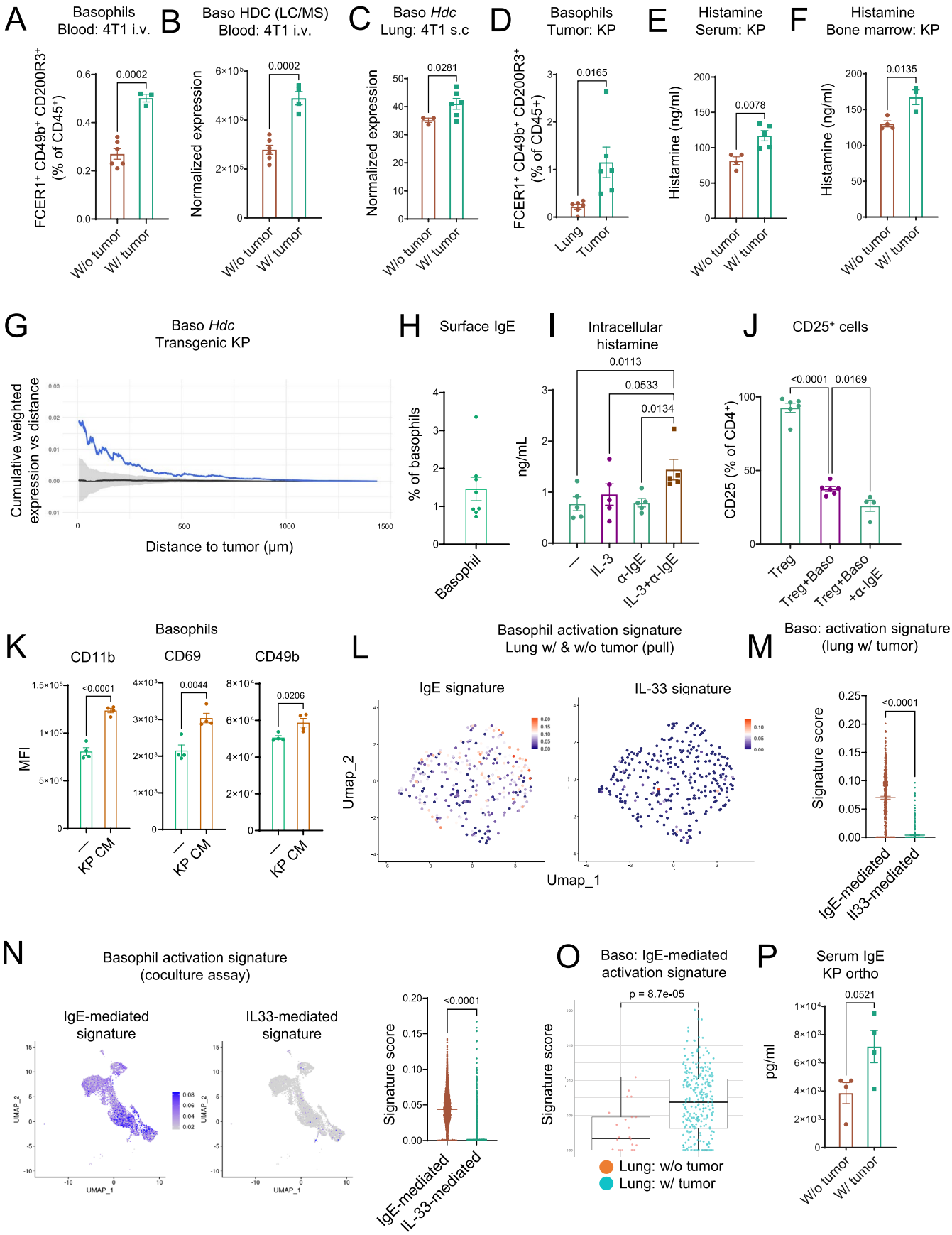


Extended Data Fig. 5 | See next page for caption.

https://doi.org/10.1038/s43018-026-01257-5

Extended Data Fig. 5 | Basophils inhibit Tregs through mast cell protease 8 (MCPT8)-mediated IL-2Rα (CD25) cleavage. A. Viability of Tregs cultured alone or with basophils in the presence of a 0.4 µm transwell insert. Data represent $Aqua^{-}CD4^{+}$ T cells. *n* = 8 (Treg), 8 (Treg+Baso) and 4 (Treg+Baso+insert). **B**. $CD25^{+}$ cells among $CD4^{+}$ T cells using anti-CD25 clone 3C7. *n* = 3. **C**. $CD25^{+}$ cells among $CD4^{+}$ T cells in the indicated culture conditions using a transwell insert. *n* = 8. **D**. $CD25^{+}$ cells among $CD4^{+}$ T cells in the indicated co-cultures. *n* = 3. **E**. $CD25^{+}$ cells among $CD4^{+}$ T cells in the indicated co-cultures. *n* = 4 (Treg), 4 (Treg+Baso) and 8 (Treg+Baso+Lora). **F**. $CD25^{+}$ cells among $CD4^{+}$ T cells following 4 h of basophil exposure, Treg sorting and an additional 72 h of culture (related to Fig. 2i). *n* = 5 (Treg), 4 (basophil-exposed Treg) and 4 (Treg+Baso). **G**. CD25 protein quantification in Tregs cultured alone or with basophils (related to Fig. 5b). *n* = 4. **H**. *Il2ra* (CD25) expression in Tregs cultured alone or with basophils by scRNA-seq. *n* = 2. **I**. Top 20 protein-coding genes in basophils measured by bulk RNA-seq. Serine proteases are highlighted in blue. *n* = 3. **J**. *Mcpt8* expression in basophils 72 h after siRNA knockdown, measured by qPCR and normalized to *Gapdh*. *n* = 1 (untransfected, UT) and 2 (all other conditions). **K**. MCPT8 immunoblot in UT, siCtrl- and siMCPT8-transfected basophils (left). HSP90 served as loading control. Band quantification (right). *n* = 2. **L**. Over-representation analysis of Hallmark pathways using the top 200 genes repressed in basophil-exposed Tregs. Circle size indicates gene number; x axis shows $-\log_{10}$ adjusted *P*. *n* = 2. **M**. Proportion of Tregs classified as $STAT1^{+}$ central or effector/non-lymphoid tissue (NLT) subsets. *n* = 2. **N**. Schematic of basophil depletion in tumor-free mice. **O**. $CD25^{+}$ cells among splenic and lung $CD4^{+}FOXP3^{+}$ Tregs. Spleen *n* = 6 per group; lung *n* = 6 (IgG) and 5 (anti-CD200R3). **P**. Mathematical model of interactions between cancer cells, Tregs, $CD8^{+}$ T cells and basophils. **Q**. Model predictions of mechanisms contributing to cancer cell death in co-culture assays. In **J** and **O**, data are presented as mean ± s.e.m. In **H**, violin plots contain box plots showing the median and IQR, with whiskers as indicated. Related to Fig. 2i for **F** and Fig. 3d for **H**, **L** and **M**. Statistical analysis: **A** and **C**–**F**, one-way ANOVA with Fisher's LSD test; **B**, **G**, **H** and **O**, two-sided Student's *t*-tests; **L**, one-sided Fisher's exact test with Benjamini–Hochberg correction. In **A**–**M**, *n* represents independent cell cultures. **A**–**E**, 24-h co-culture; in **F**, Tregs were exposed to basophils for 4 h, sorted and cultured for an additional 72 h before analysis.

https://doi.org/10.1038/s43018-026-01257-5

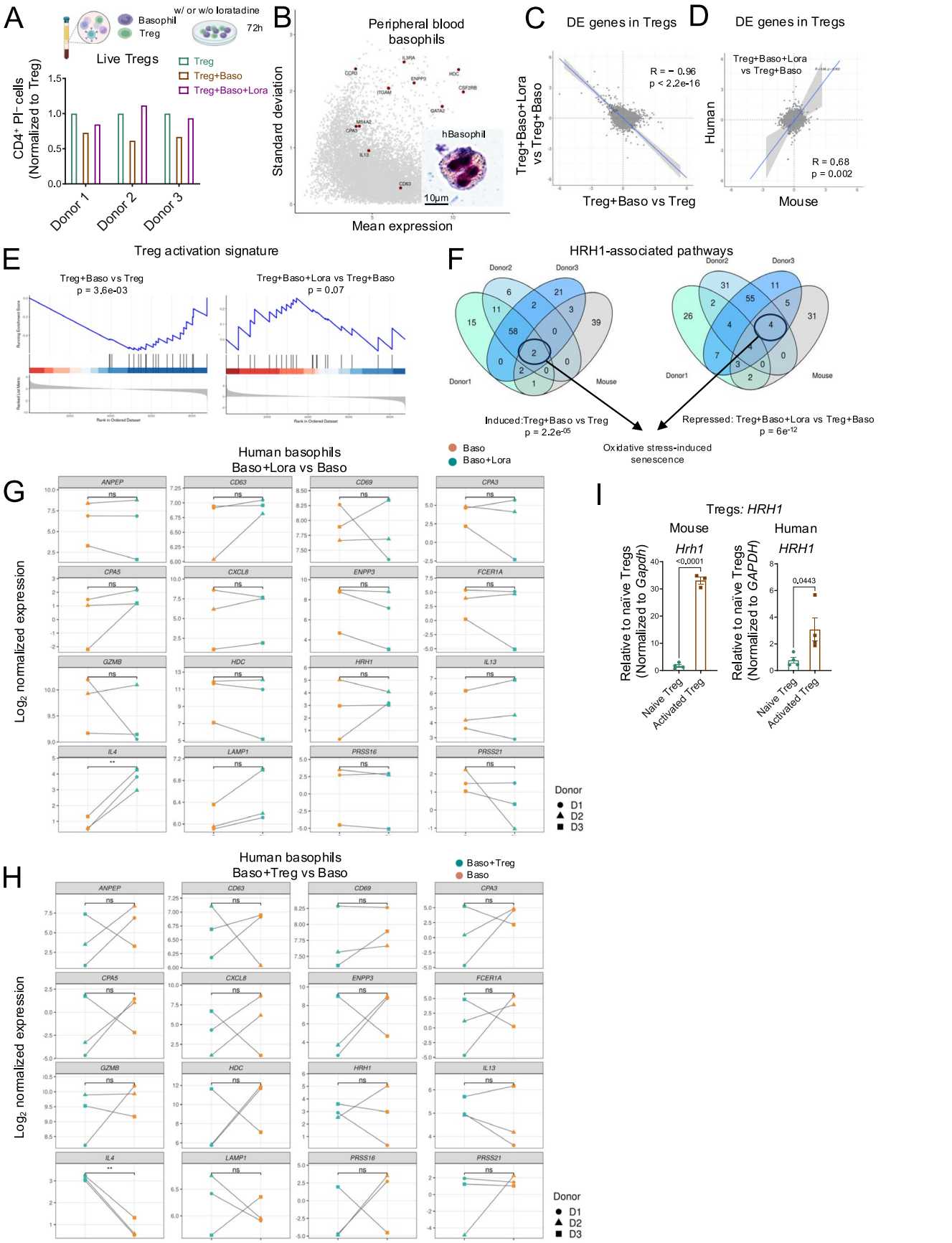


Extended Data Fig. 6 | See next page for caption.

https://doi.org/10.1038/s43018-026-01257-5

Extended Data Fig. 6 | Histamine levels are locally and systemically elevated in cancer. A. Blood basophils (FcεRI$^+$CD49b$^+$CD200R3$^+$CD45$^+$) in healthy or i.v. 4T1 tumor-bearing mice. *n* = 6 (no tumor) and 3 (tumor). **B**. HDC protein expression in blood basophils measured by LC–MS. *n* = 6 (no tumor) and 4 (tumor). **C**. *Hdc* expression in lung basophils from mice with or without s.c. 4T1 tumors. *n* = *3* (w/o tumor) and *6* (w/ tumor). **D**. Basophils (FcεRI$^+$CD49b$^+$CD200R3$^+$CD45$^+$) in orthotopic KP tumors or healthy lungs. *n* = 6. **E**. Serum histamine in mice with or without orthotopic KP tumors. *n* = 4 (no tumor) and 5 (tumor). **F**. Histamine in conditioned medium from bone marrow cells cultured for 24 h. *n* = 4 (no tumor) and 3 (tumor). **G**. Spatial distribution of cumulative *Hdc* expression in a representative field of view from one KP mouse lung; >10 fields of view were analysed. **H**. Anti-IgE$^+$ basophils after 7 days of culture. *n* = 8. **I**. Intracellular histamine after 16 h stimulation. *n* = 5. **J**. CD25$^+$CD4$^+$FOXP3$^+$ Tregs after 16 h anti-IgE stimulation. *n* = 6 (Treg and Treg+Baso) and 4 (Treg+Baso+α-IgE). **K**. Mean fluorescence intensity of the indicated marker in basophils cultured with KP-conditioned medium (CM). *n* = 4. **L**. UMAP of IgE- and IL-33-mediated activation signatures in lung basophils. *n* = 3 (w/o tumor) and 6 (tumor). **M**. IgE- and IL-33-mediated activation signature scores in lung basophils from s.c. 4T1 tumor-bearing mice. *n* = 6 mice. **N**. UMAP of IgE- and IL-33-mediated activation signatures in ex vivo-cultured basophils pooled from *n* = 22 independent cell cultures. Right, quantification of IgE- versus IL-33-signature scores. **O**. IgE-mediated activation signature scores in lung basophils from tumor-free (*n* = 3) and s.c. 4T1 tumor-bearing (*n* = 6) mice; tumor-bearing data are also shown in M. **P**. Serum IgE concentration in mice with or without orthotopic KP tumors. *n* = 4 mice/group. In **A**–**F**, **H**–**J**, **K**, **M**, **N** and **P**, data are represented as mean ± s.e.m. In **O**, box plot shows the median, IQR and whiskers as indicated. Statistical analysis: **A**, **B**, **D**–**F**, **K** and **P**, unpaired two-sided Student's *t*-tests; **C**, unpaired two-sided Welch's *t*-test; **I** and **J**, one-way ANOVA with Fisher's LSD test; **M** and **N**, paired two-sided Student's *t*-tests performed at single cell level; **O**, Wilcoxon rank-sum test with continuity correction. In **H**–**K**, *n* represents independent cell cultures. **M**–**O**, each dot represents one basophil. Panels **C**, **L**, **M** and **O** are derived from the dataset shown in Fig. 1a. IgE and IL-33 signatures in **L**–**O** were derived from ref. 38.

https://doi.org/10.1038/s43018-026-01257-5

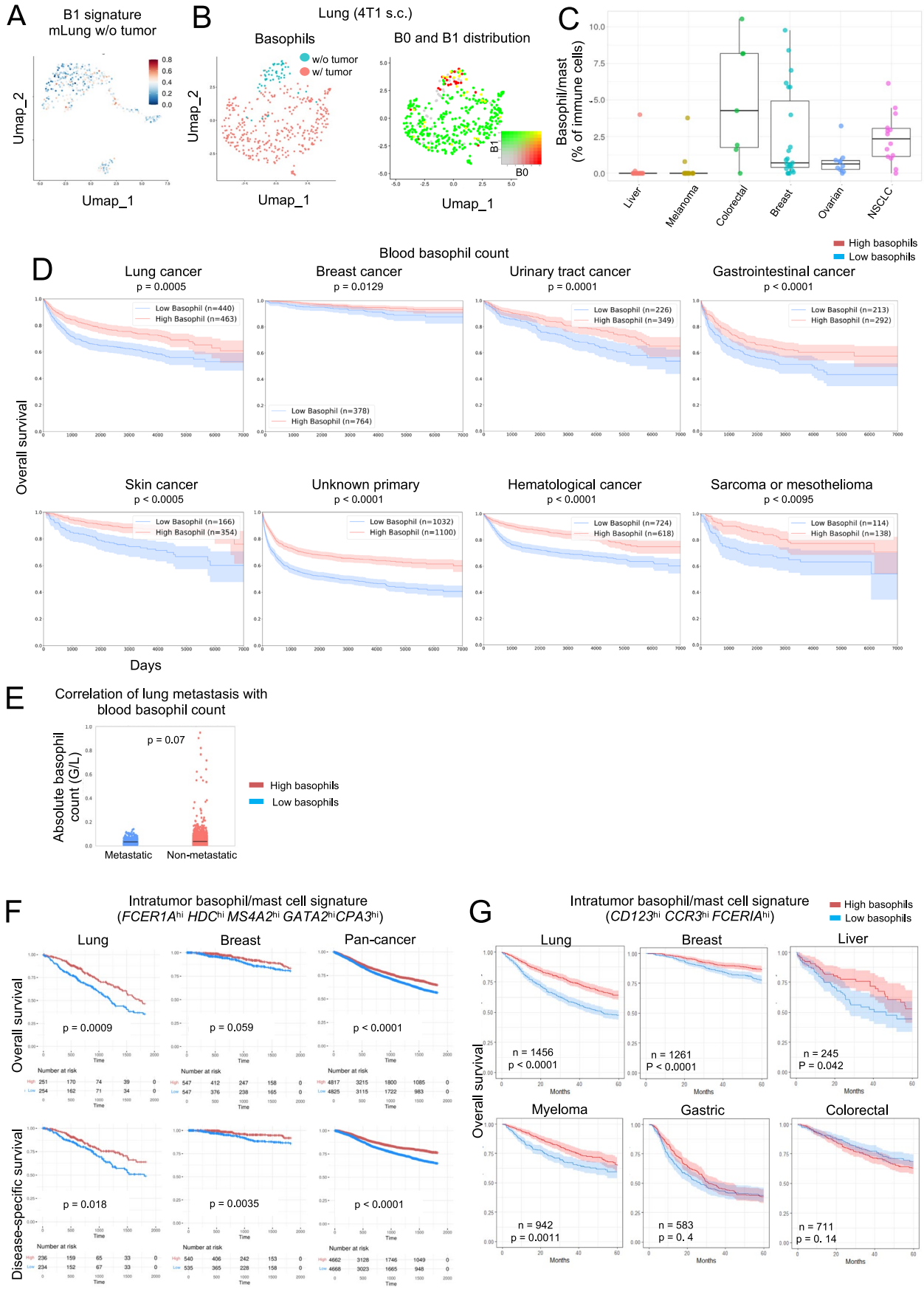


Extended Data Fig. 7 | See next page for caption.

https://doi.org/10.1038/s43018-026-01257-5

Extended Data Fig. 7 | HRH1-mediated basophil-Treg crosstalk is conserved in humans. A. Top, schematic of the human basophil–Treg co-culture assay. Bottom, live Tregs ($CD4^+PI^-$) after co-culture with basophils ± loratadine (5 µM), normalized to Tregs. $n = 3$ donors. **B**. Mean expression versus standard deviation of genes in human blood basophils analysed by bulk RNA-seq. Basophil-associated genes are highlighted in red. Bottom right, Giemsa-stained human basophils. $n = 3$. **C**. Correlation of log_2 fold changes induced by human basophils and loratadine in Tregs. $n = 3$. **D**. Correlation of loratadine-induced log_2 fold changes in Tregs exposed to basophils in human ($n = 3$) and mouse ($n = 2$ independent cell cultures). **E**. GSEA of a custom Treg activation signature in the indicated comparisons. *P* values were computed using 100,000 permutations. $n = 3$. **F**. Venn diagrams of Reactome pathways enriched in basophil-induced genes (left) and loratadine-repressed genes (right) in human and mouse Tregs. ORA was performed on the top 100 differentially expressed genes. $n = 3$. **G**. Log_2-normalized expression of the indicated genes in human basophils treated with vehicle or loratadine. $n = 3$. **H**. Log_2-normalized expression of the indicated genes in human basophils cultured alone or with Tregs. $n = 3$. **I**. *HRH1* expression in mouse (left) and human (right) Tregs before and after 24 h activation with anti-CD3/CD28 Dynabeads, normalized to *GAPDH* and expressed relative to naïve Tregs. Mouse: $n = 4$ (naïve) and 3 (activated); human: $n = 4$ per group. Data are presented as mean ± s.e.m. in bar plots. Statistical analysis: **C** and **D**, Pearson correlation; **E**, GSEA with 100,000 permutations; **G** and **H**, paired two-sided Student's *t*-tests; **I**, unpaired two-sided Student's *t*-tests. In panels **A** and **G**–**I**, *n* represents independent donors unless stated otherwise. Panel **a** created in BioRender; De Palma Lab EPFL, https://biorender.com/8yxozuz (2026); De Palma Lab EPFL, https://biorender.com/m9grmnj (2026).

https://doi.org/10.1038/s43018-026-01257-5

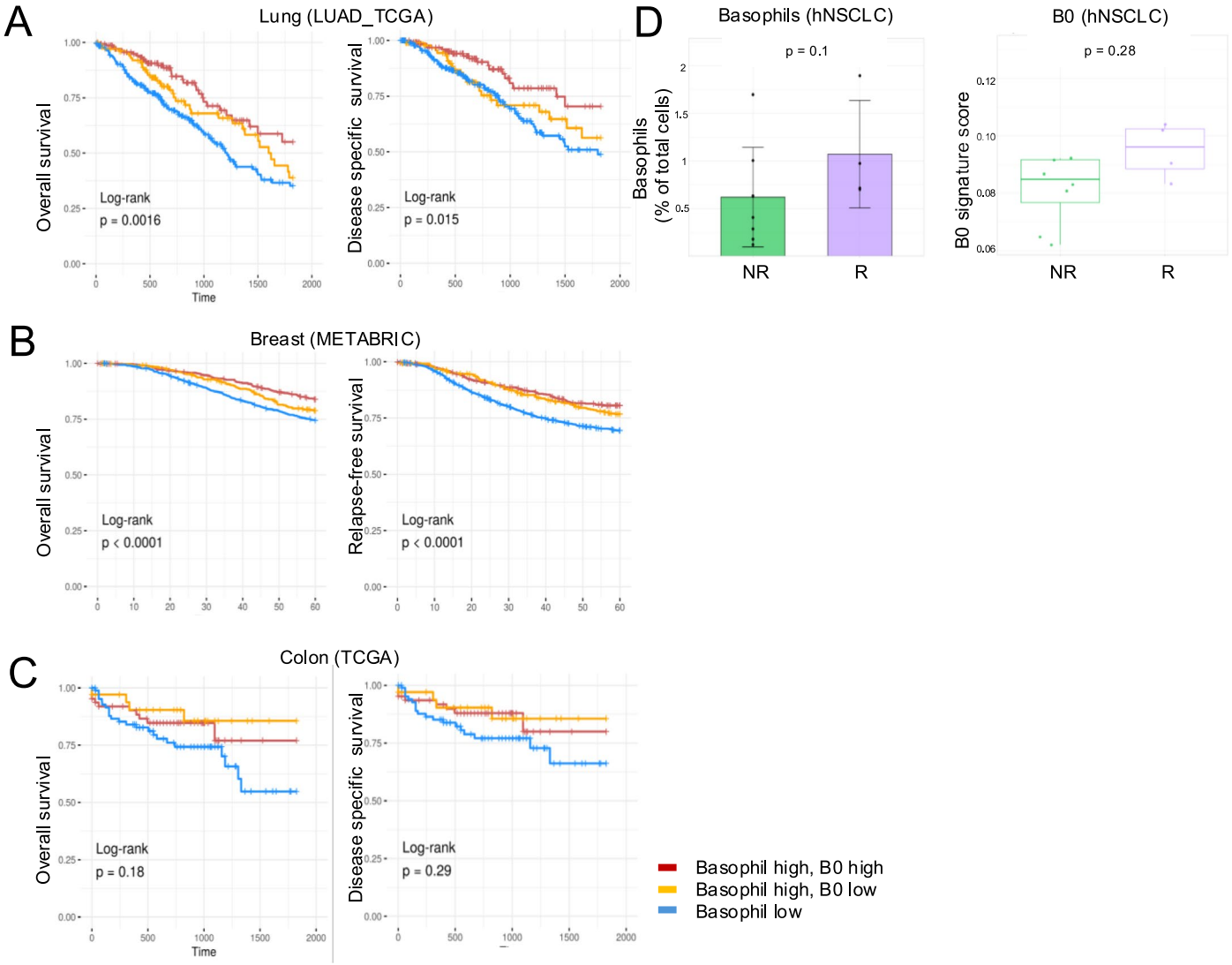


Extended Data Fig. 8 | See next page for caption.

https://doi.org/10.1038/s43018-026-01257-5

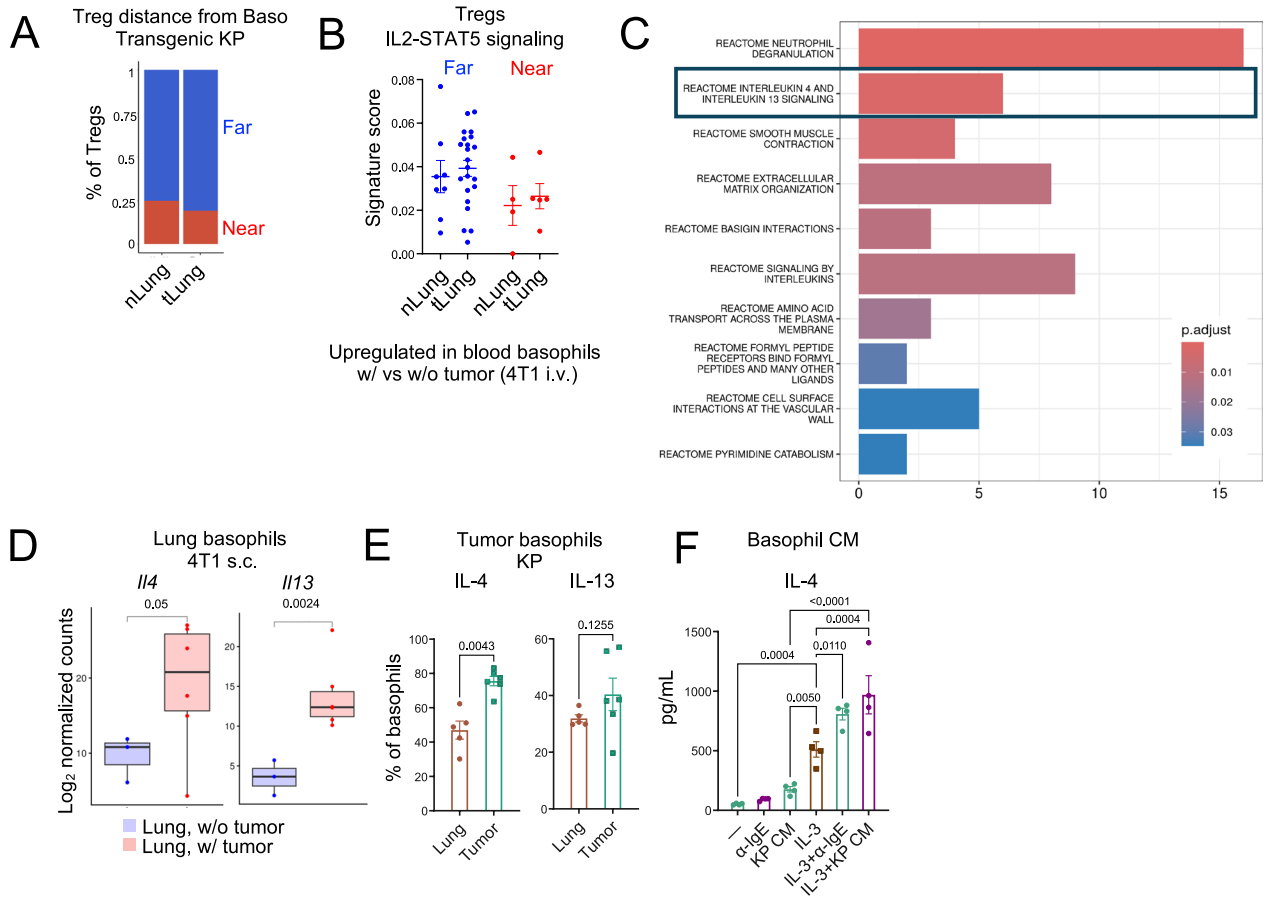
Extended Data Fig. 8 | Circulating and intratumoral basophils are associated with improved survival in patients with cancer. A. UMAP of the B1 signature in basophils from tumor-free mice. *n* = 4. **B**. Left, UMAP of lung basophils from tumor-free (*n* = 6) and tumor-bearing (*n* = 8) mice. Right, UMAP of B0 and B1 signature enrichment. **C**. Human basophil/mast cell abundance among immune cells across cancer types. *n* = 16 (Liver); *n* = 20 (melanoma); *n* = 7 (colorectal); *n* = 23 (breast); *n* = 10 (ovarian); *n* = 14 (lung). **D**. Overall survival in patients with low or high blood basophil counts in indicated cancers. Groups sizes are shown in the panels. **E**. Association between lung metastasis and blood basophil counts in metastatic and non-metastatic cancers (cut-off, 0.03 G/L). *n* = 5,071 (low) and 6,093 (high) patients. **F**. Intratumoral basophil/mast cell signature *(FCER1A, HDC, MS4A2, GATA2* and *CPA3)* and overall or disease-specific survival in TCGA LUAD, BRCA and pan-cancer cohorts. Patients were stratified by the median signature score. **G**. Intratumoral basophil signature (*CD123, CCR3* and *FCER1A*) and survival across cancer types from the KM-Plotter dataset. Patients were stratified by tertiles of basophil signature expression, with survival compared between the lowest (T1) and highest (T3) tertiles. n = 485 low and 486 high (lung), 420 low and 420 high (breast), 81 low and 82 high (liver), 314 low and 314 high (myeloma), 193 low and 194 high (gastric), and 237 low and 237 high (colorectal). Box plots show the median, IQR and whiskers extending to the most extreme values within 1.5 × IQR. Statistical analysis: **D**, log-rank test; **E**, one-sided Fisher's exact test; **F** and **G**, two-sided log-rank test. **D**–**E**. Analyses of the same clinical cohort used in Fig. 8g.

https://doi.org/10.1038/s43018-026-01257-5



Extended Data Fig. 9 | The B0 program is associated with improved survival in patients with cancer. A. Overall (left) and disease-specific (right) survival in the TCGA lung adenocarcinoma (LUAD) cohort according to intratumoral B0 signature expression. Patients were stratified into Basophil High B0 High (n = 146 and 138), Basophil High B0 Low (n = 105 and 98), and Basophil Low (n = 254 and 234) groups for overall and disease-specific survival, respectively. **B**. Overall (left) and relapse-free (right) survival in the METABRIC breast cancer cohort according to intratumoral B0 signature expression. Patients were stratified into Basophil High B0 High (n = 552), Basophil High B0 Low (n = 438), and Basophil Low (n = 990 and 989) groups for overall and relapse-free survival, respectively. **C**. Overall (left) and disease-specific (right) survival in the TCGA colon cancer cohort according to intratumoral B0 signature expression. Patients were stratified into Basophil High B0 High (n = 63), Basophil High B0 Low (n = 34), and Basophil Low (n = 95) groups. **D**. Intratumoral basophil abundance (% of all cells) in lung cancer patients treated with neoadjuvant immunotherapy, analysed from ref. 49 (left). B0 signature enrichment in the indicated groups (right). n = 4 responders and 7 non-responders. Data are presented as mean ± s.e.m. (bar plots) or as median, IQR and whiskers extending to the most extreme values within 1.5 × IQR (box plots). Statistical analysis: **A**–**C**, log-rank tests; **D**, two-sided Wilcoxon tests.

https://doi.org/10.1038/s43018-026-01257-5



Extended Data Fig. 10 | Tumors alter basophil cytokine profiles without abolishing Treg inhibition. A. Percentage of Tregs located either near (≤50 µm) or far (>50 µm) from basophils in healthy lung (nLung) or tumor/peritumoral lung (tLung), assessed by spatial transcriptomic analysis of KP lung sections. **B**. IL-2–STAT5 signalling signature scores in Tregs located near or far from basophils, Far: $n = 8$ Tregs (nLung) and 22 (tLung); Near: $n = 4$ Tregs (nLung) and 5 (tLung). A–B, cells were analysed across >10 fields of view from $n = 1$ KP mouse lung. These data are a stratified representation of the dataset shown in Fig. 5h. **C**. Reactome pathways enriched among proteins upregulated in blood basophils from breast cancer-bearing mice ($n = 4$) compared with the B0 signature from tumor-free mice ($n = 6$), identified by LC–MS. Colour scale indicates false discovery rate (FDR)-adjusted *P* values. **D**. Log_2-normalized counts of *Il4* and *Il13* in lung basophils from mice with or without breast cancer. Related to Fig. 1a. $n = 3$ (without tumor) and 6 (with tumor). **E**. Percentage of IL-4$^+$ and IL-13$^+$ intratumoral basophils in the orthotopic KP model compared with healthy lung basophils. $n = 5$ (lung) and 6 (tumor). **F**. IL-4 concentration in culture supernatants of basophils stimulated with KP cell line-conditioned medium (CM) or the indicated stimuli for 16 h. $n = 4$ independent cell cultures. The IL-3 + anti-IgE data are also shown in Extended Data Fig. 3O. Data are presented as mean ± s.e.m. in bar plots and dot plots (**B**, **E** and **F**) or as median, IQR and whiskers extending to the most extreme values within 1.5 × IQR in box plots (**D**). Statistical analysis: **C**, Reactome over-representation analysis with Benjamini–Hochberg correction for multiple comparisons; **D**, unpaired two-sided Student's *t*-test; **E**, two-sided Mann–Whitney test; **F**, one-way ANOVA with Fisher's LSD test.

nature portfolio

Corresponding author(s): Nahal Mansouri

Last updated by author(s): 17.09.2026

Reporting Summary

Nature Portfolio wishes to improve the reproducibility of the work that we publish. This form provides structure for consistency and transparency in reporting. For further information on Nature Portfolio policies, see our Editorial Policies and the Editorial Policy Checklist.

Statistics

For all statistical analyses, confirm that the following items are present in the figure legend, table legend, main text, or Methods section.

n/a	Confirmed	
☐	☒	The exact sample size (*n*) for each experimental group/condition, given as a discrete number and unit of measurement
☐	☒	A statement on whether measurements were taken from distinct samples or whether the same sample was measured repeatedly
☐	☒	The statistical test(s) used AND whether they are one- or two-sided *Only common tests should be described solely by name; describe more complex techniques in the Methods section.*
☐	☒	A description of all covariates tested
☐	☒	A description of any assumptions or corrections, such as tests of normality and adjustment for multiple comparisons
☐	☒	A full description of the statistical parameters including central tendency (e.g. means) or other basic estimates (e.g. regression coefficient) AND variation (e.g. standard deviation) or associated estimates of uncertainty (e.g. confidence intervals)
☐	☒	For null hypothesis testing, the test statistic (e.g. *F*, *t*, *r*) with confidence intervals, effect sizes, degrees of freedom and *P* value noted *Give P values as exact values whenever suitable.*
☒	☐	For Bayesian analysis, information on the choice of priors and Markov chain Monte Carlo settings
☒	☐	For hierarchical and complex designs, identification of the appropriate level for tests and full reporting of outcomes
☒	☐	Estimates of effect sizes (e.g. Cohen's *d*, Pearson's *r*), indicating how they were calculated

Our web collection on statistics for biologists contains articles on many of the points above.

Software and code

Policy information about availability of computer code

Data collection

Flow-cytometry data were acquired using BD LSRFortessa, BD LSR II SORP, Beckman Coulter CytoFLEX S and CytoFLEX LX, and Invitrogen Attune NxT flow cytometers.

Immunofluorescence and microscopy images were acquired using a Zeiss LSM700 confocal microscope or an Axioscan 7 slide scanner (Zeiss).

Mouse bulk RNA-sequencing and single-cell RNA-sequencing libraries were sequenced using an Illumina NovaSeq 6000. Human bulk RNA-sequencing libraries were sequenced using an Element Biosciences AVITI.

Spatial-transcriptomics libraries were sequenced using both platforms.Micro-CT scans of mouse lungs were acquired using a Quantum FX micro-CT scanner (PerkinElmer).Absorbance-based assays were measured using an Infinite microplate reader (Tecan).

Dynamic cancer-cell growth was monitored using an IncuCyte live-cell imaging system (Sartorius).

Peptide fractions were analysed by nanoLC–MS/MS using a Vanquish Neo UHPLC coupled to an Orbitrap Ascend Tribrid mass spectrometer (Thermo Fisher Scientific).

Data analysis

Graphs were generated using Prism (GraphPad Software) or R. Data are presented as mean ± s.e.m. unless otherwise indicated. Individual data points are shown whenever possible. Normality was assessed using the Shapiro–Wilk test. Equality of variances was not formally tested. Comparisons were performed using Student's or Welch's t-tests, Mann–Whitney or Wilcoxon tests, analysis of variance, Fisher's exact tests, log-rank tests or permutation-based analyses, as specified in the figure legends. Initial exploratory analyses used two-sided tests. One-sided tests were used for subsequent experiments addressing prespecified directional hypotheses; otherwise, two-sided tests were applied. Multiple comparisons were performed using one-way ANOVA followed by Fisher's LSD test, multiple paired t-tests or Benjamini–Hochberg correction, as indicated. Exact P values are shown in the figures, except when $P < 0.0001$.

or the prospective randomized crossover clinical trial, treatment comparisons were performed using paired statistical methods. Because the data were not normally distributed, placebo and loratadine measurements were compared using the Wilcoxon signed-rank test. Data are presented as mean ± s.d. unless otherwise indicated. Schematics were created with BioRender.com under a publication licence.

Schematics included in this study were created with BioRender.com under a publication license. Further information on research design is available in the Nature Portfolio Reporting Summary linked to this article.

Flow-cytometry data were analysed using FlowJo v10.1 (FlowJo LLC). Gating strategies are reported in Supplementary Figs. 1–9 and Supplementary Table 3.

Immunofluorescence images were analysed using QuPath. A region of interest (ROI) encompassing the lung was defined by setting a DAPI threshold and manually adjusted to include DAPI-negative areas and exclude adjacent tissue. For quantification of GFP^+ and mCh^+ areas, a GFP^+ or mCh^+ pixel classifier trained on 10% of the dataset was applied. The area positive for each marker was normalized to the total lung area. Nuclei were segmented using StarDist with the "dsb2018_heavy_augment.pb" model applied to the DAPI channel.

scRNA-seq data were processed using Cell Ranger v7.0.0 against the mouse mm10 reference genome. Downstream analyses were performed using Seurat v5.3.0, and pathway-enrichment analyses were performed using clusterProfiler v4.6.2.

Micro-CT scans to measure lung metastasis (Fig. 1H): Tumour volumes were quantified from micro-CT scans using Analyze software, and three-dimensional reconstructions were generated using OsiriX MD (Pixmeo). Tumours were identified as spherical solid masses with ground-glass opacity. Pixel-intensity thresholds were manually adjusted based on the contrast between tumour and surrounding lung tissue, allowing automated delineation of tumour margins, with manual correction when necessary. Individual tumours were defined as separate objects, and their volumes were calculated using the software.

Mass spectrometry

Raw mass-spectrometry data were processed using Proteome Discoverer v3.0 with SEQUEST and MSFragger and searched against the UniProt Mus musculus reference proteome (release 2025_03), supplemented with common contaminant proteins. Searches were performed with trypsin specificity, allowing up to two missed cleavages. Carbamidomethylation of cysteine and TMTpro modification of lysine residues and peptide N termini were specified as fixed modifications; methionine oxidation was specified as a variable modification. A false-discovery rate of 1% was applied at both the peptide and protein levels. Protein quantification and statistical analyses were performed in R v4.4.2 using in-house scripts. TMT reporter-ion intensities were normalized for sample loading and subsequently subjected to trimmed mean of M-values normalization using edgeR v4.4.2. Differential protein abundance was assessed using limma v3.62.2, with P values adjusted using the Benjamini–Hochberg method. Proteins with an adjusted $P < 0.05$ were considered significantly differentially abundant.

RNA sequencing and bioinformatics analysis

Mouse RNA-seq. Total RNA was extracted using the RNeasy Micro Kit (QIAGEN). Libraries from $CD8^+$ T cells and basophils were prepared using the NEBNext Ultra RNA Library Prep Kit, and Treg libraries were prepared using the NEBNext Single Cell/Low Input cDNA Synthesis & Amplification Module and Ultra II DNA Library Prep Kit (NEB). Libraries were sequenced on an Illumina NovaSeq 6000 (2 × 150 bp). Reads were mapped and quantified against mm10 using STAR and Salmon through nf-core/rnaseq v3.10.0. Counts were normalized using TMM in edgeR v4.2.1 and voom in limma v3.60.4, and differential expression was determined using limma. Genes with an average TPM <2 or counts <5 per sample were excluded, together with uncharacterized genes, predicted genes and pseudogenes.

Human RNA-seq. Human basophils ($FCεRI^+c\text{-}Kit^-$) and $CD4^+$ Tregs were FACS-sorted from PBMCs before or after 18 h co-culture (>99% purity). RNA was extracted using QIAzol and the RNeasy Micro Kit (QIAGEN), and samples with DV200 >30% were processed using the SMART-Seq Stranded Kit with UMI integration and rRNA depletion (Takara Bio) and sequenced on an AVITI instrument (paired-end, 75 bp). Reads were processed against GRCh38 using STAR, Salmon and featureCounts through nf-core/rnaseq and normalized using TMM/voom. Genes with an average TPM <2 or counts <5 per sample were excluded, together with pseudogenes and uncharacterized genes. For Tregs, only protein-coding genes were retained after exclusion of mitochondrial and ribosomal genes.

scRNA-seq. Lung or cultured immune-cell suspensions were processed using the Chromium Single Cell 3′ Library & Gel Bead Kit v3.1 (10x Genomics) and sequenced on an Illumina NovaSeq 6000 (~20,000 reads per cell). Cell Ranger v7.0.0 was used for processing against mm10. Downstream analyses were performed using Seurat v5.3.0. Cells with ≥200 and <7,500 detected features and <10% mitochondrial transcripts were retained, and doublets were removed using DoubletFinder v2.0.3. Data were normalized using SCTransform, clustered using the Louvain algorithm, visualized by UMAP and annotated using canonical markers. Differential expression was performed using pseudobulk analysis in muscat/edgeR or Seurat FindAllMarkers, retaining genes expressed in ≥10% of cells per population per sample with an average logCPM >5.

Pathway enrichment and bioinformatic analyses. Gene-set enrichment and over-representation analyses were performed using clusterProfiler v4.6.2. Hallmark gene sets were obtained from msigdbr v10.0.1. Gene expression across immune-cell populations was interrogated using the Human Protein Atlas v23.0 and Ensembl v109. TCGA expression and clinical data were analysed using UCSCXenaTools v1.4.7. Single-sample signature scores were calculated using hacksig v0.1.2 and compared using two-sided Student's t-tests with Benjamini–Hochberg correction. DrugBank 6.0 was interrogated using SAveRUNNER.

IgE/IL-33 activation signature. These activation signature were derived from published transcriptomic data38 using genes significantly upregulated following IgE or IL-33 stimulation.

NicheNet analysis. Cell–cell communication was analysed using NicheNet v2.2.0. Ligands expressed in ≥5% of basophils were considered, and receptors with regulatory weights <0.2 were excluded. Differentially expressed genes in receiver cells were identified by pseudobulk analysis (adjusted $P < 0.05$ and $\log_2$ fold change >0.25). The top 20 predicted ligands were used to infer ligand–receptor–target networks, which were visualized using ggalluvial v0.12.5.

Basophil B0 and B1 signature analysis

Data sources and preprocessing. Preprocessed scRNA-seq datasets were obtained from GEO, EGA, Figshare and cellxgene. Human datasets included lung cancer (GSE13190750), colorectal cancer (GSE17831851 and Figshare51), breast cancer (ref.52, EGAS00001004809), pan-cancer (ref.48, cellxgene), and healthy lung, colon and breast tissues from Tabula Sapiens (2022). Mouse datasets included a published 4T1 breast cancer dataset (ref.46, GSE263963) and our mouse lung scRNA-seq dataset. Datasets were reanalyzed using Seurat. Features detected in ≥3 cells and cells with ≥100 detected genes were retained; cells with ≥20% mitochondrial transcripts, nCount_RNA <50 or identified as doublets using scDblFinder v1.16.0 were excluded. Data were normalized, scaled, subjected to PCA and Louvain clustering, visualized by UMAP and annotated using canonical markers. For datasets lacking raw counts, normalized expression matrices from the original study were used.
B0 and B1 signature generation and validation. Steady-state (B0) and tumor-associated (B1) basophil signatures were derived by intersecting dysregulated genes or proteins across four independent datasets: 1) our mouse lung scRNA-seq, which included both tumor-free and tumor-bearing mice, either untreated or treated with paclitaxel; 2) our blood-basophil proteomic dataset; 3) a published mouse lung scRNA-seq dataset46; and 4) a human colorectal cancer scRNA-seq dataset47. Mouse basophils were identified by Mcpt8, Hdc and Cpa3, pseudobulked by biological replicate and analyzed using DESeq2 v1.42.1. Human basophils were identified by FCER1A, HDC, MS4A2, GATA2 and CPA3, and differential expression was determined using Seurat FindMarkers. Genes with adjusted $P < 0.05$ were retained and assigned to B1 or B0 according to their direction of change in tumor-associated versus tumor-free basophils. Proteomic differential abundance analysis was performed as described above, retaining proteins with FDR < 0.05 and assigning them to B1 or B0 according to their direction of change. The resulting B0 and B1 signatures were independently validated using UCell (AddModuleScore_UCell) in mouse and human basophil scRNA-seq datasets50–52 and Tabula Sapiens.

Human transcriptomic and survival analyses

Melanoma Treg analysis. scRNA-seq data and clinical annotations from patients with melanoma were obtained from ref.45. Tregs were defined as $CD4^+FOXP3^+CD25^+$ cells and assigned to treatment groups according to the original clinical annotations. Transcriptional regulatory networks were inferred using SCENIC v1.3.1 on GSE94396 and ref.43. Regulon activity was quantified using AUCell v1.24.0, and specificity was assessed using Regulon Specificity Scores.

Association of intratumoural basophils with survival. For KM-Plotter analyses, basophil abundance was estimated from the combined expression of IL3RA, CCR3 and FCER1A. Patients with breast, colorectal, gastric, lung, ovarian or liver cancer were stratified into tertiles, and survival was compared between the equally sized highest (T3) and lowest (T1) tertiles using the log-rank test. Kaplan–Meier curves were reformatted using the survival and ggsurvfit R packages.

For TCGA and METABRIC analyses, primary tumour expression and survival data were obtained through cBioPortal. Gene expression was z-score-normalized using hacksig. Kaplan–Meier analyses used survival v3.8-3 and survminer v0.5.1, with follow-up censored at 5 years and significance assessed using the log-rank test. Tumours were stratified by expression of FCER1A, HDC, MS4A2, GATA2 and CPA3, and basophil-high tumours were further classified according to the B0 and B1 signatures.

Lung basophil–Treg correlation. Lung tumour and adjacent normal scRNA-seq/CITE-seq data were obtained from ref.77. Basophils were identified as $CD123^+CD117^-FCER1A^+CCR3^+$ cells, with TPSAB1 and TPSB2 used as ancillary markers, and Tregs were identified by CD4, IL2RA and FOXP3. Samples containing <1,000 or >10,000 cells, generated using older library protocols or lacking CD45 enrichment were excluded. Pearson correlation was used to assess the association between basophil and Treg abundance.

Visium HD spatial transcriptomics

Processing and analysis. KP lungs were harvested 127 days after intratracheal lentiviral Cre delivery, embedded in OCT and processed using the 10x Genomics Visium HD CytAssist FFPE workflow. Libraries were sequenced on NovaSeq 6000 and AVITI platforms and processed using Space Ranger v3.1.0 against mm10-2020-A. Visium HD data were imported using bin2cell v0.3.3, spatial striping was corrected using destripe, and expression counts were normalized and log-transformed using Scanpy v1.11.2.

Nuclei were segmented using StarDist (2D_versatile_he) in bin2cell and expanded to approximate whole-cell boundaries. Transcript counts were aggregated at the cell level, and cells were annotated in Seurat using mouse lung scRNA-seq-derived signatures quantified with UCell. Spatial visualizations were generated using B2CViz v1.0.0.

Spatial proximity analysis. Euclidean distances between Tregs and the nearest basophil were calculated using get.knnx in FNN v1.1.4, with Tregs classified as near or far using a 50-µm threshold. IL-2–STAT5 Hallmark pathway activity was quantified using UCell, and groups were compared using pairwise t-tests in ggpubr v0.6.1.

Association of blood basophil counts with survival

Adult patients with a primary malignant tumour diagnosed at CHUV between 2000 and 2020 and institutional research consent were included; patients with benign tumours or carcinoma in situ were excluded. Absolute blood basophil counts were available for 11,164 patients. After removing duplicate measurements and median-imputing missing values, mean basophil counts from diagnosis to death, last follow-up or data extraction were calculated as previously described53. Patients were stratified according to the median basophil count (0.03 G/L), and survival was compared by Kaplan–Meier analysis and log-rank test using lifelines v0.27.8.

Prospective clinical trial

We conducted a randomized, double-blind, placebo-controlled crossover trial involving 40 healthy adult volunteers. Recruitment was

conducted between 21 June and 21 August 2024. The trial is reported in accordance with the CONSORT 2010 guidelines, and the study protocol and completed CONSORT checklist are provided in the Supplementary Information. Both male and female healthy volunteers aged 20–30 years were enrolled. Biological sex was self-reported and recorded as a biological variable. The study was not designed or powered to detect sex-specific differences. Baseline age and sex were balanced between treatment-sequence groups at randomization.

Participants were randomized 1:1 in 10 blocks of four to receive placebo followed by loratadine or the reverse sequence, using Sealed Envelope. Drug and placebo were identically packaged and coded by an independent clinical laboratory expert. Participants, investigators and outcome assessors were blinded, and allocation was concealed from the data analyst until completion of the analysis. Participants received loratadine (10 mg daily) or placebo for 21 days per period without a washout period. The primary endpoint was the change in Treg frequency following loratadine compared with placebo. The prespecified secondary endpoint was the number of $CD8^+$ effector T cells; this outcome is not reported here because it was outside the scope of the present study, which focused on basophil–Treg interactions.

Peripheral blood was collected at the end of each treatment period. PBMCs were isolated and analysed by flow cytometry following staining with CD4-FITC and CD25-PE antibodies (BioLegend). Tregs were identified as $CD4^+CD25^+$ lymphocytes using fluorescence-minus-one controls for gating.

Six participants withdrew before day 22. An additional four participants in Group A and five in Group B missed the day 42 blood draw, resulting in 29 loratadine-treated and 30 placebo-treated samples. Paired crossover analyses included only complete treatment pairs (see Supplementary Table 1 for participant characteristics).

Data distributions were assessed using the Shapiro–Wilk, D'Agostino–Pearson, Anderson–Darling and Kolmogorov–Smirnov tests together with Q–Q plots. Because the data were not normally distributed, unpaired comparisons were performed using the Mann–Whitney test, and paired crossover analyses were performed using the Wilcoxon signed-rank test. Sample size was estimated from a previous study78 assuming a 20% treatment effect, $\alpha = 0.05$ and 80% power, requiring 32 participants. To account for an anticipated 20% dropout rate, 40 participants were enrolled.

Mathematical modelling of cell interactions

A mechanistic ordinary differential equation model describing interactions between cancer cells, Tregs, $CD8^+$ T cells and basophils was implemented in MATLAB using the ode15s solver and mass-action kinetics79 (Extended Data Fig. 5Q). Initial cell numbers and experimental timing matched the in vitro assays. Parameters governing proliferation, death and immune interactions, including basophil-mediated Treg apoptosis and inhibition of Treg-mediated $CD8^+$ T-cell suppression, were fitted to experimental measurements. Model files and equations are available at https://github.com/FinleyLabUSC/Basophil-immune-model/, and parameter values are provided in Supplementary Table 5.

For manuscripts utilizing custom algorithms or software that are central to the research but not yet described in published literature, software must be made available to editors and reviewers. We strongly encourage code deposition in a community repository (e.g. GitHub). See the Nature Portfolio guidelines for submitting code & software for further information.

Data

Policy information about availability of data

All manuscripts must include a data availability statement. This statement should provide the following information, where applicable:

- Accession codes, unique identifiers, or web links for publicly available datasets
- A description of any restrictions on data availability
- For clinical datasets or third party data, please ensure that the statement adheres to our policy

Data availibility
Sequencing and spatial transcriptomics data generated in this study are available in GEO under accession codes GSE266677 [https://www.ncbi.nlm.nih.gov/geo/query/acc.cgi?acc=GSE266677] and GSE341382 [https://www.ncbi.nlm.nih.gov/geo/query/acc.cgi?acc=GSE341382]. Mass spectrometry proteomics data are available through PRIDE under accession code PXD082224 [https://www.ebi.ac.uk/pride/archive/projects/PXD082224]. Publicly available datasets used in this study are available in GEO under accession codes GSE131907 [https://www.ncbi.nlm.nih.gov/geo/query/acc.cgi?acc=GSE131907], GSE178318 [https://www.ncbi.nlm.nih.gov/geo/query/acc.cgi?acc=GSE178318], GSE263963 [https://www.ncbi.nlm.nih.gov/geo/query/acc.cgi?acc=GSE263963] and GSE94396 [https://www.ncbi.nlm.nih.gov/geo/query/acc.cgi?acc=GSE94396].
De-identified prospective trial data are provided as Source Data. The study protocol is included in the Supplementary Information. Individual-level clinical data from retrospective studies and biobanked biological samples cannot be made publicly available because access is restricted under the approved study protocols and applicable institutional data-protection requirements. Requests for access for academically led research may be considered subject to the relevant institutional and ethical approvals and appropriate data- or material-transfer agreements.
The remaining data are available within the Article, its supplementary information files or Source Data file.

Code availability
The mathematical model and custom code developed for the cell-interaction simulations in this study are publicly available at https://zenodo.org/records/22773668 (ref.80).

Human research participants

Policy information about studies involving human research participants and Sex and Gender in Research.

Reporting on sex and gender	For functional analyses using immune cells isolated from PBMCs from healthy donors, age and sex were not considered in the study design or analysis. For the retrospective survival analysis and CCL24 quantification in bronchial aspirates, age and sex

were recorded but were not included as analytical variables. The retrospective analysis focused on the association between blood basophil levels and survival.For the prospective clinical trial, both male and female healthy volunteers were enrolled. Biological sex was self-reported and recorded as a biological variable. The study was not designed or powered to detect sex-specific differences. Age and sex were balanced between treatment-sequence groups (Supplementary Table 1).

Population characteristics

The retrospective cohort included adult patients with a primary malignant tumour diagnosed at Lausanne University Hospital (CHUV) between 2000 and 2020 who had provided institutional consent for research. Patients with benign tumours or carcinoma in situ were excluded. Absolute blood basophil counts were available for 11,164 patients.
For CCL24 quantification, bronchial aspirates were obtained from patients undergoing diagnostic bronchoscopy at CHUV. Patients with active lung infection, a history of asthma or severe allergies were excluded.

The prospective clinical trial included healthy male and female volunteers aged 20–30 years. Baseline age and sex were balanced between treatment-sequence groups at randomization.

For functional experiments, PBMCs were obtained from healthy blood donors. No specific donor characteristics were considered in the study design or analysis.

Recruitment

Clinical trial:
Participants were recruited at Imam Hossein Hospital through local advertisements.

Functional analysis of immune cells:
Peripheral blood from healthy donors was obtained from the Blood Transfusion Center (Lausanne, Switzerland) under protocol P_297.

Bronchial aspirate CCL24 quantification:
Samples were obtained from the “Biomark Lung” biobank (CHUV_2022_023_RM), comprising bronchial aspirates collected from patients undergoing diagnostic evaluation for suspected lung cancer.

Retrospective clinical cohort:
Patients were identified retrospectively from electronic medical records at Lausanne University Hospital (CHUV). Eligible patients were adults diagnosed with a primary malignant tumour between 2000 and 2020 who had provided institutional consent for research and had available blood basophil measurements. Patients with benign tumours or carcinoma in situ were excluded. No prospective recruitment was performed.

Ethics oversight

Human buffy coats from healthy donors were obtained from the Lausanne Blood Transfusion Center under Project P_297. No ethical approval was required for the use of these samples, and written informed consent was obtained by the provider.

Bronchial aspirates were obtained from patients undergoing diagnostic bronchoscopy at Lausanne University Hospital (CHUV), collected and biobanked under registry CHUV_2022_023_RM, and analysed with approval from the Cantonal Ethics Committee of Vaud (VD2022-01536). All included patients had provided written institutional consent for research.
The retrospective study of patients with cancer at CHUV was approved by the Commission cantonale d’éthique de la recherche sur l’être humain (CER-VD2020-02322). All included patients had provided written institutional consent for research.

The prospective clinical trial in healthy volunteers was approved by the Shaheed Beheshti Medical University Ethics Committee (IR.SBMU.RETECH.REC.1402.304) and conducted in accordance with the Declaration of Helsinki and applicable regulations governing research involving human participants. All participants provided written informed consent and received financial compensation for participation. The trial was prospectively registered in the Iranian Registry of Clinical Trials (IRCT20170608034390N14, https://www.irct.ir/trial/77072).

Note that full information on the approval of the study protocol must also be provided in the manuscript.

Field-specific reporting

Please select the one below that is the best fit for your research. If you are not sure, read the appropriate sections before making your selection.

☒ Life sciences ☐ Behavioural & social sciences ☐ Ecological, evolutionary & environmental sciences

For a reference copy of the document with all sections, see nature.com/documents/nr-reporting-summary-flat.pdf

Life sciences study design

All studies must disclose on these points even when the disclosure is negative.

Sample size

Mouse experiments comprised independent biological replicates and were performed in one or two independent cohorts. Sample sizes were not predetermined using statistical methods but were based on our previous experience with the respective tumour models, including their expected biological variability and effect sizes. Experiments involving mouse primary cells typically used 3–9 independent cultures per group, based on our previous experience with these assays. Sample sizes and statistical tests are indicated in the figure legends. Experiments involving human primary cells used three to four independent donors, and the statistical analyses applied are indicated in the figure legends. For the clinical trial, sample size was estimated from a previous study assuming a 20% treatment effect, $\alpha = 0.05$ and 80% power, requiring 32

participants. To account for an anticipated 20% dropout rate, 40 participants were enrolled. For metastatic mouse models, animals were not randomly allocated because experimental groups were defined before or at the time of tumour inoculation. For studies involving established disease, mice were randomized to treatment groups before treatment initiation where applicable. Mice of the same strain, sex and similar age were used within each experiment to minimize potential confounding. Where applicable, control and treatment groups were studied concurrently under the same experimental conditions.For in vitro experiments, primary cells were allocated to experimental conditions according to the predefined study design, with cells from the same biological samples distributed across control and treatment conditions where applicable.For the clinical trial, participants were randomized 1:1 to receive placebo followed by loratadine or vice versa using block randomization (10 blocks of four participants), with the allocation sequence generated using the Sealed Envelope online randomization service.

Data exclusions

No animals or data points were excluded as outliers. In rare instances, individual samples were excluded from specific analyses owing to technical failures during sample collection, processing or data acquisition.

Replication

Mouse studies were performed in one or two independent cohorts. Cell-culture experiments were performed in 1–3 independent experiments. Each value represents an independent primary-cell co-culture, in which primary cells were independently assembled and treated in separate wells. Each well constitutes an independently established biological culture and was subjected to the experimental conditions independently. Accordingly, individual wells were considered independent biological replicates for the purpose of assessing variability and treatment effects. RNA-sequencing experiments were performed once. Biological replicates are defined in the figure legends.

Randomization

For metastatic lung models, randomization was not performed because treatment groups were defined before or at the time of tumour inoculation. For studies involving established disease, mice were randomized to treatment groups before treatment initiation where applicable. In the EAE experiment, mice were randomly assigned to treatment groups.Double-blind, randomized crossover clinical trial: The 40 participants were randomized 1:1 to two treatment-sequence groups of 20 participants: placebo followed by loratadine or loratadine followed by placebo. Block randomization was performed using 10 blocks of four participants, with equal allocation to the two treatment sequences within each block. The allocation sequence was generated using the Sealed Envelope online randomization service (www.sealedenvelope.com).

Blinding

Mouse studies: Drug administration in mouse tumour experiments was performed by investigators aware of group allocation. Investigators were blinded during tumour growth measurements, immunofluorescence acquisition and quantification, and flow-cytometry acquisition where applicable, using anonymized mouse identification numbers. Flow-cytometry analysis was not blinded because of manual gating and access to experimental codes. EAE clinical scoring was performed blinded to treatment group. In the clinical trial, participants, investigators and outcome assessors were blinded, and treatment allocation remained concealed from the data analyst until completion of the analysis

Clinical trial: Drug and placebo were packaged in identical bottles and coded according to the randomization list by an independent clinical laboratory expert who was not involved in the study. Participants, investigators and outcome assessors remained blinded, and treatment allocation was concealed from the data analyst until completion of the analysis.

Reporting for specific materials, systems and methods

We require information from authors about some types of materials, experimental systems and methods used in many studies. Here, indicate whether each material, system or method listed is relevant to your study. If you are not sure if a list item applies to your research, read the appropriate section before selecting a response.

Materials & experimental systems

n/a	Involved in the study
☐	☒ Antibodies
☐	☒ Eukaryotic cell lines
☒	☐ Palaeontology and archaeology
☐	☒ Animals and other organisms
☐	☒ Clinical data
☒	☐ Dual use research of concern

Methods

n/a	Involved in the study
☒	☐ ChIP-seq
☐	☒ Flow cytometry
☒	☐ MRI-based neuroimaging

Antibodies

Antibodies used

A list of antibodies is provided. We indicate the following: Antigen; Fluorochrome; Reactivity; Clone; Provider; Reference (catalogue #); Dilution.

FLOW CYTOMETRY

Antibodies Compagny Reference Clone Dilution
CD3 APC 100236 Biolegend 17A2 1 : 100 https://www.biolegend.com/en-us/products/apc-anti-mouse-cd3-antibody-8055
CD25 Brillant Violet 605 102036 Biolegend PC61 1 : 100 https://www.biolegend.com/en-us/products/brilliant-violet-605-anti-mouse-cd25-antibody-7639
FC block (mouse) 553142 BD Biosciences 2,4G2 1 : 100 https://www.bdbiosciences.com/en-us/products/reagents/flow-cytometry-reagents/research-reagents/single-color-antibodies-ruo/purified-rat-anti-mouse-cd16-cd32-mouse-bd-fc-block.553142
CD45 Pacific blue 103126 Biolegend 30-F11 1 : 100 https://www.biolegend.com/en-us/products/pacific-blue-anti-mouse-cd45-

antibody-3102
CD4 Alexa Fluor 488 100529 Biolegend RM4-5 1 : 100 https://www.biolegend.com/en-us/products/alexa-fluor-488-anti-mouse-cd4-antibody-2697
CD44 Alexa Fluor 488 103016 Biolegend IM7 1 : 100 https://www.biolegend.com/en-us/products/alexa-fluor-488-anti-mouse-human-cd44-antibody-3097
PD-1 PE 114117 Biolegend RMP1-14 1 : 100 https://www.biolegend.com/en-us/products/pe-anti-mouse-cd279-pd-1-antibody-12737
FoxP3 PE 12-5773-80 invitrogen FJK-16s 1 : 100 https://www.thermofisher.com/antibody/product/FOXP3-Antibody-clone-FJK-16s-Monoclonal/12-5773-82
CD11b Brillant Violet 711 101241 Biolegend M1/70 1 : 100 https://www.biolegend.com/en-us/products/brilliant-violet-711-anti-mouse-human-cd11b-antibody-7927
CD49b Fitc 103503 Biolegend HMa2 1 : 100 https://www.biolegend.com/en-us/products/fitc-anti-mouse-cd49b-antibody-297
CD69 Pacific blue 104523 Biolegend H1.2F3 1 : 100 https://www.biolegend.com/en-us/products/pacific-blue-anti-mouse-cd69-antibody-4403
FCER1a PE 134307 Biolegend Mar-01 1 : 100 https://www.biolegend.com/en-us/products/pe-anti-mouse-fcepsilonrialpha-antibody-5950
CD117 APC 105812 Biolegend 2B8 1 : 100 https://www.biolegend.com/en-us/products/apc-anti-mouse-cd117-c-kit-antibody-72
CD4 Brillant Violet605 100547 Biolegend RM4-5 1 : 100 https://www.biolegend.com/en-us/products/brilliant-violet-605-anti-mouse-cd4-antibody-7627
CD25 APC Cy7 101918 Biolegend 3C7 1 : 100 https://www.biolegend.com/en-us/products/apc-cyanine7-anti-mouse-cd25-antibody-14316
CD200R3 APC 142208 Biolegend Ba13 1:100 https://www.biolegend.com/en-gb/products/apc-anti-mouse-cd200r3-antibody-8240?GroupID=BLG10519
Granzyme B PE Texas GRB17 Thermofisher scientific GB11 1 : 100 https://www.thermofisher.com/antibody/product/Granzyme-B-Antibody-clone-GB11-Monoclonal/GRB17
Cell trace Violet C34571 Thermofisher scientific 1 : 100 https://www.thermofisher.com/order/catalog/product/C34571
CD8 APC Cy7 100714 Biolegend 53-6.7 1:100 https://www.biolegend.com/en-gb/products/apc-cyanine7-anti-mouse-cd8a-antibody-2269
Fixable Aqua Dead cell stain kit 405nm excitation L34965 Thermofisher scientific 1 : 1000 https://www.thermofisher.com/order/catalog/product/L34965?SID=srch-hj-L34965
CD4 FITC anti-human 300506 BioLegend RPA-T4 1 : 100 https://www.biolegend.com/en-us/products/fitc-anti-human-cd4-antibody-825
CD25 PE anti-human 302606 BioLegend BC96 1 : 100 https://www.biolegend.com/en-us/products/pe-anti-human-cd25-antibody-616
FC Block (validated in human) 14-0161-82 Thermofisher scientific 93 1 : 100 CD16/CD32 Monoclonal Antibody (93), eBioscience™ | Invitrogen (14-0161-82)
anti-mCherry unconjugated ab205402 abcam polyclonal 1 : 100 https://www.abcam.com/en-us/products/primary-antibodies/mcherry-antibody-ab205402
anti-GFP A11122 ThermoFisher Scientific polyclonal 1 : 100 https://www.thermofisher.com/antibody/product/GFP-Antibody-Polyclonal/A-11122
anti-MCPT8 647401 Biolegend Tug8 1 : 100 https://www.biolegend.com/en-us/products/purified-anti-mmcp-8-antibody-6266
anti-FOXP3 14-5773-82 ebiosciences FJK-16s 1 : 100 https://www.thermofisher.com/antibody/product/FOXP3-Antibody-clone-FJK-16s-Monoclonal/14-5773-82
anti-foxp3 ab75763 abcam polyclonal 1 : 200 https://www.abcam.com/en-us/products/primary-antibodies/foxp3-antibody-ab75763
anti basophil antibody ab155577 abcam 2D7 1 : 100 https://www.abcam.com/en-us/products/primary-antibodies/basophils-antibody-2d7-ab155577
IL4 PE Cy7 504117 Biolegend "11B11" 1 : 100 https://www.biolegend.com/fr-ch/products/pe-cyanine7-anti-mouse-il-4-antibody-7119?GroupID=BLG1753&__cf_chl_tk=D6g39wiW9IUJ8q7GreIldObw09n5Y4VvFHcgSZDV88Y-1756984313-1.0.1.1-3VwOIPdZ0W_fmo_uzPpuh5N.Ga.6o7YjXlKsn8MphXQ
IL13 PE dazzle 159411 Biolegend W17010B 1 : 100 https://www.biolegend.com/fr-ch/products/pedazzle-594-anti-mouse-il-13-antibody-24702
IL6 APC 504507 Biolegend MP5-20F3 1 : 100 https://www.biolegend.com/fr-ch/products/apc-anti-mouse-il-6-antibody-7035
IL-2Rα/CD25 36128 Cell signaling E4B2Z 01:40 IL-2Rα/CD25 (E4B2Z) XP® Rabbit mAb | Cell Signaling Technology
CD25 Chimeric Recombinant MA548169 Thermofisher scientific PC-61.5.3 1 : 100 CD25 Chimeric Recombinant Monoclonal Antibody (PC-61.5.3) (MA5-48169)
anti-HRH1 PA5-102098 Invitrogen Polyclonal 1 : 40 HRH1 Polyclonal Antibody (PA5-102098)
anti-actin MAB8929 R&D 937215 1 : 40 Anti-beta Actin Antibody MAB8929: R&D Systems
anti -DJ1 5933 Cell signalling D29E5 01:40 https://www.cellsignal.com/products/primary-antibodies/dj-1-d29e5-xp-rabbit-mab/5933
anti IgE Biotin 406903 Biolegend RME-1 1 : 100 https://www.biolegend.com/fr-fr/products/biotin-anti-mouse-ige-2517
anti IgE FITC 406906 Biolegend RME-1 1 : 100 https://www.biolegend.com/fr-fr/products/fitc-anti-mouse-ige-3266
anti-HSP90 4877 Cell signaling C45G5 1 : 1000 https://www.cellsignal.com/products/primary-antibodies/hsp90-c45g5-rabbit-mab/4877?srsltid=AfmBOoojubQyIV8HWv7QTKHjxs9jryXY25zxS_wICNu4UPQrknjn6CwN
CD206 PE 141705 Biolegend C068C2 1 : 100 PE anti-mouse CD206 MMR Antibody anti-CD206 - C068C2
Arginase 1 AF488 53-3697-82 ThermoFisher Scientific A1exF5 1 : 100 https://www.thermofisher.com/antibody/product/Arginase-1-Antibody-clone-A1exF5-Monoclonal/53-3697-82

Validation

Antibodies Compagny Reference Clone Dilution
CD3 APC 100236 Biolegend 17A2 1 : 100 https://www.biolegend.com/en-us/products/apc-anti-mouse-cd3-antibody-8055
CD25 Brillant Violet 605 102036 Biolegend PC61 1 : 100 https://www.biolegend.com/en-us/products/brilliant-violet-605-anti-mouse-cd25-antibody-7639
FC block (mouse) 553142 BD Biosciences 2,4G2 1 : 100 https://www.bdbiosciences.com/en-us/products/reagents/flow-cytometry-reagents/research-reagents/single-color-antibodies-ruo/purified-rat-anti-mouse-cd16-cd32-mouse-bd-fc-block.553142
CD45 Pacific blue 103126 Biolegend 30-F11 1 : 100 https://www.biolegend.com/en-us/products/pacific-blue-anti-mouse-cd45-antibody-3102
CD4 Alexa Fluor 488 100529 Biolegend RM4-5 1 : 100 https://www.biolegend.com/en-us/products/alexa-fluor-488-anti-mouse-cd4-

antibody-2697
CD44 Alexa Fluor 488 103016 Biolegend IM7 1 : 100 https://www.biolegend.com/en-us/products/alexa-fluor-488-anti-mouse-human-cd44-antibody-3097
PD-1 PE 114117 Biolegend RMP1-14 1 : 100 https://www.biolegend.com/en-us/products/pe-anti-mouse-cd279-pd-1-antibody-12737
FoxP3 PE 12-5773-80 invitrogen FJK-16s 1 : 100 https://www.thermofisher.com/antibody/product/FOXP3-Antibody-clone-FJK-16s-Monoclonal/12-5773-82
CD11b Brillant Violet 711 101241 Biolegend M1/70 1 : 100 https://www.biolegend.com/en-us/products/brilliant-violet-711-anti-mouse-human-cd11b-antibody-7927
CD49b Fitc 103503 Biolegend HMa2 1 : 100 https://www.biolegend.com/en-us/products/fitc-anti-mouse-cd49b-antibody-297
CD69 Pacific blue 104523 Biolegend H1.2F3 1 : 100 https://www.biolegend.com/en-us/products/pacific-blue-anti-mouse-cd69-antibody-4403
FCER1a PE 134307 Biolegend Mar-01 1 : 100 https://www.biolegend.com/en-us/products/pe-anti-mouse-fcepsilonrialpha-antibody-5950
CD117 APC 105812 Biolegend 2B8 1 : 100 https://www.biolegend.com/en-us/products/apc-anti-mouse-cd117-c-kit-antibody-72
CD4 Brillant Violet605 100547 Biolegend RM4-5 1 : 100 https://www.biolegend.com/en-us/products/brilliant-violet-605-anti-mouse-cd4-antibody-7627
CD25 APC Cy7 101918 Biolegend 3C7 1 : 100 https://www.biolegend.com/en-us/products/apc-cyanine7-anti-mouse-cd25-antibody-14316
CD200R3 APC 142208 Biolegend Ba13 1:100 https://www.biolegend.com/en-gb/products/apc-anti-mouse-cd200r3-antibody-8240?GroupID=BLG10519
Granzyme B PE Texas GRB17 Thermofisher scientific GB11 1 : 100 https://www.thermofisher.com/antibody/product/Granzyme-B-Antibody-clone-GB11-Monoclonal/GRB17
Cell trace Violet C34571 Thermofisher scientific 1 : 100 https://www.thermofisher.com/order/catalog/product/C34571
CD8 APC Cy7 100714 Biolegend 53-6.7 1:100 https://www.biolegend.com/en-gb/products/apc-cyanine7-anti-mouse-cd8a-antibody-2269
Fixable Aqua Dead cell stain kit 405nm excitation L34965 Thermofisher scientific 1 : 1000 https://www.thermofisher.com/order/catalog/product/L34965?SID=srch-hj-L34965
CD4 FITC anti-human 300506 BioLegend RPA-T4 1 : 100 https://www.biolegend.com/en-us/products/fitc-anti-human-cd4-antibody-825
CD25 PE anti-human 302606 BioLegend BC96 1 : 100 https://www.biolegend.com/en-us/products/pe-anti-human-cd25-antibody-616
FC Block (validated in human) 14-0161-82 Thermofisher scientific 93 1 : 100 CD16/CD32 Monoclonal Antibody (93), eBioscience™ | Invitrogen (14-0161-82)
anti-mCherry unconjugated ab205402 abcam polyclonal 1 : 100 https://www.abcam.com/en-us/products/primary-antibodies/mcherry-antibody-ab205402
anti-GFP A11122 ThermoFisher Scientific polyclonal 1 : 100 https://www.thermofisher.com/antibody/product/GFP-Antibody-Polyclonal/A-11122
anti-MCPT8 647401 Biolegend Tug8 1 : 100 https://www.biolegend.com/en-us/products/purified-anti-mmcp-8-antibody-6266
anti-FOXP3 14-5773-82 ebiosciences FJK-16s 1 : 100 https://www.thermofisher.com/antibody/product/FOXP3-Antibody-clone-FJK-16s-Monoclonal/14-5773-82
anti-foxp3 ab75763 abcam polyclonal 1 : 200 https://www.abcam.com/en-us/products/primary-antibodies/foxp3-antibody-ab75763
anti basophil antibody ab155577 abcam 2D7 1 : 100 https://www.abcam.com/en-us/products/primary-antibodies/basophils-antibody-2d7-ab155577
IL4 PE Cy7 504117 Biolegend "11B11" 1 : 100 https://www.biolegend.com/fr-ch/products/pe-cyanine7-anti-mouse-il-4-antibody-7119?GroupID=BLG1753&__cf_chl_tk=D6g39wiW9IUJ8q7GreIldObw09n5Y4VvFHcgSZDV88Y-1756984313-1.0.1.1-3VwOIPdZ0W_fmo_uzPpuh5N.Ga.6o7YjXlKsn8MphXQ
IL13 PE dazzle 159411 Biolegend W17010B 1 : 100 https://www.biolegend.com/fr-ch/products/pedazzle-594-anti-mouse-il-13-antibody-24702
IL6 APC 504507 Biolegend MP5-20F3 1 : 100 https://www.biolegend.com/fr-ch/products/apc-anti-mouse-il-6-antibody-7035
IL-2Rα/CD25 36128 Cell signaling E4B2Z 01:40 IL-2Rα/CD25 (E4B2Z) XP® Rabbit mAb | Cell Signaling Technology
CD25 Chimeric Recombinant MA548169 Thermofisher scientific PC-61.5.3 1 : 100 CD25 Chimeric Recombinant Monoclonal Antibody (PC-61.5.3) (MA5-48169)
anti-HRH1 PA5-102098 Invitrogen Polyclonal 1 : 40 HRH1 Polyclonal Antibody (PA5-102098)
anti-actin MAB8929 R&D 937215 1 : 40 Anti-beta Actin Antibody MAB8929: R&D Systems
anti -DJ1 5933 Cell signalling D29E5 01:40 https://www.cellsignal.com/products/primary-antibodies/dj-1-d29e5-xp-rabbit-mab/5933
anti IgE Biotin 406903 Biolegend RME-1 1 : 100 https://www.biolegend.com/fr-fr/products/biotin-anti-mouse-ige-2517
anti IgE FITC 406906 Biolegend RME-1 1 : 100 https://www.biolegend.com/fr-fr/products/fitc-anti-mouse-ige-3266
anti-HSP90 4877 Cell signaling C45G5 1 : 1000 https://www.cellsignal.com/products/primary-antibodies/hsp90-c45g5-rabbit-mab/4877?srsltid=AfmBOoojubQyIV8HWv7QTKHjxs9jryXY25zxS_wICNu4UPQrknjn6CwN
CD206 PE 141705 Biolegend C068C2 1 : 100 PE anti-mouse CD206 MMR Antibody anti-CD206 - C068C2
Arginase 1 AF488 53-3697-82 ThermoFisher Scientific A1exF5 1 : 100 https://www.thermofisher.com/antibody/product/Arginase-1-Antibody-clone-A1exF5-Monoclonal/53-3697-82

Eukaryotic cell lines

Policy information about cell lines and Sex and Gender in Research

Cell line source(s)	The KrasG12D;Trp53-null lung adenocarcinoma cell line (KP; male origin), previously described in our publications (Martinez-Usatorre et al., 2021; Duval et al., 2024), was transduced with a lentiviral construct encoding GFP, as previously described (Squadrito et al., 2018), to generate the KP-GFP cell line. The 4T1 mammary adenocarcinoma cell line (female origin; ATCC CRL-2539) was engineered to express a CD9–mCherry fusion protein to generate the 4T1-CD9-mCh cell line, as previously described by our group (Keklikoglou et al., 2018). The MC38-OVA and PyMT cell lines, both of female origin, were also described previously (Squadrito et al., 2018; Keklikoglou et al., 2018).

Authentication	While the original stocks of cancer cell lines were authenticated, we did not perform further authentication in the past several months.
Mycoplasma contamination	All cell lines have tested negative for Mycoplasma contamination in tests routinely performed in the laboratory.
Commonly misidentified lines (See ICLAC register)	None

Animals and other research organisms

Policy information about studies involving animals; ARRIVE guidelines recommended for reporting animal research, and Sex and Gender in Research

Laboratory animals	All animal experiments complied with relevant ethical regulations and were approved by the Cantonal Veterinary Office of Vaud (protocols VD2978.2, VD3435.1, VD3785, VD3953 and VD4176) or by the Institutional Animal Care and Use Committee of Brigham and Women's Hospital. Mice We used female BALB/cJ (Jackson Laboratory stock #000651) and FVB/NJ (#001800) mice for mammary tumour models, male C57BL/6J mice (#000664) for lung tumour models, female C57BL/6J mice for the EAE model, and female OT-I mice (#003831) as T-cell donors. C57BL/6J mice of either sex were used for bone marrow and spleen cell isolation. Female CD45.1 (B6.SJL-Ptprc^{a} Pepc^{b}/BoyJ; #002014), Foxp3-DTR (B6.129(Cg)-Foxp3tm3(HBEGF/GFP)Ayr/J; #016958) and KrasLSL-G12D/+;Trp53fl/fl mice, previously described by us23, were used as indicated. BALB/cJ, C57BL/6J, FVB/NJ and OT-I mice were purchased from The Jackson Laboratory, whereas the other strains were bred in-house. All mice were maintained under specific pathogen-free conditions at the EPFL or Agora animal facilities in Lausanne, Switzerland, or at the Brigham and Women's Hospital animal facility in Boston, USA. Mice were housed in groups of up to five mice per cage at 18–24 °C and 40–60% humidity and maintained on a 12-h light/dark cycle (6 a.m. to 6 p.m.). Food and water were available ad libitum. Male and female mice were used as indicated for each disease model. Sex was selected according to established experimental models and was not evaluated as an independent biological variable. Mouse tumor models and interventions Experimental lung metastases were established by intravenous injection of 2 × 105 KP-GFP cells into 8-week-old male C57BL/6 mice or 2-5 × 104 4T1 or 4T1-CD9-mCherry cells into 8-week-old female BALB/c mice. Tumor development was monitored by micro-CT as described previously23,74. Orthotopic KP lung tumors were generated by intravenous injection of multicellular KP spheroids (~50 cells per spheroid) prepared as previously described23 and lung tumor growth was monitored by micro-CT as described23,74. The maximum authorized size of individual lung tumors (3 mm in diameter) was not exceeded. Subcutaneous mammary tumors were induced by implantation of 7.5 × 103 or 5 × 105 4T1 or 4T1-CD9-mCherry cells into the right flank of 6–8-week-old female BALB/c mice. Orthotopic mammary tumors were established by implantation of 2 × 105 PyMT cells into the mammary fat pad of 8-week-old female FVB/N mice. Tumor volume was calculated as (length × width2)/3. The maximum authorized tumor volume (1,000 mm3) was not exceeded. Where indicated, mice received intravenous anti-CD200R3 antibody (clone Ba103, 20 µg per mouse; Hycult Biotech) or isotype control. Loratadine or diphenhydramine (20 mg/kg/day, Sigma) was administered orally in carboxymethyl cellulose. Where indicated, paclitaxel (10 mg/kg; Labatec) or vehicle was administered intraperitoneally every 3 days from day 17 after subcutaneous 4T1 tumor-cell implantation, as previously described22. Drug administration schedules and mouse euthanasia time points are indicated in the figures. Experimental autoimmune encephalitis model EAE was induced as previously described76. Briefly, 8-week-old female C57BL/6 mice were immunized subcutaneously with myelin oligodendrocyte glycoprotein (MOG)35–55 peptide emulsified in complete Freund's adjuvant containing Mycobacterium tuberculosis H37Ra, followed by intraperitoneal pertussis-toxin administration on the day of immunization and 2 days later. Loratadine (20 mg kg^{-1} day^{-1}) or vehicle (CMC) was administered by oral gavage from 7 days before immunization until day 25. Clinical disease was assessed daily using a 0–5 neurological scoring scale. Mice were randomly assigned to treatment groups, and clinical scoring was performed blinded to treatment group.
Wild animals	The study did not involve wild animals.
Reporting on sex	Experiments involving 4T1 and PyMT mammary tumour cells used female mice, whereas experiments involving transplanted KP cancer cells used male mice. Female mice were used for the EAE model and as OT-I T-cell donors. Female CD45.1, Foxp3-DTR and transgenic KP mice were used as indicated. C57BL/6J mice of either sex were used for bone marrow-derived cell and splenocyte isolation. Sex was selected according to established experimental models and was not evaluated as an independent biological variable.
Field-collected samples	None
Ethics oversight	All animal experiments complied with relevant ethical regulations and were approved by the Cantonal Veterinary Office of Vaud (protocols VD3435.1, VD2978.2, VD3953, VD4176 and VD3785) or by the Institutional Animal Care and Use Committee of Brigham and Women's Hospital.

Note that full information on the approval of the study protocol must also be provided in the manuscript.

Clinical data

Policy information about clinical studies

All manuscripts should comply with the ICMJE guidelines for publication of clinical research and a completed CONSORT checklist must be included with all submissions.

Clinical trial registration	IRCT20170608034390N14
Study protocol	https://irct.behdasht.gov.ir/trial/77072
Data collection	Prospective clinical trial: We conducted a randomized, double-blind, placebo-controlled crossover trial involving 40 healthy adult volunteers. The study was approved by the Shaheed Beheshti Medical University Ethics Committee (IR.SBMU.RETECH.REC.1402.304), conducted in accordance with the Declaration of Helsinki and applicable regulations governing research involving human participants, and prospectively registered in the Iranian Registry of Clinical Trials (IRCT20170608034390N14; https://www.irct.ir/trial/77072). Participants were recruited and data were collected at Imam Hossein Hospital, Tehran, Iran, between 21 June and 21 August 2024. The trial is reported in accordance with the CONSORT 2010 guidelines, and the study protocol and completed CONSORT checklist are provided in the Supplementary Information. Healthy male and female volunteers aged 20–30 years were enrolled. Biological sex was self-reported and recorded as a biological variable. The study was not designed or powered to detect sex-specific differences. Baseline age and sex were balanced between treatment-sequence groups (Supplementary Table 1). All participants provided written informed consent and received financial compensation for participation. Participants were randomized 1:1 to receive placebo followed by loratadine or loratadine followed by placebo using block randomization (10 blocks of four participants), with the allocation sequence generated using the Sealed Envelope online randomization service. Participants were enrolled by the study investigators and assigned to the randomized treatment sequence according to the generated allocation codes. Drug and placebo were packaged in identical bottles and labelled using the randomization codes by an independent clinical laboratory expert who was not part of the research team. Participants, investigators and outcome assessors remained blinded throughout the study, and treatment allocation remained concealed from the data analyst until completion of the analysis. Participants received oral loratadine (10 mg once daily) or matching placebo for 21 days during each treatment period, with no washout period. The primary endpoint was the change in Treg frequency following loratadine compared with placebo. The prespecified secondary endpoint was the number of $CD8^+$ effector T cells; this outcome is not reported here because it was outside the scope of the present study. Peripheral blood was collected at the end of each treatment period. PBMCs were isolated and analysed by flow cytometry following staining with CD4-FITC and CD25-PE antibodies (BioLegend). Tregs were identified as $CD4^+CD25^+$ lymphocytes using fluorescence-minus-one controls for gating. Six participants withdrew before day 22. An additional four participants in Group A and five in Group B missed the day 42 blood draw, resulting in 29 loratadine-treated and 30 placebo-treated samples. Retrospective cohort study: Electronic medical records from adult patients with a primary malignant tumour diagnosed at Lausanne University Hospital (CHUV) between 2000 and 2020 who had provided written institutional consent for research were analysed. Patients with benign tumours or carcinoma in situ were excluded. Absolute blood basophil counts were available for 11,164 patients. CCL24 quantification in bronchial aspirates: Bronchial aspirates were obtained from individuals undergoing diagnostic bronchoscopy at CHUV and collected and biobanked under registry CHUV_2022_023_RM, with approval from the Cantonal Ethics Committee of Vaud (VD2022-01536). Individuals with active lung infection, asthma or severe allergies were excluded. Human CCL24 concentrations were quantified using a sandwich ELISA kit (R&D Systems, DCC240B) according to the manufacturer's instructions. Human buffy coats: Buffy coats from healthy donors were obtained from the Lausanne Blood Transfusion Center under protocol P_297.
Outcomes	Based on pre-clinical studies in our mouse models, we predicted that daily use of loratadine can enhance Treg numbers. We therefore defined the percentage of Tregs in the peripheral blood of healthy individuals as the primary outcome of the study. Blood sampling, measurement and data acquisition is outlined in detail under data collection.

Flow Cytometry

Plots

Confirm that:

☒ The axis labels state the marker and fluorochrome used (e.g. CD4-FITC).

☒ The axis scales are clearly visible. Include numbers along axes only for bottom left plot of group (a 'group' is an analysis of identical markers).

☒ All plots are contour plots with outliers or pseudocolor plots.

☒ A numerical value for number of cells or percentage (with statistics) is provided.

Methodology

Sample preparation	Before euthanasia, deeply anaesthetized mice were perfused with PBS to remove intravascular blood cells. Lungs were harvested and dissociated using the Mouse Lung Dissociation Kit and gentleMACS Tissue Dissociator (Miltenyi Biotec). Tumours were minced and digested in IMDM containing collagenase IV (0.2 mg/ml), dispase (2 mg/ml) and DNase I (0.002 mg/ml) for 20 min at 37°C. Spleens were mechanically dissociated and filtered through 70-µm cell strainers. Blood was collected by tail-vein bleeding or cardiac puncture into EDTA-coated tubes. Red blood cells were lysed using RBC lysis buffer (Sigma), and the resulting single-cell suspensions were washed and transferred to 96-well U-bottom plates for antibody staining. Cell suspensions were incubated with anti-mouse CD16/CD32 Fc-receptor-blocking antibody (4 µg/ml) for 15 min at 4°C, followed by extracellular staining with the relevant fluorophore-conjugated antibodies for 30 min at 4°C. FOXP3 and GZMB intracellular staining was performed using the eBioscience FOXP3/Transcription Factor Staining Buffer Set, whereas IL-4 and IL-13 staining was performed using the Intracellular Fixation & Permeabilization Buffer Set (Thermo Fisher Scientific). For cytokine detection, cells were stimulated for 4 h with Cell Activation Cocktail and brefeldin A (10 µg/ml; BioLegend, 423303). Samples were acquired using BD LSRFortessa, BD LSR II SORP, Beckman Coulter CytoFLEX S and CytoFLEX LX, or Invitrogen Attune NxT flow cytometers. Compensation was performed using single-stained controls, and gates were defined using fluorescence-minus-one controls. Antibodies and gating definitions are provided in Supplementary Tables 2 and 3, with the corresponding gating strategies shown in Supplementary Figs. 1–9.
Instrument	BD LSRFortessa™, BD® LSR II SORP, Beckman Coulter CytoFLEX S and CytoFLEX LX, and Invitrogen Attune™ NxT flow cytometers were used for acquisition of flow cytometry data.
Software	For flow cytomentry analysis, we employed FlowJo, LLC V10.1.
Cell population abundance	Cell sorting was performed using a BD FACSAria™ Fusion flow cytometer to isolate cell populations for functional assays, adoptive transfer and downstream molecular analyses.
Gating strategy	Gating strategies are shown in supplementary figures 1 to 9 . Following gating on live cells, different immune cell populations were identified as follows: Blood • CD8+ T cells: CD45+ CD3+ CD11b– CD8+ • CD4+ T cells: CD45+ CD3+ CD11b– CD4+ • Tregs: CD45+ CD3+ CD11b– CD4+ FOXP3+ • Granzyme B+ T cells: CD45+ CD3+ CD11b– CD8+ GZMB+ • Basophil: CD45+ CD117– FCεR1+ CD49+ / CD45+ CD200R3+ FCεR1+CD49+ Tumor • FOXP3+ CD25+ double positive Tregs: CD45+ CD3+ CD11b– CD4+ FOXP3+ CD25+ • Granzyme B+ T cells: CD45+ CD3+ CD11b– CD8+ GZMB+ • Basophils: CD45+ CD117– FCεR1+ CD49+ (IL4+ or IL13+) Spleen • Tregs: CD45+ CD3+ CD11b– CD4+ FOXP3+ or CD4+ eGFP+ (Foxp3DTR mice) • FOXP3+ CD25+ double positive Tregs: CD45+ CD3+ CD11b– CD4+ FOXP3+ CD25+ • Granzyme B+ T cells: : CD45+ CD3+ CD11b– CD8+ GZMB+ • CD8+ T cells: CD45+ CD3+ CD11b– CD8+ • CD4+ T cells: CD45+ CD3+ CD11b– CD4+ • Basophils: CD45+ CD117– FCεR1+ CD49+ Lung parenchyma • Tregs: CD45+ CD3+ CD11b– CD4+ FOXP3+ • T cells: CD45+ CD3+ • CD8+ T cells: CD45+ CD3+ CD11b– CD8+ • CD4+ T cells: CD45+ CD3+ CD11b– CD4+ • Metastatic cancer cells: CD45– mCh+ (mammary tumor) or CD45– eGFP+ (lung tumor) • Basophils: CD45+ CKIT– FCεR1+CD49+ / CD45+ CD200R3+ FCεR1+CD49+

☒ Tick this box to confirm that a figure exemplifying the gating strategy is provided in the Supplementary Information.